

Plasticity in Cu thin films: an experimental investigation of the effect of microstructure

A thesis presented

by

Yong Xiang

to

The Division of Engineering and Applied Sciences

in partial fulfillment of the requirements

for the degree of

Doctor of Philosophy

in the subject of

Engineering Sciences

Harvard University

Cambridge, Massachusetts

October, 2005

© 2005 - Yong Xiang

All rights reserved.

Thesis advisor

Joost J. Vlassak

Author

Yong Xiang

**Plasticity in Cu thin films:
an experimental investigation of the effect of microstructure**

Abstract

The mechanical behavior of freestanding Cu thin films is investigated using the plane-strain bulge test. Finite element analysis of the bulge test technique confirms that the measurement is highly accurate and reliable. A versatile specimen fabrication process using Si micromachining is developed and an automated bulge test apparatus with high displacement and pressure measurement resolutions is constructed. The elastic-plastic behavior of Cu films is studied with emphasis on the effects of microstructure, film thickness, and surface passivation on the plastic response of the films. For that purpose, Cu films with a range of thickness and microstructure and with different surface passivation conditions are prepared by electroplating or sputtering. The microstructure is carefully characterized and the stress-strain curves are measured. The mechanical properties are determined as a function of film thickness and microstructure for films both with and without surface passivation. The stiffness of the Cu films varies with film thickness because of changes in the crystallographic texture of the films and the elastic anisotropy of Cu. No modulus deficit is observed. The yield stress of unpassivated films varies mainly with the average grain size, while film thickness and texture have a

negligible effect. The yield stress follows the classical Hall-Petch relation with a coefficient close to that for bulk Cu. The results indicate that grain boundary strengthening is the main strengthening mechanism for unpassivated Cu films. Passivated films exhibit increased yield stress and work-hardening rate, as well as a distinct Bauschinger effect with the reverse plastic flow already occurring on unloading. Moreover, the yield stress increases with decreasing film thickness. Comparison of the experimental results with strain-gradient plasticity and discrete dislocation simulations suggests that the presence of any film-passivation interface restricts dislocation motion and results in the formation of a boundary layer with high dislocation density near the interface, which leads to a back stress field that superimposes on the applied stress field in the film. The directionality of the back stress leads to plastic flow asymmetry: it increases the flow stress on loading but assists reverse plastic flow on unloading. The boundary layer does not scale with the film thickness; hence the influence of the back stress increases with decreasing film thickness.

Table of Contents

Title Page	i
Abstract	iii
Table of Contents	v
List of Figures	ix
List of Tables	xv
Acknowledgements	xvi
Dedication	xviii
Chapter 1 Introduction	1
1.1 Background: Thin films and their applications	2
1.2 Mechanical behavior of thin films: Motivation	4
1.2.1 Technological driving force: Mechanical behavior and materials reliability	4
1.2.2 Scientific driving force: Size effects	7
1.2.3 Materials system	9

1.3	The goal and outline of the thesis	11
Chapter 2	Microstructure and mechanics of thin films: Background information	13
2.1	Thin film growth	14
2.1.1	Evaporation and sputtering	14
2.1.2	Electroplating	16
2.2	Thin-film microstructures	17
2.3	Mechanical characterization techniques	20
2.3.1	Techniques for films on substrate	20
2.3.2	Techniques for freestanding films	24
2.4	Advances in thin film mechanics	26
Chapter 3	The plane-strain bulge test technique for thin films	31
3.1	A brief review of the bulge test technique	32
3.2	Finite element analysis	35
3.3	Sample preparation	44
3.4	Experimental setup	47
3.5	Results and discussion	48
3.6	Summary	51
Chapter 4	The mechanical properties of freestanding electroplated Cu thin films	53
4.1	Objective and overview	53
4.2	Experimental	54
4.3	Results	55
4.3.1	Microstructural characterization	55
4.3.2	Mechanical properties	64
4.4	Discussion	67
4.4.1	Elastic modulus	67
4.4.2	Stress–strain curves and residual stresses	70
4.4.3	Yield stress	71

4.5	Summary	75
Chapter 5	Length-scale effect in freestanding Cu thin films	77
5.1	Objective and overview	78
5.2	Experiments	79
5.3	Experimental results	82
5.3.1	Microstructure	82
5.3.2	Stress–strain curves	87
5.3.3	Yield stress	91
5.4	Strain-gradient plasticity calculations	94
5.4.1	The strain-gradient plasticity	95
5.4.2	Problem formulation	96
5.4.3	Numerical results	100
5.5	Discrete dislocation dynamics simulations	103
5.5.1	Modeling	103
5.5.2	Numerical results	105
5.6	Comparison and discussion	108
5.7	Summary	111
Chapter 6	Bauschinger effect in Cu thin films	114
6.1	Introduction	115
6.1.1	What is Bauschinger effect?	115
6.1.2	Bauschinger effect in thin metal films	116
6.1.3	Objective and overview	117
6.2.	Compression test for thin metal films	118
6.2.1	The compression test technique	118
6.2.2	Application to thin sputter-deposited Al and Cu films	121
6.2.3	Discussion	126
6.3	The influence of free surfaces, interfaces, and grain boundaries on Bauschinger effect	128
6.3.1	Experimental results	129

6.3.2	Comparison and discussion	130
6.3.3	Length-scale effect versus Bauschinger effect	134
6.4	Summary	136
Chapter 7	Conclusions and outlook	138
7.1	Summary and concluding remarks	138
7.2	Suggestions for future work	143
Bibliography		146
Appendix A	Experimental documentation	158
A.1	Micromachining	158
A.1.1	Substrate preparation	159
A.1.2	Photolithography	161
A.1.3	Reactive ion etch	162
A.1.4	Anisotropic wet etch	164
A.2	Bulge test system	166
A.2.1	Displacement measurement	166
A.2.2	Data acquisition and experimental procedure	169
A.2.3	Data processing	172
Appendix B	Calculation of the equivalent uniaxial stress–strain curve	174
Appendix C	Calculation of the plane-strain modulus of a polycrystalline film	178
Appendix D	Influence of grain boundary grooving on experimental film stiffness	182
Appendix E	Taylor factor for polycrystalline thin films	184

List of Figures

FIGURE	PAGE
1.1 Cross sections of a 90 nm CMOS microprocessor. (From [1]).	3
1.2 SEM micrographs of MEMS micromirror arrays showing the film layer structure. (From [2]).	3
1.3 (a) Cross-sectional TEM micrograph shows Cu interconnects manufactured using dual damascene process. (b) Cracks A and B are formed in Cu vias due to stresses caused by temperature cycles. (From [13]).	7
1.4 Calculated gate and interconnect delay versus technology generation. (From [27]).	10
3.1 Schematic of the plane-strain bulge test for a long rectangular membrane: (a) Perspective view of the freestanding film before and after a uniform pressure (p) is applied; (b) Plan view of a typical sample showing a long rectangular membrane framed by a Si substrate.	36
3.2 The plane-strain stress–strain curves obtained from the finite element method for various aspect ratios [$b/a = 2, 4$ and 5] and for $n = 0$ (a), $n = 0.2$ (b) and $n = 0.5$ (c); (d) The plane-strain stress–strain curves	

	calculated using small and large deformation formulae for a membrane with $n = 0.2$ and $b/a = 4$	40
3.3	The pressure–deflection curves and corresponding plane-strain stress–strain curves obtained from the finite element method for an ideally plastic material [(a, b) $n = 0$] and a strain-hardening material [(c, d) $n = 0.5$] with various levels of residual stress ($\sigma_{res}/\sigma_y = 0, 0.6,$ and 1).	42
3.4	The von Mises stress–strain curves for the ideally plastic material [(a) $n = 0$, corresponding to Fig. 3.3(b)] and strain-hardening material [(b) $n = 0.5$, corresponding to Fig. 3.3(d)] with various levels of residual stress ($\sigma_{res}/\sigma_y = 0, 0.6,$ and 1).	43
3.5	Schematic illustration of the sample preparation process using the standard photolithography and Si micromachining technology.	45
3.6	Schematic illustration of the bulge test apparatus.	47
3.7	Experimental results for a $2.8 \mu\text{m}$ electroplated Cu film: (a) The pressure–deflection curve with two brief unloading cycles; (b) The plane-strain stress–strain curve; (c) Evolution of the transverse and longitudinal stress with applied strain; (d) The von Mises equivalent uniaxial stress–strain curve.	49
3.8	Parallel FEM analysis for the experimental data: (a) The pressure–deflection curve obtained with FEM is in good agreement with the experimental curve; (b) The corresponding plane-strain stress–strain curves are compared with the “input” plane-strain behavior.	51
4.1	Focused ion beam (FIB) micrographs showing the grain structure of as-deposited [(a), (b), and (c) for $h = 0.9, 1.8,$ and $3.0 \mu\text{m}$, respectively] and annealed [(d), (e), and (f) for $h = 0.9, 1.8,$ and $3.0 \mu\text{m}$, respectively] Cu films.	58
4.2	The orientation distribution function (ODF) of as-deposited [(a), (b), and (c) for $h = 0.9, 1.8,$ and $3.0 \mu\text{m}$, respectively] and annealed [(d), (e), and (f) for $h = 0.9, 1.8,$ and $3.0 \mu\text{m}$, respectively] Cu films as a function of the three Euler angles.	60
4.3	TEM micrographs showing the grain structure of a $1.8 \mu\text{m}$ untested Cu film before [(a) and (b)] and after [(c)] annealing, and a $3.0 \mu\text{m}$ annealed Cu film after the bulge test [(d)].	62

4.4	AFM results showing grain boundary morphology of annealed 1.8 μm [(a) and (b)] and 3.0 μm [(c) and (d)] Cu films. [(a) and (c)]: Plan-view in deflection mode; [(b) and (d)]: Cross-sectional profile showing the extrusion heights and groove depths.	63
4.5	The plane-strain stress–strain curves of freestanding electroplated Cu films.	65
4.6	The variation of stiffness with film thickness and heat treatment.	66
4.7	The plane-strain yield stress (a), the resolved shear stress (b) and the plane-strain Taylor factor (b) as a function of film thickness and heat treatment.	66
4.8	Periodic crack model for grain boundary grooves.	68
4.9	The normalized effective plane-strain modulus, M_c / M_0 , as a function of the normalized depth, c / h , and density, h / d , of the grain boundary grooves.	69
4.10	The plane-strain yield stress as a function of average grain size ignoring twin boundaries (a) and taking twin boundaries into account (b).	74
5.1	The FIB micrograph (a) and the orientation distribution function (b) for an electroplated 1.9 μm Cu film.	84
5.2	Cross-section TEM micrographs of electroplated Cu films after deformation showing: (a) Grain size on the order of the film thickness for a 1.0 μm film; (b) More than one grain across the film thickness for a 4.2 μm film; (c) A region of high dislocation density at the Cu-Ti interface in a 1.8 μm passivated film.	85
5.3	Typical plan-view TEM micrographs showing the grain structure for Cu films of 0.34 (a) and 0.89 (b) μm	86
5.4	Stress–strain curves of the first set of electroplated Cu films. (a) The effect of passivation for 1.0 μm films. (b) The effect of film thickness for 1.0 – 4.2 μm films with both surfaces passivated by 20 nm Ti. All curves are offset by the equi-biaxial residual strains in the films, as represented by the dashed line starting from the origin.	88
5.5	The stress–strain curves of 1.8 μm electroplated Cu films (2 nd set) with both surfaces passivated by 20 – 50 nm Ti. All curves are offset by the	

	equi-biaxial residual strains in the films, as represented by the dashed line starting from the origin.	89
5.6	Typical stress–strain curves for unpassivated (dotted curves) and passivated (solid curves) Cu films: (a) – (e) for 0.34 – 0.89 μm films, respectively. All curves are plotted at the same scale and are offset by the equi-biaxial residual strains in the films, as represented by the dashed line starting from the origin.	90
5.7	Yield stress as a function of reciprocal film thickness for both passivated (filled symbols) and unpassivated (open symbols) Cu films. The data for sputter-deposited and electroplated Cu films are separated by a vertical dash-dot line.	92
5.8	The yield stress of unpassivated films is correlated with the average grain size through a distinct Hall-Petch behavior. The data agree remarkably well with the results [open circles] for freestanding electroplated films investigated in Chapter 4.	92
5.9	Yield stress as a function of the passivation layer thickness for 1.8 μm electroplated films. The dashed line represents the contribution of the Ti layers if there is no plastic deformation in Ti.	94
5.10	Schematic illustration of the cross-section of a thin film under plane-strain tension. The bottom surface of the film is passivated by a rigid layer.	97
5.11	(a) Calculated stress–strain curves for films with one surface passivated [$N = 0.1$]. (b) Distribution of transverse plastic strain and (c) distribution of transverse stress across the film thickness at a given applied strain.	101
5.12	The strengthening factor, S , as defined in Eq. (2), versus the normalized film thickness. The dashed line is the best fit to experimental data with a length scale parameter $\ell = 360$ nm for a hardening index $N = 0.15$, while the solid line is the best fit with $\ell = 330$ nm for $N = 0.1$	102
5.13	The two-dimensional model of a freestanding film with both surfaces passivated and under tensile loading.	104
5.14	The distribution of stress and dislocation in 1 μm films with (a) both surfaces passivated, (b) bottom surface passivated, and (c) no passivation. The applied strain is $\varepsilon = 0.5\%$	106

5.15	Discrete dislocation simulations reproduce the experimental stress–strain curves for the first set of Cu films [Fig. 5.4]: (a) Effects of passivation on stress–strain curves of 1.0 μm film; (b) Effects of film thickness on stress–strain curves of films with both surfaces passivated.	107
5.16	Comparison between experimental and computational yield stress as a function of the reciprocal of film thickness for (a) films with one surface passivated and (b) unpassivated films.	108
5.17	A boundary layer with high plastic strain gradients is formed near the film–passivation interface. The thickness of this layer is independent of film thickness.	110
6.1	Schematic illustration of the typical stress–strain curve of a metallic material that exhibits the Bauschinger effect.	115
6.2	The principle of the compression test technique for thin metal films. The stress–strain curves of the metal and ceramic layers in the composite film are schematically shown.	119
6.3	TEM micrographs showing the grain structure of a 1 μm Al film (a) and a 0.6 μm Cu film (b).	122
6.4	Pressure–deflection curves of the Cu/Si ₃ N ₄ bilayer and the freestanding Si ₃ N ₄ film. For clarity, only every twentieth data point of the Si ₃ N ₄ unloading curve is displayed (■).	124
6.5	Stress–strain curves of passivated and freestanding films for a 0.6 μm Cu film (a) and a 1 μm Al film (b). The stress–strain curves are offset by the biaxial residual strains in the films, as represented by the dashed lines starting from the origins in the stress–strain curves.	125
6.6	Dislocations interact with grain boundaries as well as free surfaces and interfaces in thin films.	126
6.7	Bauschinger effect in sputter-deposited Cu films: the reverse plastic strain, ε_{rp} , as defined in the inset, versus the applied prestrain, ε_p . Both strains are normalized by the yield strain, $\varepsilon_y = \sigma_y (1 - \nu^2) / E$	129
6.8	Discrete dislocation simulations predict significant Bauschinger effect in films with one surface passivated: (a) $h = 1 \mu\text{m}$, $d = 1.5 \mu\text{m}$ and (b)	

	$h = 0.6 \mu\text{m}$, $d = 0.5 \mu\text{m}$. By contrast, little or no reverse plastic flow is observed in unpassivated films.	131
6.9	The reverse plastic strain as a function of the total prestrain for each unloading loop of the stress–strain curves obtained by numerical simulations [open symbols] and experimental measurements [filled symbols]. Both strains are normalized by the corresponding yield strains.	133
6.10	Calculated dislocation density at approximately yield stress versus the reciprocal of film thickness. Figures are taken from Ref.	133
A.1	Si wafer cleavage method: (a) Schematic illustration of the cross-section of the Si wafer and the glass pliers; (b) The glass pliers.	160
A.2	A typical photolithographic mask designed for patterning 2 by 2 long rectangular windows in the Si_3N_4 coating. The mask is in negative tone. The dimensions of the rectangles are $3.32 \times 10.92 \text{ mm}^2$	161
A.3	Schematic illustration of the wet etching system.	165
A.4	Schematic illustration of the wafer holder for wet etching.	165
A.5	The light sensitive resistor.	167
A.6	(a) A full bridge circuit to monitor the fringe intensity. (b) The power supply and signal processing module (SCC-SG04) for the full bridge.	167
A.7	Schematic illustration of the experiment control software interface.	170

List of Tables

TABLE		PAGE
4.1	Summary of results.	56
5.1	Summary of experimental results.	80
A.1	Photolithography steps and parameters.	163
A.2	Procedure for wet etching.	164
A.3	Procedure for the bulge test.	171

Acknowledgements

I would like to express my deep gratitude to all those who have generously helped me in the past five years.

First of all, I am most grateful to my advisor Professor Joost J. Vlassak for his guidance, advice, and encouragement these years. He is a great scientist as well as a great person, who is intelligent, encouraging, and supportive. It has always been a pleasure to have those inspiring discussions with him. I have learned more than knowledge from him. It is an honor and privilege to be one of his first Ph.D. students.

I would like to thank Professors John W. Hutchinson, Frans Spaepen, and James R. Rice for serving in my research committee and offering me many valuable advices on my graduate study and research. Professor Hutchinson helped me a lot on the strain-gradient plasticity calculations. I would also like to thank Professor Zhigang Suo. I benefited much from working with him on the Cu/polymer project.

I am very grateful to Professor Xi Chen at Columbia University, who is a brilliant scholar as well as a wonderful friend. He has always been so helpful to me, nearly in every aspect of my life, since the first day I arrived at Harvard.

I sincerely thank Dr. Ting Y. Tsui for his help with materials preparation. I also greatly appreciate the generous help from Drs. Maria T. Perez-Prado, Vidya Ramaswamy, Warren Moberly-Chan, David Bell, Young-Shin Jun, and Cheng-Yen Wen with microstructure characterization. Dr. Lucia Nicola, Professor Alan Needleman, and Professor Eric Van der Giessen provide the discrete dislocation simulations of the experiments in Chapter 5, which aided in the understanding of the experimental results.

I would also like to thank Xi Wang, Youbo Lin, Teng Li, Prita Pant, Zhen Zhang, Zhenyu Huang, Patrick McCluskey, Anita Bowles, and many other current and former members in the materials science and the solid mechanics groups at Harvard.

Many thanks to Ren Feng, Yang Ling, Irene Mai, Simon Xi, Lu Hu, Xin Zhong, Shan Huang, and other wonderful friends. Their friendship has made my life full of pleasure. Special thanks go to Ms. Sandra Basch. She is such a noble and loving person who is always ready to help others. She has taught me a lot of things beyond school. Her friendship and generous help have meant so much to me and to my family all these years.

The last but not the least, I am deeply indebted to my family. Without their love and support, I can never have reached this far.

Dedicated to my family.

Chapter 1

Introduction

In this chapter, the background and motivation for the current study are given. The wide use of thin film technology in many important engineering applications has initiated extensive research on thin-film materials. Our motivation also comes from an academic interest in the unusual behavior observed in materials at very small scales. Thin films provide a unique opportunity to extend our understanding of material behavior at multiple length-scales. There have been numerous attempts to improve this understanding. The work presented in this thesis represents one of these attempts in one very particular field – plasticity in materials at the sub-micron and micron scales. The basic goal and the organization of this work are given at the end of this chapter.

1.1 Background: Thin films and their applications

The digital revolution brought about by the development of integrated circuits over the last half century is one of the most astonishing achievements in human history. Computers, cellular phones, and many other information technologies have now become indispensable parts of modern societies. These technologies – modern computers, the Internet, telecommunications, as well as modern financial, business, manufacturing, and transportation systems – all depend on the existence of integrated circuits. For all their importance, integrated circuits could have never been achieved without the creative and efficient exploitation of thin film materials. Most materials used in advanced microelectronic devices are in thin film form. For example, a single state-of-the-art microprocessor contains hundreds of millions of thin-film transistors that are interconnected by numerous thin metal wires. Figure 1.1 shows the cross-sections of a typical 90 nm CMOS processor that contains 1 level of W contacts and local interconnects as well as 10 levels of Cu interconnects [1]. The continuing miniaturization and increasing complexity of metal interconnects have become the cost, yield, and performance limiter for advanced integrated circuits.

Thin films are also essential components of microelectromechanical systems (MEMS) [2]. In these microscopic machines, mechanical and electronic components are microfabricated from thin films and integrated together using techniques developed by the microelectronics industry. A host of devices with unique capabilities at very small scales such as sensors, actuators, power producing devices, chemical reactors, and biomedical devices have been developed. These devices have found a variety of

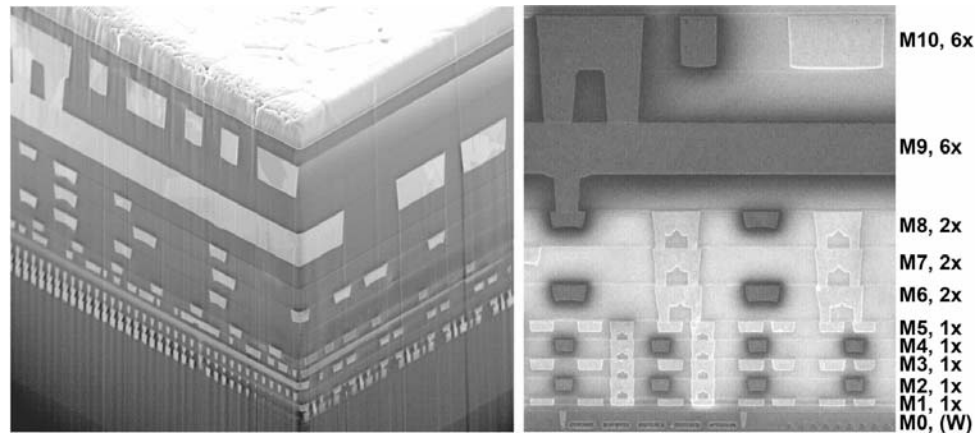


Figure 1.1: Cross sections of a 90 nm CMOS microprocessor. (From [1])

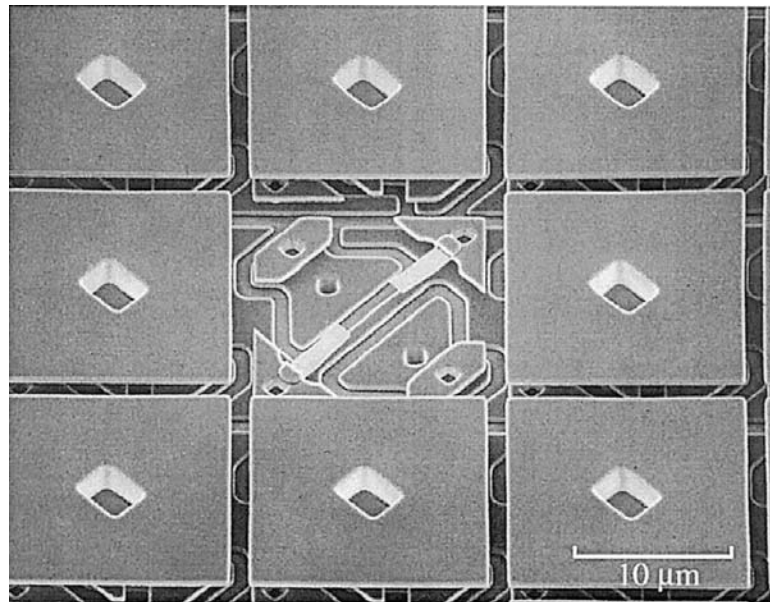


Figure 1.2: SEM micrographs of MEMS micromirror arrays showing the film layer structure (From [2])

applications across a wide range of industries. For example, Figure 1.2 illustrates the complex layer structure of a MEMS micromirror array widely used in portable projectors [2]. The essential structural and functional components are in thin-film form. Other examples of commercially successful MEMS devices [2] include inkjet printer heads, accelerometers, gyroscopes, pressure sensors, and optical switches. The feature size of MEMS devices continues decreasing and merges at nanometer scales into nanoelectromechanical systems (NEMS) and nanotechnology.

Besides the microelectronics and MEMS industries, thin films and coatings are also extensively used as wear resistant coatings on cutting tools, protective coatings in data storage devices, and thermal barrier coatings on turbine blades.

1.2 Mechanical behavior of thin films: Motivation

1.2.1 Technological driving force: Mechanical behavior and materials reliability

In certain applications, thin films are used as components that carry mechanical loads. In these applications, the mechanical performance of the thin-film material is the primary consideration in materials selection. Examples include the structural and moving parts in MEMS devices, such as the hinges in micromirror arrays and optical switches, wear resistance coatings on cutting tools, and protective coatings for magnetic disks.

In many other applications, thin films are selected primarily because of their unique electronic, magnetic, optical, or thermal properties. The mechanical characteristics of the materials of choice in such applications are, however, not unimportant because thin films are often subjected to large mechanical stresses during both the manufacturing process and normal operation of the end-use devices.

Generally, mechanical stresses in thin films can be divided into either the so-called intrinsic or growth stresses that develop during the deposition process, or the extrinsic stresses that are induced by external physical effects [3-6]. Thin-film materials are fabricated using very different processing methods than those for bulk materials, such as epitaxial growth and various vapor deposition techniques. These processing methods often result in development of mechanical stresses in the films. There have been many mechanisms proposed for the development of growth stresses, which depend sensitively on the materials systems, deposition technique, and process parameters [7-12]. The extrinsic stresses are induced by various physical effects after the film is grown. One of the most commonly encountered examples is the thermal mismatch stress due to the thermal expansion mismatch between a film and its substrate [3]. The manufacturing process and normal operation of most thin-film based devices often involve large temperature cycles. Therefore, thermal mismatch stresses are inevitable and they can be very high if the thermal mismatch is large and the elastic modulus of the film is large, such as is the case for Cu films used in integrated circuits.

Large mechanical stresses are unfavorable in most applications. For example, large mechanical stresses sometimes causes the materials to deviate from their ideal

functions due to coupling between the mechanical and functional properties. This often leads to device malfunction and/or failure. For example, high levels of residual stress in shape memory alloy thin films may prevent a phase transformation from occurring and may lead to loss of the shape memory effect. For piezoelectric thin films, excessive deformations due to large stresses may also cause the material to behave differently from its ideal function.

Even though the presence of large mechanical stresses may sometimes not significantly affect the functional properties of thin films, they may still cause a material to fail by promoting the formation of voids or cracks in the films or by delaminating the films from attached layers. For example, the multilayered Cu interconnects in the CMOS processor in Fig. 1.1 are bonded tightly to barrier coatings and interlayer dielectrics. Figure 1.3(a) shows the details of such a configuration [13]. High levels of thermal mismatch stresses in both the Cu interconnect and surrounding layers can be induced because the CTEs of the Cu interconnect and surrounding materials are very different. Temperature cycles produce cyclic stresses in these materials and fatigue becomes a potential failure mechanism. Microcracks may develop in the Cu interconnects causing increased resistance or electrical opens in the circuits, as shown in Fig. 1.3(b). The surrounding layers may also crack or delaminate from the Cu interconnects.

Therefore, understanding and controlling the mechanical properties of thin films is of paramount significance in order to improve the reliability and lifetime of devices based on thin films. Investigations of the mechanical behavior of thin films were initiated as a result of this technological driving force and continue to be motivated as the

microelectronics adopts new material systems and as dimensions of devices continue to shrink.

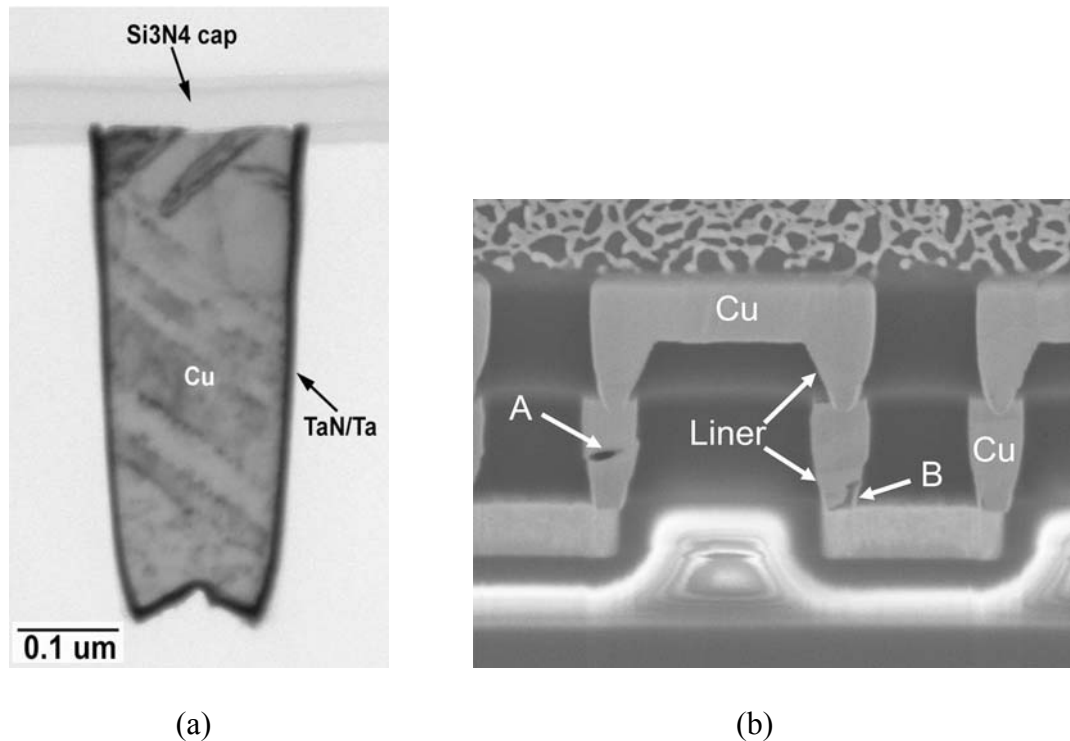


Figure 1.3: (a) Cross-sectional TEM micrograph shows Cu interconnects manufactured using dual damascene process. (b) Cracks A and B are formed in Cu vias due to stresses caused by temperature cycles. (From [13])

1.2.2 Scientific driving force: Size effects

In addition to the tremendous technological driving force, there is also a strong scientific motivation to study thin-film mechanical behavior. It has long been recognized that the mechanical properties of thin films can be very different from those of their bulk

counterparts [3, 6]. This phenomenon is generally referred to as a size effect and reflects the scaling laws of physical properties [2, 14]. Some properties can be simply explained through extrapolation of bulk behavior [2], but other properties depend sensitively on mechanisms that remain illusive [14]. The strength of thin films is a prime example: A substantial amount of experimental evidence has shown that thin metal films can support much higher stresses than the same material in bulk form. This strengthening has generally been attributed to dimensional and microstructural constraints on dislocation activity in thin films [14].

Dimensional constraints are imposed by the interfaces and the small dimensions typically encountered in thin films, while microstructural constraints arise from the very fine grains often found in thin films. In bulk materials, microstructural constraints dominate the plastic behavior of the material. However, when material dimensions are comparable to microstructural length scales – as is typically the case for thin films – free surfaces and interfaces play an important role as well. For example, dislocations can exit the material through free surfaces, while strong interfaces can prevent them from doing so. Consequently, strong interfaces lead to a higher cumulative dislocation density in the film and result in a higher flow stress and a greater strain-hardening rate. This behavior cannot be captured by classical plasticity theories [15] and motivates a strong interest in developing new models to describe it.

In addition to dimensional constraints, the microstructure of thin films also affects their mechanical properties. Since thin films are fabricated using different techniques than those for bulk materials, the microstructure of thin films is often very different from

that of bulk materials [16, 17]. A thorough understanding of the effect of the microstructure certainly expands our knowledge significantly.

In summary, understanding the deformation mechanisms for thin films is not only important to take full advantage of the materials and improve device reliability, but also important expand to our knowledge of the processing-structure-property relationship, one of the basic tasks in materials science.

1.2.3 Materials system

In the current study, Cu thin films were selected as a model materials system because of the technological significance of Cu as the new interconnect material in integrated circuits.

In the past, the mechanical properties of thin films of Al and its alloys were studied in order to improve the reliability and lifetime of devices with Al. With the continuing miniaturization of microelectronics devices and increasing current density in the interconnects, it was found that electromigration became a major failure mechanism for these conductor lines and that the improvements in reliability and performance of interconnects based on Al alloys would soon reach practical limits [23-26]. Moreover, with decreasing device size, the resistance-capacitance (RC) interconnect signal delay becomes increasingly dominant over the gate delay as illustrated in Fig. 1.4 [27]. The curves in Fig. 1.4 suggest that the delay can be minimized by lowering the electrical resistivity of the interconnects and the permittivity of the dielectric. Cu has higher electrical and thermal conductivity, higher melting temperature and consequently better

resistance to electromigration, all of which make it a much better interconnect material than Al [28]. As a result, Cu interconnects, together with low-permittivity (low-k) dielectric interlayers, recently replaced the traditional combination of Al interconnects and SiO₂ in state-of-the-art integrated circuits.

There are also, however, some potential reliability issues with Cu. For example, Young's modulus of Cu is 50% higher than that of Al. Thermal mismatch and temperature cycles induce higher stress levels in both Cu interconnects and the surrounding dielectric. The strength of Cu is also much higher than Al. On the one hand a high strength is favorable for the mechanical performance of the material, but on the other it leads to large residual stresses that may cause excessive deformation and/or

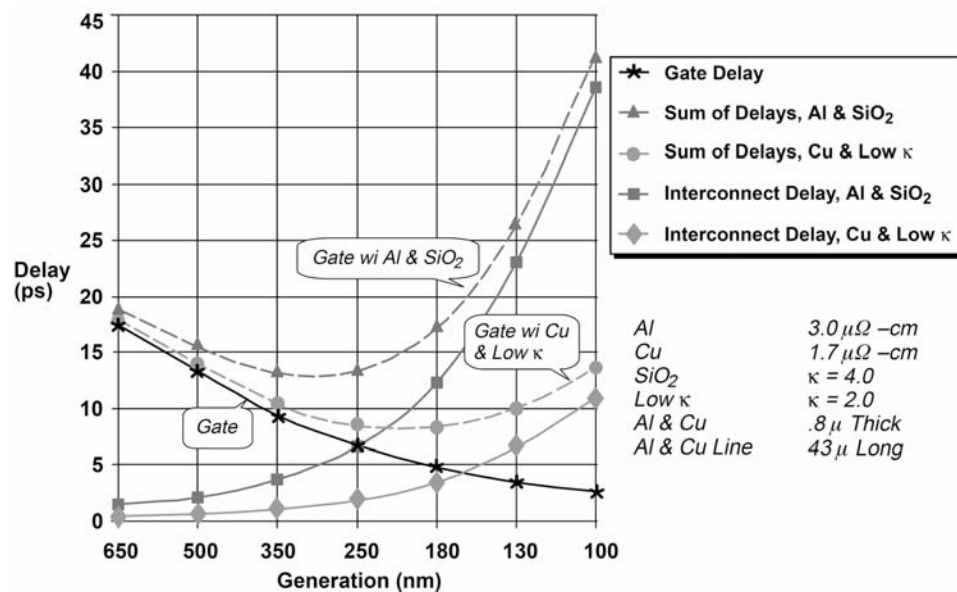


Figure 1.4: Gate and interconnect delay versus technology generation. (From [27])

promote cracking of the surrounding dielectrics. Moreover, a thin barrier layer on Cu surface is necessary to prevent diffusion. How such a surface passivation affects the mechanical behavior of Cu films also needs to be well understood. Therefore, in order to take full advantage of Cu as the new interconnect material and to further improve the reliability of devices based on Cu metallization, it is necessary to achieve the same level of understanding of its mechanical behavior as for Al films.

1.3 The goal and outline of the thesis

The goal of the current work is to extend our understanding of the mechanisms that control the mechanical properties of thin metal films, and Cu films in particular. The microstructure of the Cu films is carefully characterized. Special experimental techniques are developed to fabricate and test freestanding thin Cu films. The stress–strain curves are measured and mechanical properties such as Young’s modulus, yield stress, and work-hardening are investigated. The film properties are correlated with the microstructure of the films. Experimental results are then compared with existing models, such as strain-gradient plasticity theories and discrete dislocation dynamics simulations. The comparison yields quantitative agreement between experimental and theory. While thin Cu films were chosen as our model system, the approach is readily adapted to study the mechanical properties of other thin films.

The thesis is organized as follows. Chapter 2 briefly reviews the current status of research on the mechanical behavior of thin metal films.

Chapter 3 discusses the experimental technique used in this study, namely the plane-strain bulge test technique.

In Chapter 4, we investigate the mechanical properties of freestanding electroplated Cu thin films with various thickness and microstructure. The influence of film thickness, grain size, and crystallographic texture on the mechanical properties is evaluated quantitatively.

Chapter 5 focuses on the effects of surface passivation and film thickness on the yield stress and work-hardening rate of both electroplated and sputter-deposited Cu thin films. The experimental results are compared with strain-gradient plasticity calculations and discrete dislocation simulations.

In Chapter 6, we present a new experimental technique that allows us to test thin metal films in tension and compression and use this technique to investigate the Bauschinger effect in Cu films. The experiments are compared with the results of discrete dislocation simulations.

Finally, concluding remarks of the current study and suggestions for future work are given in Chapter 7.

Chapter 2

Microstructure and mechanics of thin films: Background information

In order to achieve a good understanding of the deformation mechanisms in thin films and to develop adequate models to describe them, we first need extensive and accurate measurements of their mechanical response. Specialized mechanical test techniques are required for that purpose. We also need a careful characterization of the microstructure of the films. Since the microstructure of a material is sensitively dependent on the fabrication process, knowledge of typical film deposition techniques is of course helpful. In this chapter, we briefly review several deposition techniques, thin-film microstructures, some specialized mechanical test techniques, as well as advances in thin films mechanics in the literature.

2.1 Thin film growth

Unlike bulk materials that are manufactured by methods such as casting, drawing, rolling, molding, etc., thin films are usually produced by fundamentally different techniques. Some common methods for thin film growth include various vapor deposition processes, spincoating, and electroplating [29]. Vapor deposition, which refers to a group of techniques that appear in many different forms, is the most widely used. Vapor deposition involves creation of a vapor phase in which the substrate is immersed and the film is grown on its surface. Vapor deposition methods are typically classified into two main types: (i) physical vapor deposition (PVD), where the vapor is formed through physical processes and no chemical reactions are involved in the deposition; (ii) chemical vapor deposition (CVD), where the material deposited is the product of a chemical reaction in the vapor or at the surface of the film. A detailed review of various techniques is beyond the scope of this thesis and interested readers are referred to [29]. In this section, we briefly introduce several of the most commonly used techniques for thin metal films, including evaporation, sputtering, and electroplating.

2.1.1 Evaporation and sputtering

Evaporation and sputtering are the two most commonly used PVD methods. Evaporation is a process in which the vapor is created by evaporating the source material using thermal energy in one form or another. Evaporated atoms travel a distance in a vacuum chamber before they condense on a substrate surface immersed in the vapor.

Depending on the thermal energy source used, evaporation can be divided into several types, including thermal evaporation, electron-beam evaporation, and molecular beam epitaxy. Evaporation is a thermal process where atoms of the material to be deposited arrive at the growth surface with low kinetic energy. The microstructure of the as-deposited film is affected by various parameters such as base pressure, substrate condition, power, deposition rate, etc. Evaporated films are often highly textured.

Sputtering is a process in which the vapor of the source materials is formed through ionic impingement of a target. In sputter deposition, an evacuated chamber is filled with a sputtering gas, typically Ar. The gas is ionized by imposing a direct-current (DC) or radio-frequency (RF) voltage, which forms a plasma in the chamber. An imposed electrical field accelerates the Ar^+ ions toward the target at high speed. The target atoms are dislodged when the energetic ions bombard the target surface. These atoms then travel through the gas phase and condense onto the substrate, leading to film growth. Sputtering is a versatile technique that can be applied to many crystalline and amorphous materials. It offers better control in maintaining stoichiometry and more uniform film thickness. Alloy thin films with highly precise compositions can be fabricated through cosputtering. There are also some disadvantages. For example, because the target atoms usually have a high kinetic energy when they arrive at the growth surface, the probability of defect nucleation and damage in sputtered films is generally higher than in evaporated films. The condensation of high energy atoms also causes the substrate temperature to increase. Moreover, the sputtering gas may cause contamination by introducing impurity atoms in the films. Metal films sputtered at room temperature are typically polycrystal-

line, consisting of very fine grains. The microstructure is of course affected by many parameters such as substrate temperature, deposition rate, power, and working gas pressure.

2.1.2 Electroplating

Electroplating, which is sometimes also called electrodeposition, is a process in which a metal is coated on a conductive surface through electrochemical reactions that are facilitated by an applied electrical potential. In this process, the surface to be coated is immersed into a solution of one or more metal salts. The surface needs to be conductive and forms the cathode of the electrical circuit. With an electrical current passing through the solution, the positive ions of the source metal are attracted to the cathode surface, where they are reduced, resulting in a coating of the source metal on that surface. Electroplating is a simple and economical course to deposit uniform coatings. It has been used in many applications across a wide range of industries for more than a century. For example, copper conductor lines in printed circuit boards, chromium coatings on steel parts in automobiles, zinc coatings on galvanized steel, and decorative gold and silver coatings on jewelry and various consumer products are all realized by means of electroplating.

Electrodeposition is now introduced for growing Cu coatings in advanced integrated circuits. Cu metallization can be realized by many methods, among which the electrodeposition [28] has the advantages of simplicity, safety, low cost, low deposition temperature, low resistivity, and high gap filling capacity in a dual-damascene process.

Since a high-conductivity surface is required for the electrodeposition, a seed Cu layer is usually sputter deposited immediately prior to the plating process. A majority of the Cu films investigated in the current work were electroplated using a commercial process currently employed in the semiconductor industry [30].

There are also some limitations for electrodeposition. For example, it generally cannot be applied to deposit alloys and nonmetallic materials. Due to the exposure of the film growth surface to the solution, impurities may be introduced.

2.2 Thin-film microstructures

The physical properties of thin films are determined by their microstructure. Therefore, no investigation of the mechanical properties of thin films is complete without a thorough characterization of their microstructure. Microstructure is a collective description of the arrangement of crystallites and crystal defects in a material [14]. Some of the most important characteristics include the shape, size, and orientation of the crystallites and their distributions, the density and distribution of crystal defects such as dislocations, defaults, and impurities, as well as the surface and interface morphologies [17]. These microstructural characteristics can be affected by many factors, including materials class, deposition technique and deposition conditions, heat treatment, and deformation history. There have been excellent reviews of the microstructure evolution in thin films, such as Refs. [16, 17]. In this section we summarize some key features related to thin metal films.

As already mentioned, films deposited by different techniques typically have very different microstructure. For example, metal films sputtered at room temperature typically consist of very fine grains, while evaporated films are often highly textured with larger grain sizes than sputtered films [29]. The microstructure formed in the deposition process is also materials dependent. For example, the mobility of the atoms of the target materials significantly affects the microstructure formation in both the deposition and post-deposition processes. The microstructure evolution during the growth process typically involves nucleation of crystallite islands from the condensed materials atoms at many sites on the substrate surface, growth of individual crystallites until they impinge with other crystallites, coalescence of the impinged crystallites, and coarsening of grains during thickening of the film [17]. For bulk materials, grain growth occurs at the expense of small grains through motion of grain boundaries, which is driven by the reduction in the total grain boundary energy. The grains are usually equi-axed. In thin films, free surfaces and interfaces also play an important role. Moreover, mismatch strains often develop between the film and the substrate and crystallographic orientations with higher in-plane elastic moduli lead to higher strain energy in the film. Therefore, grain growth and crystallographic texture development in thin films are driven by the reduction of the total energy, including the grain boundary energy, the surface and interface energy, and the strain energy. This is a thermally activated kinetic process. For films grown at room temperature, grain growth and texture development are often slow due to lack of thermal activation, resulting in a metastable structure with very fine grains.

The microstructure of thin films can be further modified through a post-deposition

process, such as annealing. During annealing, grains grow and crystallographic textures develop in order to minimize the total energy. The rate is determined by the annealing temperature. When a grain grows to a size on the order of the film's thickness, the grain boundaries intersect the film surface and form grooves at the surface. These grooves suppress further growth of the grain. As a result, a columnar grain structure with grain boundaries traversing the film thickness is formed. The grain size in the plane of the film is thus on the order of the film thickness. Annealing sometimes leads to grain boundary damage and surface morphology changes in thin films, such as grain boundary grooving, hillocking, and extrusion. These phenomena are caused by diffusional processes and arise as a result of thermal mismatch stresses during the heating and cooling of the film/substrate system.

Given the technological importance of the electrodeposition technique, it is worthwhile to have a look at the microstructure of electroplated thin films, which can be very different from those deposited by other methods. In electroplating, the microstructure of the film can be changed dramatically through the addition of certain chemicals to the plating bath. These chemicals are known as brighteners. The structure of Cu films deposited using the commercial resources currently in use consists of very fine grains and is very unstable. After deposition, the films spontaneously recrystallize at room temperature over a period of a few hours to several days [30-34]. After the recrystallization process, the as-deposited films develop a texture that is dependent on film thickness [30]. The films usually have a bimodal grain size distribution with a small number of giant grains due to abnormal grain growth [30]. The films often have a high

incidence of growth twins [30, 35]. Twin boundaries are coherent boundaries that have much smaller electrical resistivity than regular grain boundaries, which is a favorable feature for Cu used as conductor lines [35].

2.3 Mechanical characterization techniques

The first step toward a good understanding of the mechanical behavior of thin films is to obtain accurate values of various mechanical properties. The traditional mechanical testing methods used for bulk materials cannot be applied directly to the study of thin films because of the small dimensions of these materials. Several specialized techniques have been developed to characterize the mechanical behavior of thin films during the past decades. These techniques can generally be divided into two main categories: 1) Direct testing of thin films deposited on substrates, which involves minimum sample preparation. The film properties are, however, implicitly embedded in the experiment data, and significant post-processing effort is usually required in order to extract the intrinsic film properties. 2) Mechanical characterization of freestanding films, which requires careful specimen processing and handling. These techniques can yield explicit and accurate elastic-plastic properties of the films. In this section, we briefly review several of the most widely used techniques in both categories.

2.3.1 Techniques for films on substrate

Among the techniques for testing films on substrate, the substrate curvature [3]

and nanoindentation [36, 37] techniques are the most widely used and commercialized.

In the substrate curvature measurement, strains are imposed by varying the temperature of the film/substrate system if the coefficients of thermal expansion (CTE) of the film and the substrate are different. The stress in the film causes the film/substrate system to bend, the curvature of which can be measured using optical methods. Since the curvature of the substrate may not be zero, it is necessary to measure the substrate curvature prior to film deposition. The change of the substrate curvature, $\Delta\kappa$, can be related to the film stress, σ_f , through the Stoney equation [3, 38]:

$$\Delta\kappa = \frac{6\sigma_f h_f}{Y_s h_s^2} \quad (2.1)$$

where $Y_s = E_s / (1 - \nu_s)$ is the biaxial modulus of the substrate, h_f and h_s the film and substrate thicknesses, respectively. Given Y_s , h_f , and h_s , the film stress can be readily determined as a function of temperature by measuring the curvature of the film/substrate system as a function of temperature. It should be noted that the imposed strain is equibiaxial if both the film and the substrate are thermally isotropic. The technique is often used to study the thermal mechanical behavior of metal films on ceramic substrates. Proper interpretation of the experimental results is not easy because the mechanical response is complicated by the temperature change. Moreover, the strain level that can be imposed is limited by the difference of CTEs between the film and the substrate and the maximum temperature change. The microstructure of the films may also change during the thermal cycles.

Nanoindentation [36, 37] is a technique that can quickly probe the mechanical properties of various thin films deposited on substrates. In nanoindentation, a rigid indenter is driven into the film while the indentation load, P , and displacement, δ , are continuously recorded. If friction and the finite compliance of the measuring system and the indenter tip are neglected, the hardness, H , and indentation modulus, M , can be extracted using the following equations

$$H = P/A, \quad (1)$$

and
$$S = \gamma \frac{2}{\sqrt{\pi}} M \sqrt{A}. \quad (2)$$

Here, the hardness H is defined as the ratio between indentation load P and projected contact area A . The contact stiffness $S = dP/d\delta$ is obtained from the slope of the initial portion of the elastic unloading curve; γ is a correction factor for a specific indenter tip shape, e.g., $\gamma \approx 1.08$ for a three-sided pyramidal indenter tip with the same area-to-depth ratio as the Vickers indenter (i.e., the so-called Berkovich tip) [39, 40]. The hardness, H , is proportional to the material yield stress, σ_y . The ratio H/σ_y depends on indenter shape and material properties: it increases with E/σ_y and approaches a constant value (≈ 3) when $\bar{E} \tan \alpha / \sigma_y > 30$. [40, 41] If the material work hardens, the yield stress is taken at a representative strain [42], which is approximately 7% for a Berkovich indenter. For isotropic materials, the indentation modulus equals the plane-strain modulus, $M = E/(1-\nu^2)$, where E and ν are Young's modulus and Poisson's ratio of the isotropic

material, respectively. For anisotropic materials, M is given by a complicated function of the elastic constants [43].

Nanoindentation on thin films has uncertainties due to well-known experimental limitations that make it difficult to interpret the experimental data accurately. Most notable among these are the effects due to presence of the substrate, densification of the film as a result of large hydrostatic stresses, issues with tip calibration, surface roughness, and size effects as a result of the non-homogenous strain field. Considerable effort has been devoted to understanding these issues and to relating nanoindentation results to intrinsic material properties. For example, the substrate effect has been studied by Tsui et al. [44, 45], Saha and Nix [46], Chen and Vlassak [47], King [48], Bhattacharya and Nix [49], and Bolshakov and Pharr [50]. The effect of densification has been discussed by Fleck et al. [51] and Chen et al. [52]. The information that can be acquired from the nanoindentation is also limited. For example, nanoindentation is not suitable for measuring the work-hardening behavior or the residual stress in the film [44, 47].

In addition to the substrate curvature technique and nanoindentation, a number of dynamic techniques are available for determining the elastic properties of thin films on substrates. These techniques include surface acoustic wave spectroscopy (SAWS) [53] and surface Brillouin scattering (SBS) [54]. These techniques typically require knowledge of the density of the film and only provide information on the elastic behavior of the films.

2.3.2 Techniques for freestanding films

Among techniques developed to measure the mechanical behavior of freestanding thin films, the microtensile test [55-58] and the bulge test [59] techniques are widely employed. These techniques require some sample preparation, but they can be readily applied to measure intrinsic film properties without any substrate effects, and to obtain thin film constitutive behavior with relatively large applied strains.

The microtensile test is the analog of its bulk counterpart. Due to difficulties associated with sample handling at the micron or submicron scale, microtensile testing often suffers from alignment and gripping problem, which often leads to inaccuracy in the strain measurement. Spaepen and colleagues [56] have developed a diffraction-based technique for measuring the local strains of a freestanding film by patterning a square array of photoresist islands on the film surface. There are still some uncertainties in the strain measurement due to transverse wrinkling of the freestanding film. Since the film needs to be removed from the substrate before mounting it on the testing stage, residual stresses in the film cannot be measured. The sample handling also limits the thickness of the film that can be tested. Alternatively, a thinner film can be tested by depositing the film on a compliant polymeric substrate and by stretching the film/substrate composite structure [60]. The stress in the film can be obtained by subtracting the force-displacement curve of the substrate from that of the film/substrate composite structure. The local stresses in individual grains in the film can also be measured by means of x-ray diffraction [61]. Recently, progress has been made by using Si micromachining techniques to fabricate tensile specimens [55, 57]. For example, Saif and colleagues [55]

developed a MEMS-based technique in which the tensile specimen is integrated with the testing frame. Load and displacement are both measured by analyzing the SEM images of the testing frame. The testing frame features small size and can be fit into a TEM holder to perform in-situ microstructure characterization during the tensile test.

There is a variation of the microtensile test, the so-called membrane deflection experiment (MDE) that was developed by Espinosa and colleagues [58, 62, 63]. In this technique, a dogbone-shaped freestanding film stripe is microfabricated with an enlarged contact area at its center. A nanoindenter tip is used to apply line loading on this contact area and the load is continuously recorded. The gauge section of the freestanding film undergoes a pure stretch and the displacement is measured by means of a full-field interferometric method. This technique involves less specimen handling and offers accurate strain measurement. It is critical to avoid misalignment of the indenter tip in order to prevent errors caused by non-stretching deformations such as torsion. Moreover, the film stripe curls in the transverse direction due to Poisson's effect.

The bulge test is another powerful technique for measuring the mechanical behavior of freestanding thin films [59, 64, 65]. In this technique, freestanding thin films are obtained by opening a window in the substrate using micromachining techniques. The film is deflected by applying a uniform pressure to one side of the freestanding membrane. The mechanical properties of the film are determined from its pressure-deflection behavior. Compared with microtensile testing, the bulge test technique has the unique advantage of precise sample fabrication and minimal sample handling. There are virtually no issues related to specimen alignment and film wrinkling due to Poisson's

effect since the film is supported by Si substrate at all edges. Moreover, the residual stress in the film can be measured. With some care, freestanding films as thin as 50 nm can be prepared and tested. In the current work, the plane-strain bulge test is the primary mechanical characterization technique. A more detailed discussion on this technique will be given in the next chapter.

2.4 Advances in thin film mechanics

Exploration of the mechanical behavior of thin films can be traced back to as early as the 1950s [66]. This early work was initiated to study stresses and failures in integrated circuit structures. The field has developed rapidly since the late 1980s and the investigations were then extended to more general applications of thin films. There have been several reviews of the mechanical behavior of thin films by leading scholars in this field, such as Hoffman and Campbell [67], Nix [3], Alexopoulos and O'Sullivan [68], Vinci and Vlassak [6], Arzt [14], and Freund and Suresh [69]. Various theoretical models have been developed to describe the observed phenomena in thin films and other materials at small scales. In this section, these advances are reviewed with a special focus on the mechanical behavior of polycrystalline metallic thin films.

As mentioned before, thin films are generally much stronger than their bulk counterparts [3, 6] as a result of the film thickness effect as well as the effect of very fine grains. The film thickness effect cannot be captured by classical plasticity theories. Various theoretical and numerical models have thus been proposed to describe the new

features in thin film plasticity. These models can generally be divided into two main categories: (i) the macroscopic models, which are based on the continuum theory of plasticity, such as the strain-gradient plasticity theories by Aifantis [70, 71] or by Fleck and Hutchison [72-75]; (ii) the microscopic models, which are based on dislocation mechanics, such as the single dislocation model proposed by Nix [3], or the discrete dislocation dynamics simulations by Needleman and van der Giessen [76, 77]. Mechanisms for the size effect in small-scale plasticity typically fall into two main classes: (i) glide-controlled mechanisms, i.e., the dislocation glide is constrained due to the presence of plastic strain gradients or geometrically necessary dislocations (GND) [70, 71, 73-85], either due to non-uniform deformation [72, 86, 87] or due to prescribed boundary conditions, e.g., experiments in the current study; (ii) nucleation-controlled mechanisms, due to limited dislocation sources [87-89] at small material volumes.

The influence of microstructure on mechanical properties has been widely studied in bulk materials and a number of models are well established. For example, the Taylor relationship provides a relationship between flow stress and dislocation density, while the well-known Hall-Petch equation quantifies the effect of the grain size [90-92]. Some of these models developed for bulk materials break down for materials with very fine microstructures. Spaepen and Yu [22], for instance, recently compared the effect of microstructural length scales on the yield stress of various Cu-based materials including multilayers, thin films, and nanocrystalline compacts. They found that the classical Hall-Petch relation tends to overestimate the strength as the relevant microstructural length scale decreases below one micron or so. Furthermore, research on nanocrystalline

materials reveals that when the grain size decreases below a critical value (on the order of 30 to 50 nm), some materials exhibit an inverse Hall-Petch behavior, where the flow stress decreases with decreasing grain size [19, 21]. This behavior has been attributed to grain boundary deformation mechanisms such as grain boundary sliding and rotation that become dominant at very small grain sizes [93].

Some of the models that were developed to explain the size effect in thin-film plasticity, such as discrete dislocation simulations [81, 94], some crystal plasticity theories [94], as well as some strain-gradient plasticity theories [79], also predict unusual unloading behavior for thin films. These models predict a large Bauschinger effect in passivated films with reverse plastic flows already occurring even when the overall stress is still in tension on unloading, while other models do not. Experimental evidence for such an unusual Bauschinger effect is lacking due to difficulties in testing thin films in compression.

In addition to thin-film plastic behavior, elastic properties are of interest as well. Recent measurements of Young's modulus of various freestanding metal films and multilayers, including Cu [56, 60, 96, 97], Ag [56], Al [56, 57, 96], W [96], Au [55, 58], and Cu/Ag multilayers [56], have yielded experimental values that are 20% to 50% smaller than for bulk materials, while other researchers have reported values similar to those of bulk materials [55, 58, 65, 95, 98-100]. This modulus deficit is observed mainly for films deposited with e-beam evaporation and tested using the micro-tensile technique [56-58, 60], although sputtered Au films with ultra fine grains [55] and some electroplated Cu films [97] have also been reported to have lower moduli. Several

mechanisms have been suggested to explain the modulus deficit including incomplete cohesion of grain boundaries, presence of voids or microcracks, and compliant grain boundaries [56].

A number of studies have focused on Cu in particular because of the adoption of Cu metallization in advanced integrated circuits. Flinn [101] and Thouless *et al.* [102] investigated stress development and relaxation in Cu films during thermal cycling using the substrate curvature technique. Keller *et al.* [103] quantitatively studied the effects of film thickness, grain size, and passivation on the yield stress of sputtered thin Cu films on Si substrate using the same technique. Their results showed that the yield stress of Cu films is well described by the dimensional constraint model proposed by Nix [3] combined with classical Hall-Petch grain-size strengthening or Taylor strain hardening. Spolenak *et al.* [104] studied both electroplated and sputter deposited Cu films on substrates and found that the yield stress at room temperature increases with decreasing film thickness for both sets of films. Sputtered films, however, exhibited a higher yield stress than the electroplated films. This was attributed to the different microstructure of these films. Yu and Spaepen [60] measured the stress–strain curves of electron beam evaporated Cu thin films on polyimide substrates using a micro-tensile tester. They reported a 20% modulus deficit and a strong dependence of the yield strength on film thickness.

While understanding the mechanical behavior of Cu films on substrates is important because in many applications Cu films are indeed bonded to a substrate, it is difficult to separate the film thickness effect from grain-size strengthening in films on

substrates. In order to gain better understanding, it is desirable to investigate the behavior of freestanding films. Work on freestanding Cu films can be traced back to the 1960s [105-108]. For rolled Cu foils with thickness varying from 2 to 150 μm , the strength was reported to be independent of film thickness [105, 106]. Oding and Aleksanyan [107] found that the strength of evaporated films decreased by a factor of two when their thickness increased from 1.5 to 4.6 μm . Leidheiser and Sloope [108] studied the stiffness and fracture strength of freestanding thermally evaporated Cu films with thickness ranging from 60 to 500 nm using a circular bulge test technique. They found that the fracture strength of these films varied inversely with film thickness, while the stiffness was the same as for bulk polycrystalline Cu independent of film thickness. No correlation of the mechanical properties with the microstructure of the films was made. Recently, Read and colleagues [97, 109, 110] studied the tensile, fracture and fatigue behavior of freestanding electron-beam evaporated Cu thin films using the micro-tensile test. The Cu films exhibited low ductility, which was attributed to a lack of dislocation sources and a dislocation glide distance limited by the film thickness and fine grain size.

Chapter 3

The plane-strain bulge test technique for thin films[†]

The plane-strain bulge test is a powerful technique for measuring the mechanical properties of thin films and is chosen as the primary mechanical test method in the current study. It has a number of advantages compared with other techniques that are available for thin film mechanical characterization. For example, it eliminates the effect of substrates on the measurement compared with nanoindentation; it is an isothermal measurement which makes it more straightforward for data interpretation compared with the substrate curvature technique; it involves minimal sample handling and has fewer experimental uncertainties compared with the microtensile test.

[†] Based on "*The plane-strain bulge test for thin films*", Y. Xiang, X. Chen, and J.J. Vlassak, *J. Mater. Res.* **20**, 2360-2370 (2005).

In this chapter, the development of the bulge test technique is briefly reviewed. The accuracy and reliability of the plane-strain bulge test in both elastic and plastic regimes are examined through finite element analysis. A versatile sample fabrication process is developed and a computerized bulge test apparatus with high displacement and force measurement resolutions is constructed. Typical experimental procedures and data analyses are demonstrated for Cu thin films.

3.1 A brief review of the bulge test technique

Bulge testing of thin films was first reported by Beams in 1959, as a technique for measuring in-plane mechanical properties of thin films [66]. In the beginning, the technique suffered from a number of problems related to sample processing, handling, and data analysis. The recent rapid development of silicon micromachining technology has made it possible to manufacture bulge test samples with precisely controlled dimensions, and has dramatically reduced sample handling [59, 111]. These improvements have made accurate bulge testing possible. In order to explain the experimental data and relate them to the mechanical properties of the tested films, both theoretical and numerical analyses have been conducted to understand the pressure–deflection relation for membranes with various shapes. Hencky was the first to publish an analytical solution for the elastic deflection of a pressurized circular membrane with fixed edges [112]. Vlassak generalized Hencky’s solution to include the influence of residual stress on the deflection of a membrane [64]. The problem becomes more complex for

non-circular geometries such as square or rectangular membranes. An exact elastic solution for the problem of a pressurized square membrane was given by Levy, but is too complex to be practically useful [113]. A number of researchers have developed approximate solutions using energy minimization methods [59, 111, 114, 115]. Vlassak and Nix [59] derived an accurate expression for the elastic load-deflection behavior of square and rectangular membranes following an approach originally developed by Timoshenko [115]. The effect of residual stress on the membrane deflection was also taken into account. These researchers further found that once the aspect ratio of a rectangular membrane exceeds 4, the deflection at the center of the membrane is nearly independent of the aspect ratio and can be approximated with the exact solution for an infinitely long rectangular membrane, which can be readily derived [59, 115].

The accuracy and reliability of the bulge test has been analyzed by a number of researchers. Itozaki showed that failure to include the initial height of the membrane in the analysis leads to an *apparent* nonlinear elastic behavior of the film [116]. Small *et al.* analyzed the influence of initial film conditions such as film wrinkling, residual stress, and initial height of the membrane using finite element analysis [117, 118]. Vlassak [64] investigated the contribution of the film bending stiffness to the deflection of a membrane. He showed that for typical bulge test geometries, the bending moment is only significant very close to the edge of the membrane and is negligible everywhere else. These analyses, together with new sample preparation techniques based on Si micromachining, have made the bulge test a useful technique to accurately measure the elastic properties of both freestanding films and multilayers across a wide range of materials, such as ceramic,

metal, polymer, etc. [59, 98, 119, 120].

Because the bulge test technique measures isothermal stress–strain curves of freestanding films, it is also ideal for studying plasticity in thin films. Mathematical analyses of the bulge test, however, are based on linear elasticity and may not be applied to the plastic regime. In circular, square, or rectangular membranes with small aspect ratios, the stress and strain in the film are not uniform [64]. As a result, plastic flow does not initiate uniformly in the membrane. Even after the entire membrane has yielded, different parts of the membrane undergo different amounts of plastic deformation and the resulting stress state in the film can be quite complex. These geometries are thus not suitable for studying the plastic properties of thin films. We will show that deformation of rectangular membranes with aspect ratios greater than 4 results in a state that closely approximates plane strain. For thin films in a state of plane strain, the stress and strain are distributed uniformly across the width of the membrane. This feature makes long rectangular membranes especially useful for studying the plastic behavior of thin films. Indeed, a similar approach has been used to study work hardening in thin sheets, although the test geometry is quite different in this case [121].

Simple analytical formulae are established to calculate the stress and strain independently from the applied pressure and the deflection at the center of the membrane [64]. There has been, however, no systematic study of the accuracy of these formulae in the plastic regime. In this chapter, we first review the equations used to analyze bulge test results. Then, a finite element analysis is carried out to verify the accuracy of these equations in the plastic regime. A sample preparation process based on silicon

micromachining technology is used to manufacture long rectangular freestanding Cu membranes. Typical experimental results and data analyses for the Cu thin films are demonstrated and compared with the results from the finite element analysis.

3.2 Finite element analysis

Consider a pressurized rectangular membrane made of an isotropic elastic-plastic material with a power-law stress-stain relationship. Figure 3.1(a) shows a perspective view of the membrane before and after pressure is applied; Figure 3.1(b) is a plan view of the membrane window framed by a Si substrate. The deflection, δ , at the center of a membrane of dimensions $2a \times 2b$ is a function of the applied pressure, various material parameters, and the membrane geometry:

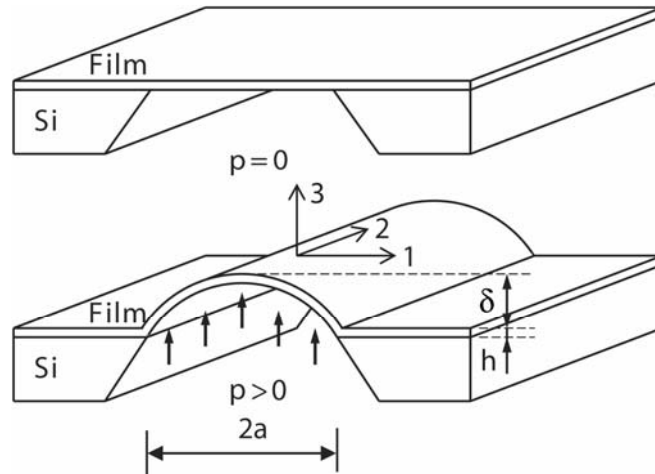
$$\delta = f(p, \sigma_0, E, \sigma_y, \nu, n, a, b, h), \quad (3.1)$$

where p is the applied pressure, σ_0 the in-plane equi-biaxial residual stress in the film, E Young's modulus, ν Poisson's ratio, σ_y the yield stress, n the strain-hardening exponent, and h the film thickness. The dimensionless form of the above function is:

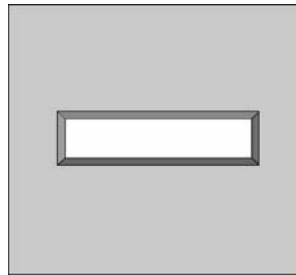
$$\frac{\delta}{a} = F\left(\frac{p}{E}, \frac{\sigma_0}{\sigma_y}, \frac{\sigma_y}{E}, \nu, n, \frac{b}{a}, \frac{h}{a}\right). \quad (3.2)$$

In the elastic regime, the strain-hardening exponent and the yield stress do not enter the equation and equation (3.2) is reduced to

$$\frac{\delta}{a} = F_1\left(\frac{p}{E}, \frac{\sigma_0}{E}, \nu, \frac{b}{a}, \frac{h}{a}\right). \quad (3.3)$$



(a)



(View from the bottom.)

- p** – Applied Pressure
- 2a** – Membrane Window Width
- h** – Membrane Thickness
- δ** – Membrane Deflection

(b)

Figure 3.1: Schematic illustration of the plane-strain bulge test for a long rectangular membrane: (a) Perspective views of the freestanding film before and after a uniform pressure (p) is applied; (b) Plan view of a typical sample showing a long rectangular membrane framed by a Si substrate.

For a linear elastic membrane, this relationship is well approximated by the following functional form [59, 64, 114]

$$p = c_1 (b/a) \frac{\sigma_0 h}{a^2} \delta + c_2 (\nu, b/a) \frac{Eh}{(1-\nu)a^4} \delta^3, \quad (3.4)$$

where c_1 is a constant that depends on the aspect ratio b/a , and c_2 a constant that depends on both Poisson's ratio and the membrane aspect ratio. The above equation is based on the membrane assumption, i.e., the influence of the bending stiffness of a membrane is negligible compared to the contribution of the residual stress. This is so if $\frac{\sigma_0 a^2}{E h^2} \gg 1$. It can be shown with a boundary layer analysis that in that case the effect of the bending stiffness is to reduce the deflection of the membrane by an amount less than the film thickness [64]. The sample dimensions in the present study satisfy this membrane assumption. For rectangular membranes with aspect ratios greater than 4, the assumption of plane strain holds and the pressure–deflection relationship is found to be

$$p = 2 \frac{\sigma_0 h}{a^2} \delta + \frac{4}{3} \frac{Eh}{(1-\nu^2)a^4} \delta^3, \quad (3.5)$$

where $2a$ is the width of the membrane, as shown in Fig. 3.1(a).

The linear elastic analysis becomes invalid once the film deforms plastically. When subjected to a uniform pressure, an infinitely long membrane with negligible bending stiffness takes the shape of a section of a cylinder with a circular cross-section [64]. The stress and strain in the membrane are then uniform across the width of the

membrane independent of whether the film deforms elastically or plastically, and are given by

$$\sigma = \frac{p(a^2 + \delta^2)}{2\delta h} \text{ and } \varepsilon = \varepsilon_0 + \frac{a^2 + \delta^2}{2a\delta} \arcsin\left(\frac{2a\delta}{a^2 + \delta^2}\right) - 1, \quad (3.6)$$

where ε_0 is the residual strain in the film. When the deflection is much smaller than the membrane width, i.e., $\delta \ll a$, the above equations reduce to

$$\sigma = \frac{pa^2}{2\delta h} \text{ and } \varepsilon = \varepsilon_0 + \frac{2\delta^2}{3a^2}. \quad (3.7)$$

For strains less than 1% and the membrane aspect ratios used in this study, the difference between equations (3.6) and (3.7) is negligible. When the deflection δ is large compared to a , equations (3.6) should be used.

Because there is no analytical solution for the plastic deflection of rectangular membranes of finite length, the finite element method (FEM) is used to evaluate the accuracy of equations (3.6) and (3.7). The parameters governing plastic deformation of the membrane are given in equation (3.2). Since we are interested in the plastic flow behavior of very thin films, the effects of b/a , n and σ_0/σ_y are examined only for the limit where $h \ll 2a$. Finite element calculations are performed using the commercial code ABAQUS. Plastic deformation is modeled using a large-deformation description combined with J_2 flow theory. The rectangular membrane is represented by 1000 three-dimensional, eight-node, quadratic, thin-shell elements (element S8R5, with 5 degrees of freedom at each node and with reduced integration) that account for finite rotations of the middle surface. The thin film is made of an elastic-plastic material governed by a power-

law constitutive equation with a strain-hardening exponent n in uniaxial tension:

$$\begin{aligned} \frac{\sigma}{\sigma_y} &= \frac{\varepsilon}{\varepsilon_y}, \text{ when } \sigma \leq \sigma_y \\ \frac{\sigma}{\sigma_y} &= \left(\frac{\varepsilon}{\varepsilon_y} \right)^n, \text{ when } \sigma > \sigma_y. \end{aligned} \quad (3.8)$$

The edges of the membrane are assumed to be clamped since the substrate suppresses any rotation of the edges.

Using this finite element model, the deflection at the center of a rectangular membrane is calculated as a function of applied pressure, membrane aspect ratio, and work-hardening exponent. The residual stress was fixed at 60% of the yield stress; the elastic modulus was taken to be 1200 times the yield stress; the t/a ratio was 3×10^{-3} . The resulting pressure–deflection relationships are converted into plane-strain stress–strain curves using equations (3.6) and plotted in Fig. 3.2. These curves are then compared with the plane-strain stress–strain relationship directly calculated from the uniaxial behavior in equation (3.8) using finite elements and denoted by “input” in Fig. 3.2. All stresses in Fig. 3.2 are normalized by the plane-strain yield stress, σ_y^{PS} , defined as the yield stress for the input plane-strain stress–strain curve calculated using finite elements; the strains are normalized by the corresponding yield strain (ε_y^{PS}). The numerical results for the plane-strain $\sigma - \varepsilon$ relationships are presented in Figs. 3.2(a), 3.2(b), and 3.2(c), for $n = 0, 0.2, 0.5$, respectively. For each value of n , stress–strain curves obtained from membranes with three different aspect ratios are compared with the input material behavior. It can be seen that for all strain-hardening exponents considered in this study, the transverse stress and

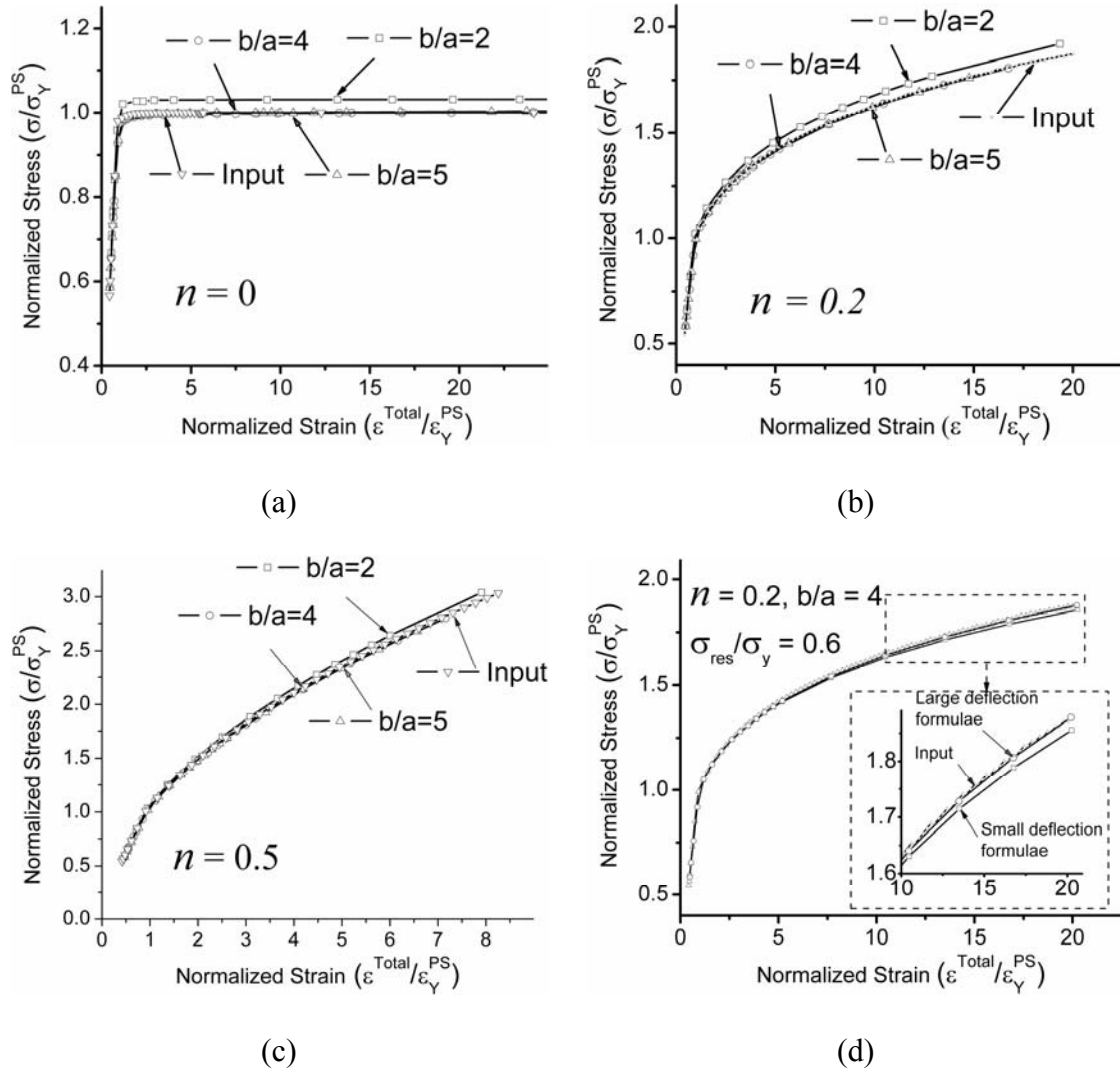


Figure 3.2: The plane-strain stress–strain curves obtained from the finite element method for various aspect ratios [$b/a=2, 4$ and 5] and for $n = 0$ (a), $n = 0.2$ (b), and $n = 0.5$ (c); (d) The plane-strain stress–strain curves calculated using small and large deformation formulae for a membrane with $n = 0.2$ and $b/a = 4$.

strain predicted from equations (3.6) are highly accurate as long as the membrane aspect ratio is at least 4. Even membranes with $b/a=2$ show good agreement, especially for larger values of the work-hardening exponent. To illustrate the difference between small and large deformation formulae, Fig. 3.2(d) shows the stress–strain curves calculated using both sets of equations for a membrane with $b/a=4$. As expected, both curves coincide with the input curve when the applied strain is small. At a strain of 1%, the $\sigma - \varepsilon$ relationship calculated using the small deformation formulae, equations (3.7), is approximately 1.5% lower than the input curve; the curve calculated using the large deformation formulae, equations (3.6), is indistinguishable from the input curve at both small and large strains. The FEM output data also verify that the longitudinal strain does not change with the applied strain, i.e., the plane-strain condition is well satisfied, and the transverse stress and strain are distributed uniformly across the width of the membrane for membranes with aspect ratios equal or greater than 4.

The effect of the residual stress on the plane-strain bulge test was also investigated using the finite element method. Fig. 3.3 shows the pressure–deflection curves for films with various levels of residual stress and the corresponding plane-strain stress–strain curves obtained using equations (3.6) for both ideally plastic [Figs. 3.3(a) and 3.3(b)] and strain-hardening [Figs. 3.3(c) and 3.3(d)] materials. It is found that the residual stress affects mainly the elastic deflection [Figs. 3.3(a) and 3.3(c)] and the initial point of yield [Figs. 3.3(a) and 3.3(b)] as expected from the yield criterion. If the material obeys the von Mises yield criterion, the stress at first yield varies from the uniaxial yield stress, σ_y , if the residual stress is equal to the yield stress, to $\sigma_y / \sqrt{1-\nu + \nu^2}$ if the

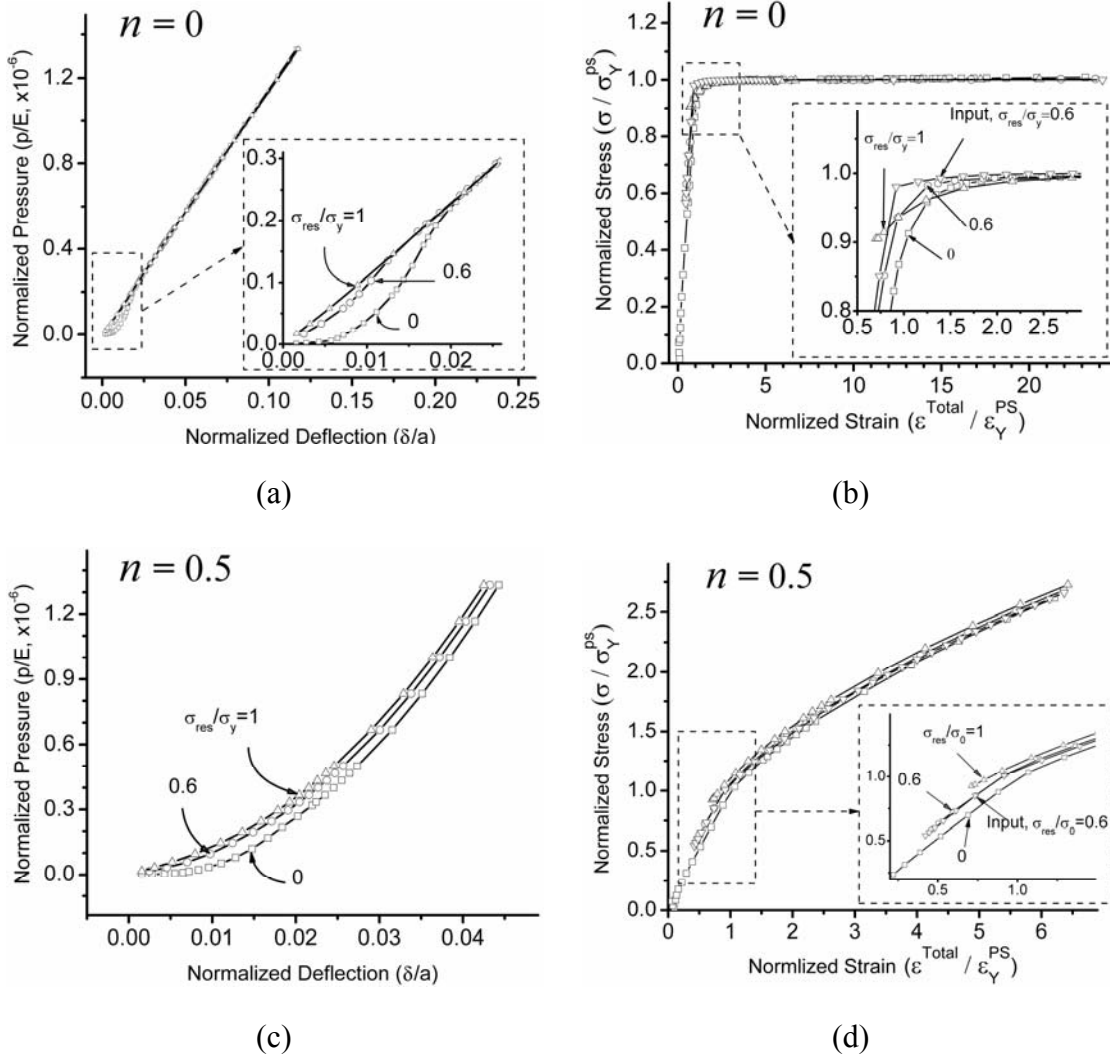


Figure 3.3: The pressure–deflection curves and corresponding plane-strain stress–strain curves obtained from the finite element method for an ideally plastic material [(a, b) $n = 0$] and a strain-hardening material [(c, d) $n = 0.5$] with various levels of residual stress ($\sigma_{res}/\sigma_y = 0, 0.6, \text{ and } 1$).

residual stress is zero. Once the film deforms plastically, the effect of the residual stress is quickly wiped out: for ideally plastic material, the residual stress has no effect on the rest of the stress–strain curve [Fig. 3.3(b)]; for strain-hardening material, the effect amounts to a small shift along the strain axis [Fig. 3.3(d)]. The plane-strain stress–strain curves [Figs. 3.3(b) and 3.3(d)] can be converted into equivalent stress–equivalent strain curves [Figs. 3.4(a) and 3.4(b)], using the method described in the Appendix B. The small discrepancy caused by the biaxial residual stress in the plane-strain stress–strain curves is completely eliminated in the equivalent uniaxial stress–strain curves.

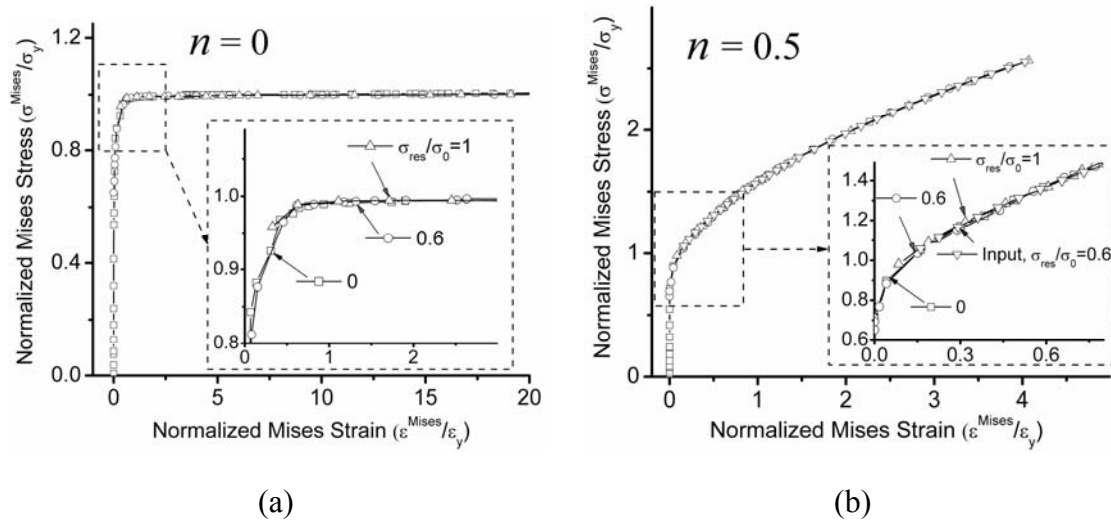


Figure 3.4: The von Mises stress–strain curves for the ideally plastic material [(a) $n = 0$, corresponding to Fig. 3.3(b)] and strain-hardening material [(b) $n = 0.5$, corresponding to Fig. 3.3(d)] with various levels of residual stress ($\sigma_{res}/\sigma_y = 0, 0.6$, and 1).

3.3 Sample preparation

In this study, a 2.8 μm electroplated, Cu film was tested to illustrate the methodology of the plane-strain bulge test. Freestanding Cu membranes were prepared using standard photolithography and silicon micromachining techniques. As shown in Fig. 3.5, we start with a (100) Si wafer coated on both sides with low pressure chemical vapor deposited (LPCVD) Si_3N_4 film. First, a 30nm TaN adhesive layer and a thin Cu seed layer were sputter deposited onto the Si_3N_4 followed by electrodeposition of the Cu film. The as-deposited film was annealed for one hour in vacuum at 600°C to stabilize the microstructure. A layer of benzocyclobutene (BCB) was spincoated onto the Cu film to protect it during subsequent processing. Photolithography is used to define long rectangular windows (with an aspect ratio of 4:1) in the LPCVD Si_3N_4 coating on the backside of the substrate and with the edges of the rectangles aligned along the $\langle 110 \rangle$ directions in the Si substrate. The Si substrate is etched anisotropically (etch selectivity between (100) and (111) crystal plane is approximately 50:1.) using a potassium hydroxide (KOH) based wet etch to create freestanding membranes that consist of the Si_3N_4 coating and the Cu film. The size of the membranes is $2.4 \times 10 \text{ mm}^2$ (with $2a = 2.4 \text{ mm}$ in Fig. 3.1). Finally, freestanding Cu films are obtained by removing the Si_3N_4 and TaN using reactive ion etching (RIE) and by dissolving the protective BCB layer in an organic solvent. The advantage of the sample preparation process is that there are no restrictions on the type of film or the way the film is deposited on the substrate, as long as the Si_3N_4 etch is selective with respect to the film of interest. An alternate technique would consist

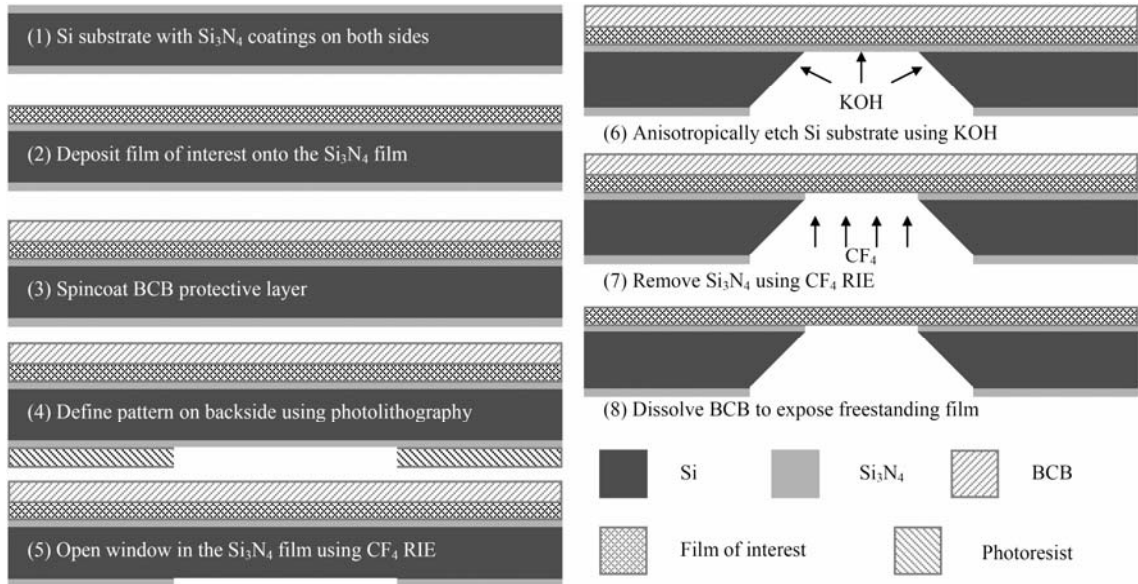


Figure 3.5: Schematic illustration of the sample preparation process using the standard photolithography and Si micromachining technology.

of first preparing freestanding Si_3N_4 membranes, after which the film of interest can be deposited directly onto the Si_3N_4 membrane. By removing the Si_3N_4 using reactive ion etching (RIE), a freestanding film is obtained. This process is easier, but much less generally applicable: the Si_3N_4 membranes are fragile and there may be limitations with respect to which deposition techniques can be used. Moreover, for high energy deposition techniques such as sputtering, the structure of the film deposited on the Si_3N_4 membrane can be different from that on the bulk Si substrate. The Si_3N_4 membrane does not conduct the heat of condensation away as efficiently as the Si substrate during the film deposition

process and the film over the membrane are exposed to much higher temperatures than elsewhere. The two methods are complimentary to each other and can be applied to a wide range of materials. Technical details and step-by-step instructions for the sample preparation are given in the Appendix A.

Note that a residual tension must be maintained in the freestanding film, since any in-plane compressive stress will cause the film to buckle due to its small bending stiffness [117, 118]. Buckles near the edge of the membrane disappear only gradually as pressure is applied during an experiment, rendering the pressure–deflection data meaningless. If the stress in the film of interest is compressive, the LPCVD Si_3N_4 coating beneath the film can be kept and the composite membrane tested. The Si_3N_4 coating typically has a high tensile residual stress and the overall stress in the composite membrane may be kept in tension if the thickness ratio of the two layers is properly selected. The mechanical properties of the film of interest can be measured by subtracting the elastic contribution of the Si_3N_4 film, which can be readily determined independently [120]. This composite technique makes it possible not only to measure films with residual compression, but also to deform metal films alternating in tension and in compression. In this case, the Si_3N_4 film acts as a spring that drives the metal film into compression after unloading. This technique will be applied to Cu and Al films to study the Bauschinger effect in thin metal films and a more detailed description is given in Chapter 6.

3.4 Experimental setup

A schematic of the bulge test apparatus used in this study is shown in Fig. 3.6. The sample is clamped onto a sample holder. Pressure is applied by pumping water into the cavity under the film using a syringe pump driven by a stepper motor. The deflection at the center of the membrane is measured by means of a laser interferometer with a displacement resolution of 316.5 nm, i.e., half the wavelength of the He-Ne laser. At the beginning of each experiment, the interferometer is used to ensure that the membrane is

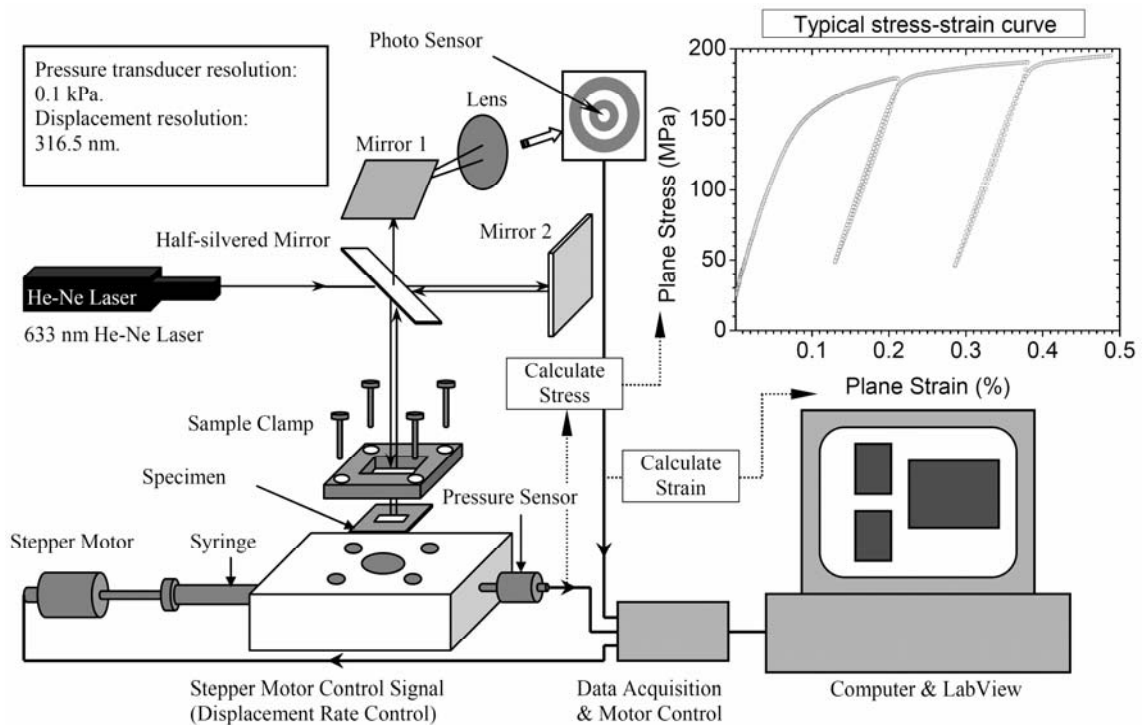


Figure 3.6: Schematic illustration of the bulge test apparatus.

flat and level with the surrounding substrate. The pressure is measured using a pressure gauge with a resolution of 0.1 kPa. The experiment is controlled by a computer via a LabView based program and a data acquisition system. A detailed technical description of the bulge test apparatus is given in Appendix A.

3.5 Results and discussion

Typical pressure–deflection data for the 2.8 μm freestanding Cu film are presented in Fig. 3.7(a). The Cu film was loaded to a maximum deflection of approximately 300 μm , at which point it ruptured. The loading segment was interrupted by two brief unloading cycles to evaluate the elastic properties of the film. Because of the large deflection compared to the membrane width, the large deformation equations (3.6) are used to calculate the plane-strain stress–strain relationship presented in Fig. 3.7(b). The fracture strain is approximately 4%. From the stress–strain curve, the residual stress in the film is determined to be 66 MPa. The yield stress is defined at a specific offset plastic strain: for example, the yield stress at 0.2% plastic strain is found to be 125MPa.

The plane strain modulus $M = \frac{E}{1-\nu^2}$ is determined from the slopes of the unloading curves and is 130 ± 5 GPa, in good agreement with the value one would expect based on the crystallographic texture of the film [30]. The plane-strain stress–strain curve [Fig. 3.7(b)] obtained using Eqs. (3.6) is converted into an equivalent uniaxial stress–strain relationship [Fig. 3.7(d)], using the method described in Appendix B. The evolution of

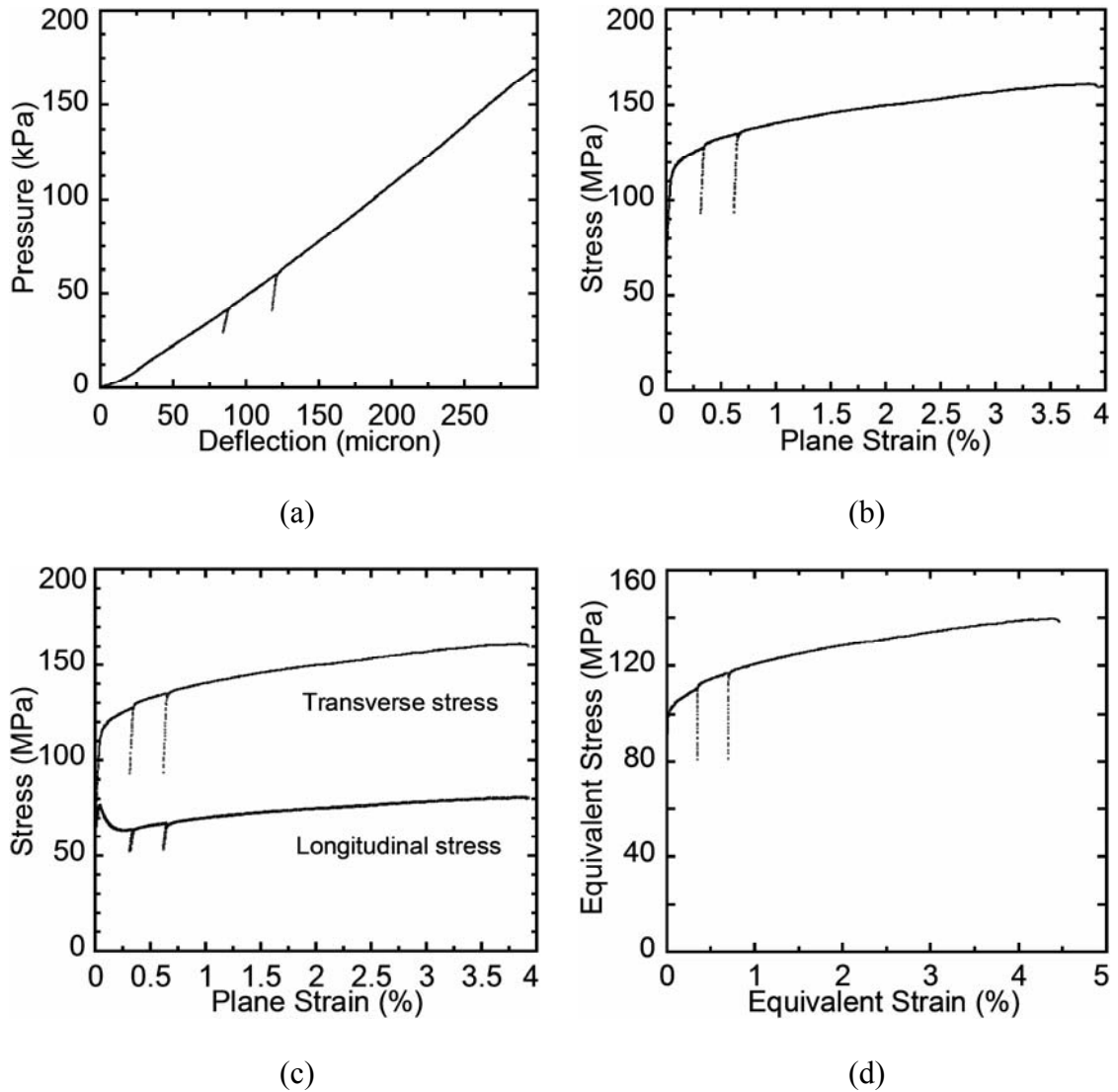


Figure 3.7: Experimental results for a 2.8 μm electroplated Cu film: (a) The pressure–deflection curve with two brief unloading cycles; (b) The plane-strain strain–stress curve; (c) Evolution of the transverse and longitudinal stress with applied strain; (d) The von Mises equivalent uniaxial stress–strain curve.

the transverse and longitudinal stress with applied strain is presented in Fig. 3.7(c). The longitudinal stress first increases with applied strain and then decreases when the film starts yielding. At larger strains, the longitudinal stress increases with applied strain and is equal to half of the transverse stress, as expected for plane-strain plastic deformation. The dip in the longitudinal stress evolution curve arises because of the relatively high biaxial residual stress in the membrane: at first, the longitudinal stress is greater than half the transverse stress and decrease until its value is half the transverse stress. At this point, it starts to increase along with the transverse stress due to work hardening. When the residual stress is below a critical level, no such dip is observed. The equivalent uniaxial stress–strain curve is plotted in Fig. 3.7(d). The strain-hardening exponent obtained for this curve is 0.36 , which is close to the value for bulk Cu [92].

The above analysis was verified using the finite element method. The film thickness and membrane geometry were taken identical to the tested sample. Experimental values for elastic ($M = 130\text{GPa}$) and plastic [Fig. 3.7(d)] properties were used as input for the material behavior in the FEM simulation. Poisson's ratio was taken to be 0.33. The pressure–deflection curve obtained from FEM is found to be in good agreement with the experimental data [Fig. 3.8(a)]. The load-deflection data obtained from FEM is then converted to a plane-strain stress–strain curve using equations (3.7). Figure 3.8(b) compares this stress–strain curve with the experimental curve. The agreement between numerical and experimental results is excellent and validates the experimental data analysis.

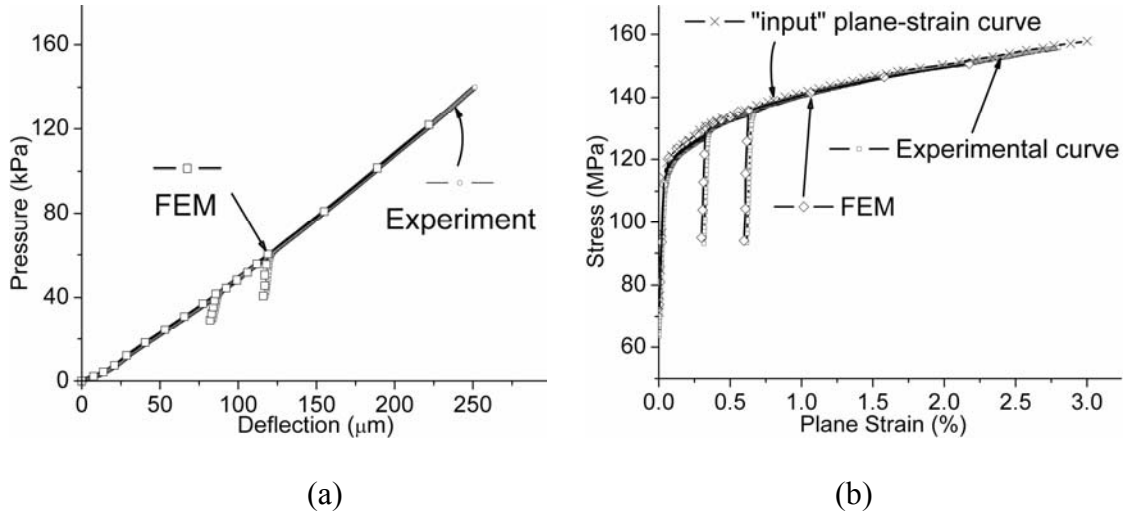


Figure 3.8: Parallel FEM analysis for the experimental data: (a) The pressure–deflection curve obtained with FEM is in good agreement with the experimental curve; (b) The corresponding plane-strain stress–strain curves are compared with the “input” plane-strain behavior.

3.6 Summary

We have used the finite element method to analyze the plane-strain bulge test as a technique for measuring the mechanical properties of thin films, with a particular emphasis on the effects of sample aspect ratio, strain-hardening exponent, and residual stress. It is found that the analytical stress and strain formulae used to analyze the bulge test are highly accurate and that the plane-strain condition is well satisfied for all

materials with strain-hardening exponents ranging from 0 to 0.5, as long as the membrane aspect ratio is 4 or greater. The residual stress affects mainly the elastic deflection of the membrane and changes the initial point of yield in the plane-strain stress–strain curve, but there is little or no effect on the rest of the stress–strain curve. The effect of the residual stress can be completely eliminated by converting the plane-strain curve into its equivalent uniaxial relationship (the von Mises stress–strain curve). The technique was applied to an electroplated Cu film. Si micromachining techniques were used to fabricate freestanding Cu membranes. Experimental results for the Cu film are in good agreement with the numerical analysis.

Chapter 4

The mechanical properties of freestanding electroplated Cu thin films[†]

4.1 Objective and overview

In this chapter, we systematically investigate the effects of microstructure on the mechanical properties of freestanding electroplated Cu thin films. Cu films with thickness ranging from 0.9 – 3.0 μm were prepared by means of electroplating followed by proper heat treatments. The film microstructure was characterized as a function of film thickness and heat treatment. The mechanical properties were determined from the stress–strain curves measured using the plane-strain bulge test. The effects of film thickness, grain size, and crystallographic texture on the mechanical properties are quantitatively evaluated.

[†] Based on "*The mechanical properties of freestanding electroplated Cu thin films*", Y. Xiang, T.Y. Tsui, and J.J. Vlassak, *Acta Mater.*, in review (2005).

4.2 Experimental

Silicon wafers with (100) orientation were coated on both surfaces with 80 nm of Si₃N₄ using low-pressure chemical vapor deposition (LPCVD). Prior to the Cu plating process, a 20 nm TaN adhesion layer and a thin Cu seed layer were sputter deposited onto the Si₃N₄ coating. Cu films with thickness ranging from 0.9 to 3.0 μm were electroplated using a commercial plating process [30]. Immediately after the electroplating process, the Cu films have a grain size on the order of a few tens of nanometers. As-plated films recrystallize spontaneously at room temperature over a period of a few hours to several days. This is a phenomenon commonly observed for electroplated films [30-33]. In this work, only fully recrystallized films were investigated. These films will be called “as-deposited films”. In order to increase the grain size, half of the films were annealed for one hour in a vacuum furnace ($\sim 10^{-7}$ Torr) at 600 °C. These films will be referred to as “annealed films”. As listed in Table 4.1, six sets of samples were prepared for this study.

The microstructure of the Cu films was characterized using focused ion beam microscopy (FIB) in a FEI DualBeam FIB/SEM DB235 system. Plan-view transmission electron microscope (TEM) samples were prepared and the sub-grain structure of the films was characterized in a Philips TEM Model 420T before and after deformation. The crystallographic texture of the films was determined with x-ray diffraction (XRD) in a Siemens D5000 diffractometer [30]. The surface topology was analyzed using scanning electron microscopy (SEM) in the FEI DualBeam system and with atomic force microscopy (AFM) in a Nanoscope IIIA Multimode STM (Digital Instruments).

The stress–strain curves of these films were measured by means of the plane-strain bulge test. The Cu films were tested at a nominal constant strain rate of $1.3 \times 10^{-6} \text{ s}^{-1}$. Partial unloading cycles were imposed to extract the elastic properties of the films. All films were loaded until final rupture.

4.3 Results

4.3.1 Microstructural characterization

Table 4.1 summarizes key microstructural information for the Cu films in this study. The grain structure of both as-deposited and annealed films is shown in the FIB micrographs in Fig. 4.1. As is evident from the micrographs in Figs. 4.1(a) – (c), as-deposited films have a very high incidence of twinning. The films show evidence of abnormal grain growth and a few $\langle 100 \rangle$ grains as large as 6–8 μm are observed. If only regular grain boundaries are counted, the average grain size is approximately 1.9 μm in all as-deposited films independent of film thickness. However, if twin boundaries are counted as grain boundaries, the average grain size is much smaller and scales with film thickness. The average grain sizes obtained using both approaches are tabulated in Table 4.1. After annealing at 600 °C for one hour, normal grain growth is observed in all films [Figs. 4.1(d) – (f)]. The average grain size of the annealed films increases significantly with film thickness [Table 4.1]; abnormal grains grow only slightly to a size of approximately 8–9 μm .

The orientation distribution functions (ODF) of the films were calculated from the XRD data [30] following the methodology described in [122]. They are presented in Fig. 4.2 for both as-deposited and annealed films. The as-deposited films generally have textures with distinct $\langle 111 \rangle$, $\langle 100 \rangle$, and $\langle 110 \rangle$ fiber components in addition to a significant fraction of randomly oriented grains. The texture of the thinnest films is dominated by a sharp $\langle 111 \rangle$ fiber component, but this component decreases with increasing film thickness, while the random texture component increases. The volume fraction of the $\langle 111 \rangle$ component calculated from the ODFs is listed as a function of film thickness in Table 4.1. Annealing does not produce significant changes in the texture. Only a slight weakening of the $\langle 111 \rangle$ texture in the thinner films was observed [Table 4.1].

Table 4.1: Summary of results.

Film set	Film thickness h (μm)	Mean grain size (μm)		Fraction of $\langle 111 \rangle$ texture	Plane-strain modulus (GPa)	0.2%- σ_y (MPa)
		Regular grain	Twin			
As-deposited ^a	0.9	1.82 ± 0.57	0.41 ± 0.02	58	154 ± 5	294.9 ± 1.3
	1.8	1.91 ± 0.09	0.53 ± 0.01	42	143 ± 4	265.5 ± 1.6
	3.0	1.95 ± 0.37	0.65 ± 0.18	30	135 ± 5	252.3 ± 1.2
Annealed ^b	0.9	2.99 ± 0.18	0.98 ± 0.14	52	N/A ^c	N/A ^c
	1.8	3.00 ± 0.43	1.34 ± 0.34	40	138 ± 3	161.1 ± 5.3
	3.0	6.13 ± 0.38	2.47 ± 0.3	31	119 ± 6	119.6 ± 4.8

^a After spontaneous recrystallization at room temperature;

^b Anneal condition: 600 °C at 10^{-7} Torr for 1 hr;

^c The annealed 0.9 μm films broke at an early stage during the bulge test.

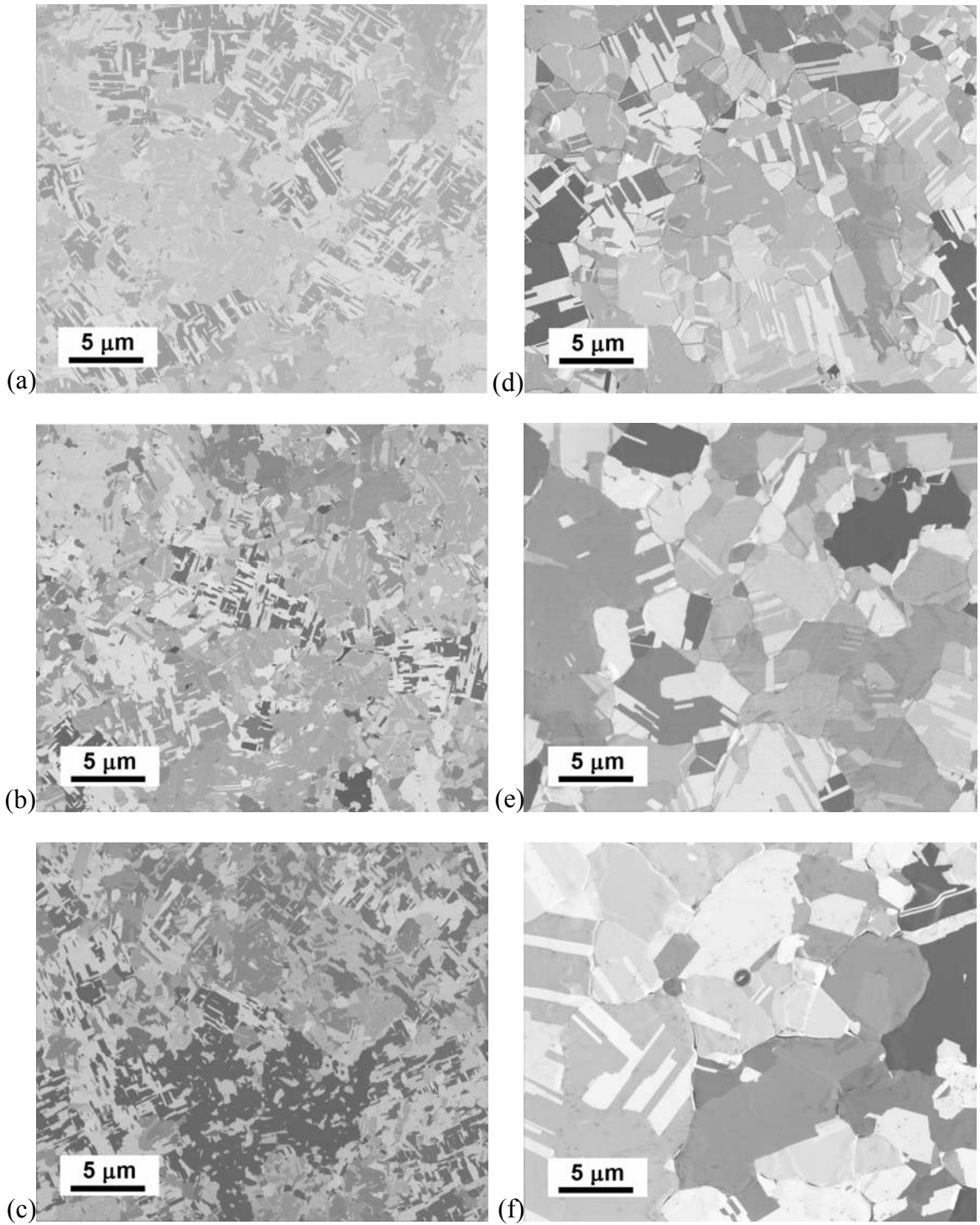


Figure 4.1: Focused ion beam (FIB) micrographs showing the grain structure of as-deposited [(a), (b), and (c) for $h = 0.9, 1.8,$ and $3.0 \mu\text{m}$, respectively] and annealed [(d), (e), and (f) for $h = 0.9, 1.8,$ and $3.0 \mu\text{m}$, respectively] Cu films.

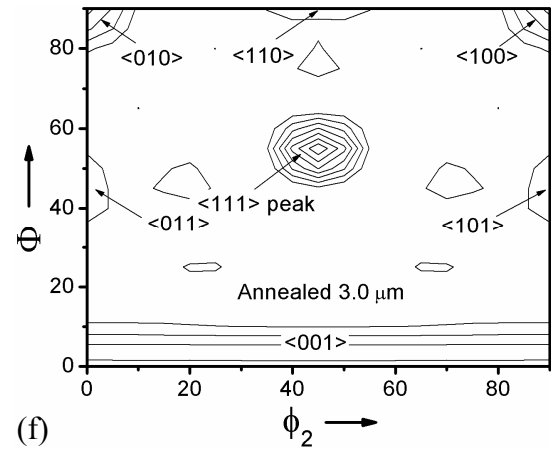
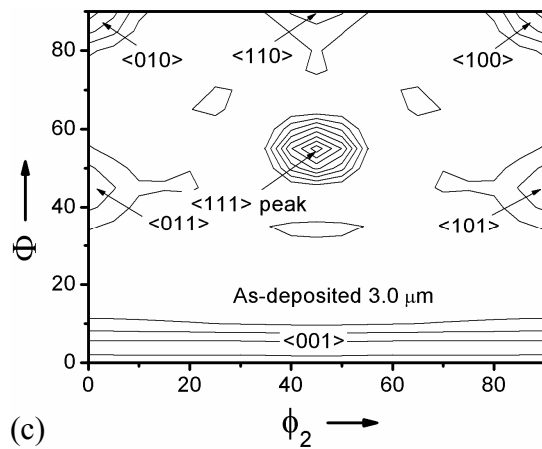
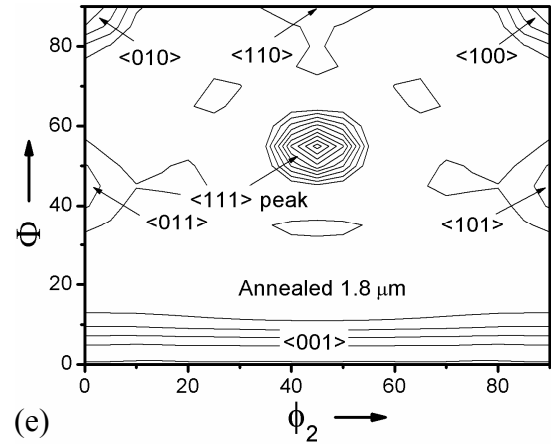
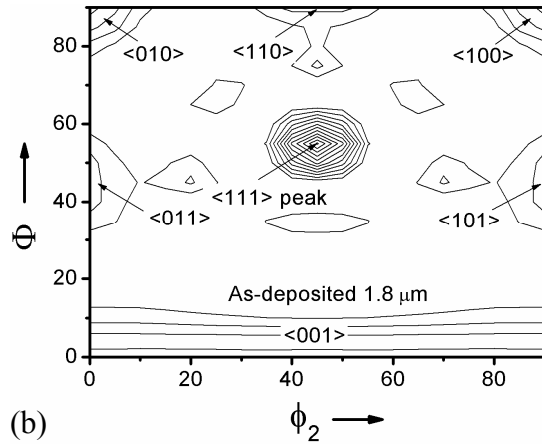
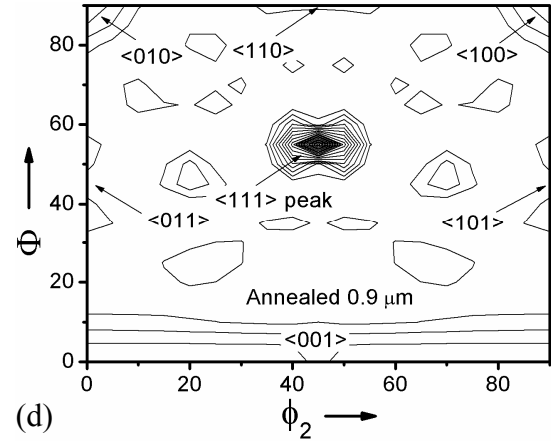
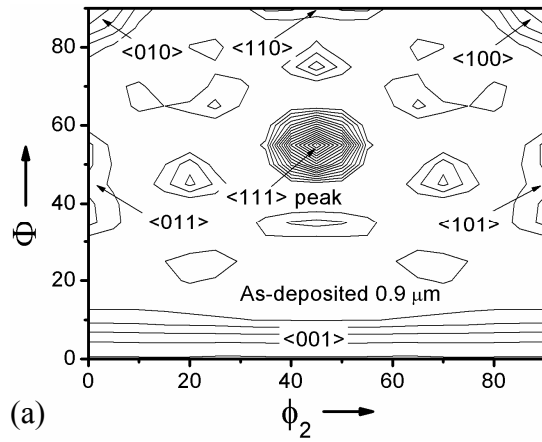


Figure 4.2: The orientation distribution function (ODF) of as-deposited [(a), (b), and (c) for $h = 0.9, 1.8,$ and $3.0 \mu\text{m}$, respectively] and annealed [(d), (e), and (f) for $h = 0.9, 1.8,$ and $3.0 \mu\text{m}$, respectively] Cu films as a function of the three Euler angles.

The plan-view TEM images in Fig. 4.3 reveal the microstructure of some of the films before and after deformation. The micrographs in Figs. 4.3(a) and 4.3(b) are for an as-deposited 1.8 μm film before deformation. The film is polycrystalline with many growth twins [Fig. 4.3(a)], confirming the FIB results. At higher magnification [Fig. 4.3(b)], areas with much smaller grains can be observed. Presumably, these areas did not fully recrystallize after the electroplating process. It should be noted that this morphology is distinctly different from the porous sub-grain structure composed of agglomerated spheroids observed by Read *et al.* in Cu electrodeposits [97]. Figure 4.3(c) shows a micrograph of a 1.8 μm film after annealing. The heat treatment results in a significant increase in grain size. In some grains, a high density of slip traces is observed [Fig. 4.3(c)]. These slip traces form in the annealed films because of the thermal mismatch between film and substrate when the samples are cooled down after annealing. Annealed films are subjected to a strain of approximately 0.7% during cooling and they have consequently a relatively high dislocation density. Figure 4.3(d) shows a typical micrograph for an annealed 3.0 μm film after deformation to approximately 3% of plastic strain. High dislocation densities are found in most grains of the deformed film.

While as-deposited films have a smooth surface, annealed films show significant topography near the grain boundaries. Figure 4.4 presents AFM results for the surface morphology of annealed 1.8 μm [Figs. 4.4(a) and 4.4(b)] and 3.0 μm [Figs. 4.4(c) and 4.4(d)] films. A significant degree of grooving and hillocking is observed along high-angle grain boundaries in both films [Figs. 4.4(a) and 4.4(c)]. Thicker films have deeper and better-defined grain boundary grooves than thinner films. Cross-sectional depth

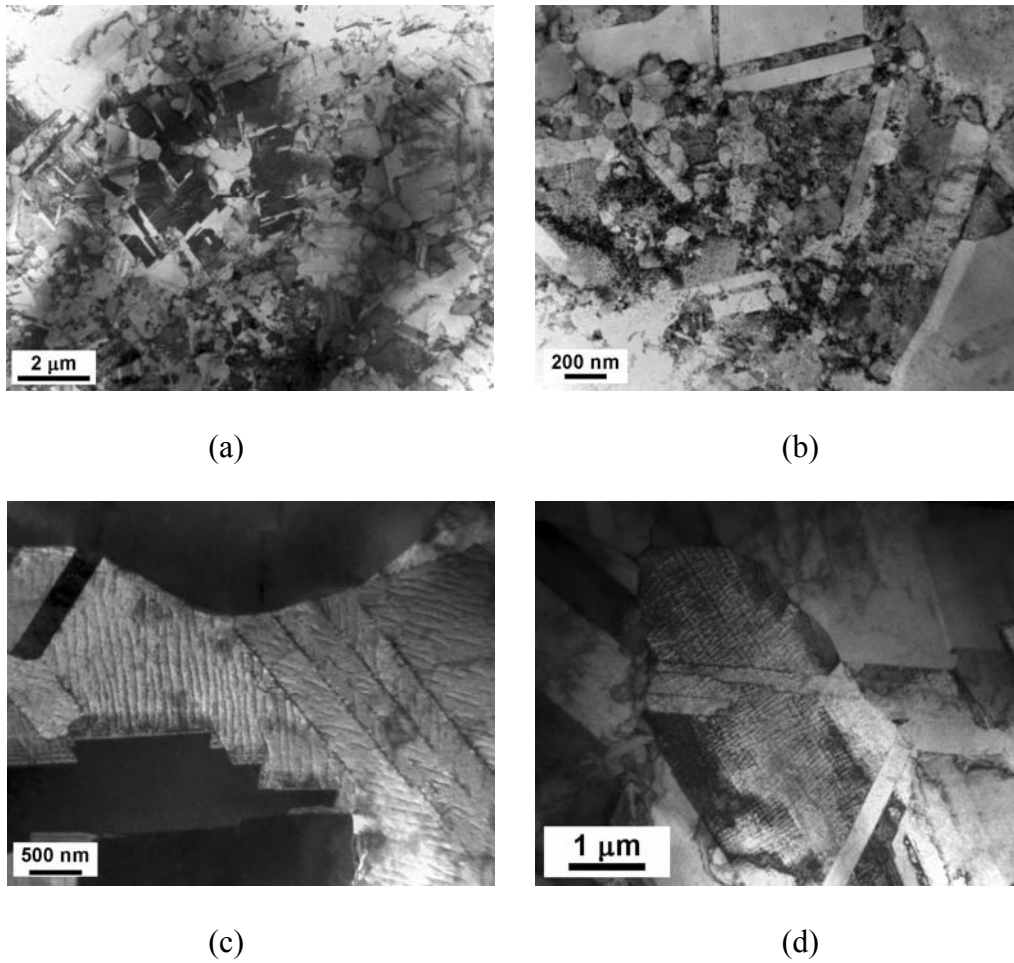


Figure 4.3: TEM micrographs showing the grain structure of a 1.8 μm untested Cu film before [(a) and (b)] and after [(c)] annealing, and a 3.0 μm annealed Cu film after the bulge test [(d)].

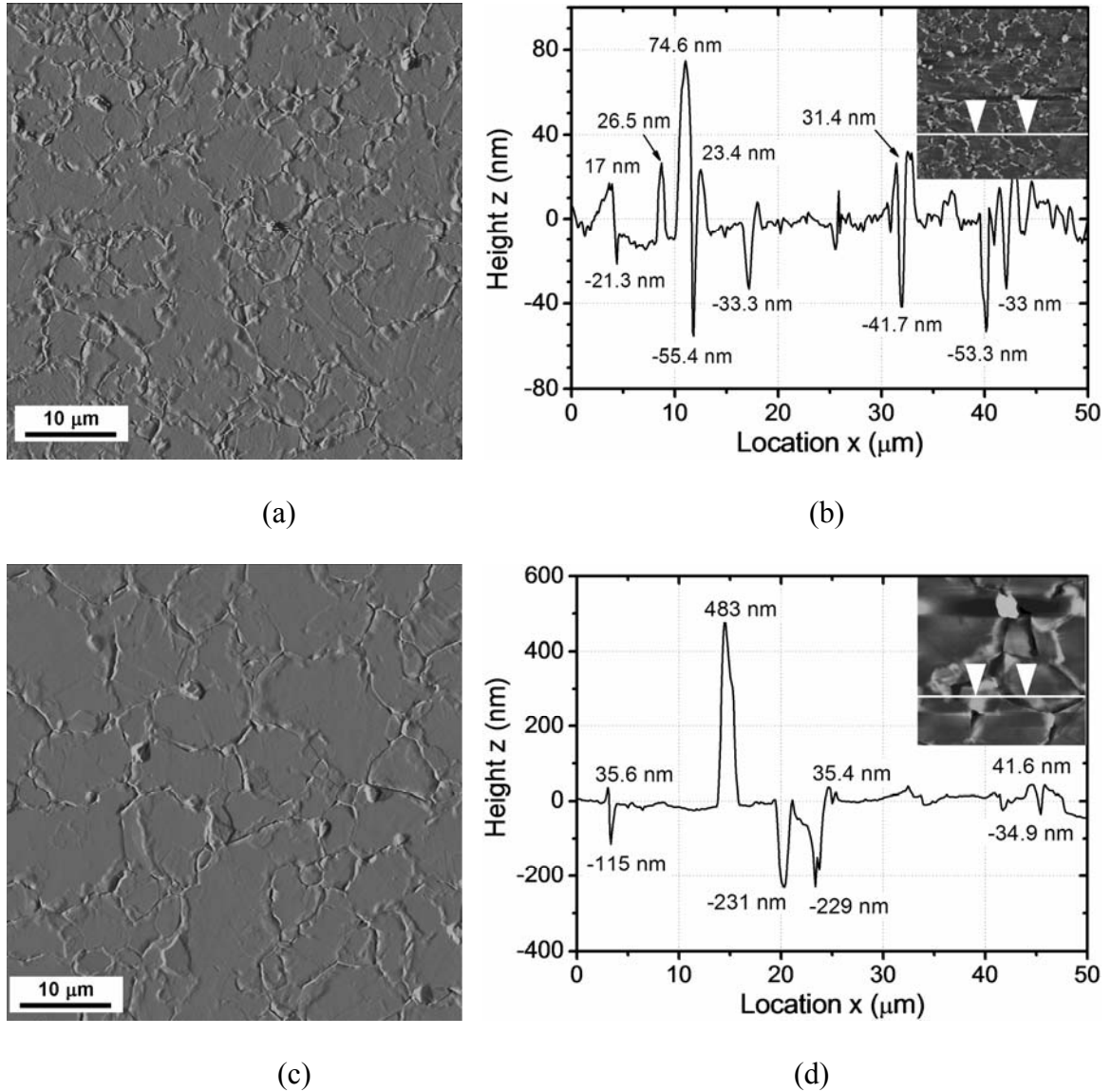


Figure 4.4: AFM results showing grain boundary morphology of annealed 1.8 μm [(a) and (b)] and 3.0 μm [(c) and (d)] Cu films. (a) and (c): Plan-view in deflection mode; (b) and (d): Cross-sectional profile showing the extrusion heights and groove depths.

profiles are shown in Fig. 4.4(b) and 4.4(d). Deep grooves along the grain boundary are often accompanied with hillocks on either side of the grain boundary, suggesting a mass flux from the grain boundaries to the film surface during annealing [123]. The average depth of the grooves is approximately 40 nm for the 1.8 μm film and 190 nm for the 3.0 μm film. Similar observations on grain boundary morphological changes in annealed Cu films have been reported by Joo *et al.* [124].

4.3.2 Mechanical properties

Typical stress - strain curves for as-deposited and annealed Cu films are presented in Fig. 4.5. No data for the annealed 0.9 μm films were obtained because the membranes fractured early in the test. A maximum strain of approximately 4.5% was obtained for the annealed 3.0 μm films (only the first 1.5% is shown in Fig. 4.5). The residual stress in the films is on the order of 100 MPa before annealing and decreases after the heat treatment. The plane-strain modulus, $M=E/(1-\nu^2)$, where E is Young's modulus and ν Poisson's ratio, is obtained from the slopes of the unloading curves and is plotted as a function of the film thickness in Fig. 4.6 for both as-deposited and annealed films. Before annealing, the plane-strain modulus varies from 138 to 151 GPa with decreasing film thickness. Annealing results in a slight decrease of the stiffness of the films. For reference, the plane-strain modulus of bulk, polycrystalline Cu is approximately 136 GPa [125]. As-deposited, thicker films have a more gradual transition from elastic to plastic behavior compared to thinner films. For the same thickness,

annealing leads to a much sharper transition in all films. After the films yield completely, there is no significant difference in the strain-hardening behavior of as-deposited and annealed films. In this study, the plane-strain yield stress, σ_y is defined at an offset plastic strain of 0.2%. The corresponding values are tabulated in Table 4.1 and are plotted as a function of film thickness in Fig. 4.7(a). The yield stress increases slightly with decreasing film thickness and drops significantly after annealing.

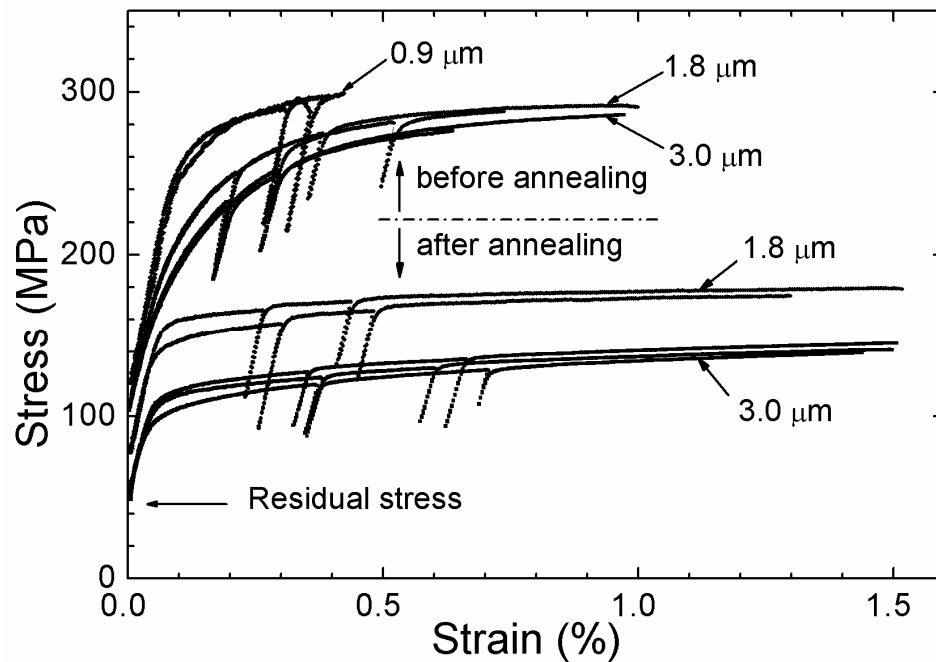


Figure 4.5: The plane-strain stress–strain curves of freestanding electroplated Cu films.

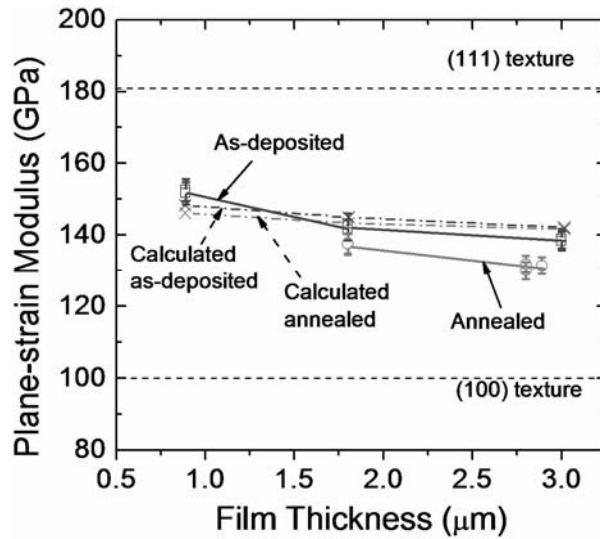


Figure 4.6: The variation of stiffness with film thickness and heat treatment.

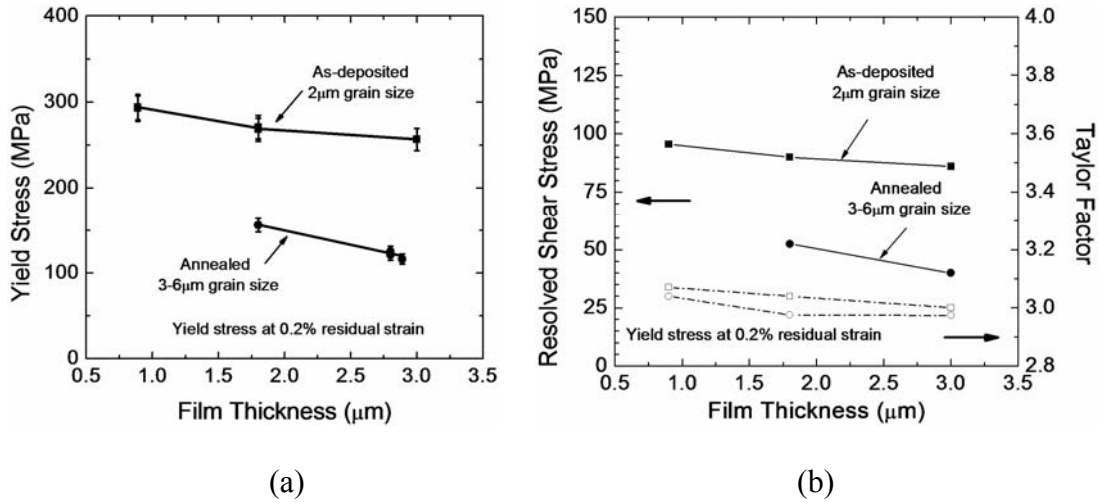


Figure 4.7: The plane-strain yield stress (a), the resolved shear stress (b) and the plane-strain Taylor factor (b) as a function of film thickness and heat treatment.

4.4 Discussion

4.4.1 Elastic modulus

The stiffness of the Cu films increases with decreasing film thickness for both as-deposited and annealed films. This variation is related to the change in crystallographic texture of these films since Cu is an elastically anisotropic material with a stiffness that is strongly orientation dependent. For example, the theoretical plane-strain modulus of Cu films with a pure $\langle 111 \rangle$ -, $\langle 110 \rangle$ - and $\langle 100 \rangle$ -fiber texture can be calculated from the single-crystal elastic constants of bulk Cu to be 181 GPa, 156 GPa and 99 GPa, respectively. With reference to Table 4.1, the $\langle 111 \rangle$ -fiber texture component is present in all films, and the volume fraction of this component increases with decreasing film thickness. Thus, one would expect the modulus of the Cu films to increase with the volume fraction of the $\langle 111 \rangle$ -texture component. To verify this, the theoretical values of the plane-strain moduli of these samples were calculated based on the experimental orientation distribution functions (see Fig. 4.2) using the single-crystal elastic constants of Cu [126]. The detailed analysis is given in Appendix C and the results are presented in Fig. 4.6 together with the experimental data. For comparison, the theoretical plane-strain moduli of films with pure $\langle 111 \rangle$ - and $\langle 100 \rangle$ -fiber textures, which constitute the theoretical upper and lower bounds for the plane-strain modulus, are also shown in Fig. 4.6.

For the as-deposited films, agreement between experimental and calculated values is quite remarkable. After annealing, the plane-strain modulus decreases slightly. This

decrease cannot be attributed to the crystallographic texture since the texture of these films remains almost unchanged after annealing. One possible explanation for the reduced modulus is the severe grain boundary grooving observed after annealing [Fig. 4.4]. The effect of grain boundary grooving on the stiffness measurement can be estimated by modeling the grooves as a periodic array of cracks, as schematically illustrated in Fig. 4.8. The details of this analysis are given in Appendix D. Figure 4.9 presents the effective stiffness as a function of the normalized grain boundary groove depth and density. From the figure, it is evident that the reduction in film stiffness due to grain boundary grooving is at most 1 – 2%, too small to explain the decrease in stiffness upon annealing. A more likely explanation may be found in enhanced anelastic behavior of the annealed films. This explanation is indeed supported by experimental results obtained by Kalkman and colleagues [96], who used a dynamic bulge test technique to demonstrate that the stiffness of freestanding Cu films is frequency-dependent. They attributed this observation to anelastic stress relaxation resulting from grain boundary

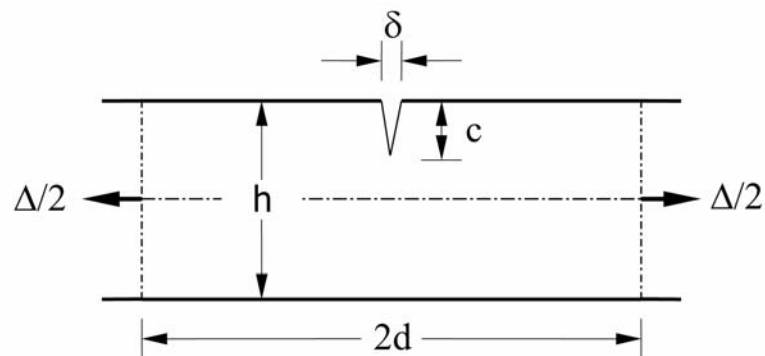


Figure 4.8: Periodic crack model for grain boundary grooves.

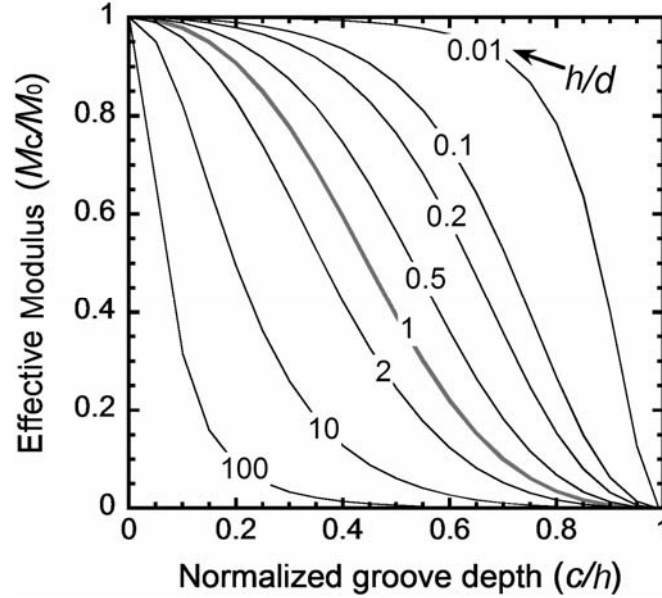


Figure 4.9: The normalized effective plane-strain modulus, M_c / M_0 , as a function of the normalized depth, c/h , and density, h/d , of the grain boundary grooves.

sliding. Dislocation bowing is a more likely mechanism in the present case, because the annealed films have larger grains than the as-deposited films and they have high dislocation densities [Figs. 4.3(c) and 4.3(d)].

In our experiments, no modulus deficit was observed. This is consistent with measurements by Espinosa *et al.* [58] on freestanding, sputter-deposited Cu film using a membrane deflection technique. Spaepen and colleagues [56, 60] reported an approximately 20% reduction in modulus for electron-beam evaporated Cu films using a micro-tensile test. They attributed this reduction to incomplete cohesion of the grain boundaries during the vapor deposition process. Read *et al.* [97] reported an even higher

(30 – 50%) modulus deficit in electroplated Cu films. In this case, the reduced stiffness was attributed to film porosity and plating defects. Based on these studies, it seems that the modulus deficit is more related to the film deposition technique and the ensuing microstructure rather than an intrinsic thin-film effect.

4.4.2 Stress–strain curves and residual stresses

Before annealing, the stress–strain curves exhibit a gradual transition from elastic to plastic deformation. This gradual transition can be attributed to variations in the residual stress between grains. It is indeed well known from micro-diffraction experiments that the residual stress state can differ significantly from grain to grain [127]. Moreover, as-deposited films have a heterogeneous microstructure with large grains next to areas of smaller grains and thus higher yield stress. Consequently, different grains yield at different overall stress levels producing a rounded stress–strain curve. Thicker films have a wider grain size distribution making the transition more gradual for these films.

Annealed films, by contrast, have a sharp elastic-plastic transition. This is explained as follows. After a Cu film is annealed at 600 °C for one hour, the stress in the film is more or less fully relaxed due to diffusional processes. When the film is cooled to room temperature, a tensile stress develops in all grains due to the thermal mismatch between film and substrate. Considering the magnitude of the thermal mismatch strain, full plastic flow is expected in all grains. Thus, immediately after cooling, all grains are roughly at their yield stress. This stress is relaxed somewhat during the wet etch process

as is evident from the stress–strain curves in Fig. 4.5. Consequently, all grains are expected to yield at almost the same macroscopic strain with some variation from grain to grain resulting from the stress relaxation and the elastic anisotropy of the grains. Macroscopically, this results in a sharp transition of the stress–strain curve from the elastic regime to the plastic regime. It should be noted that the elastic–plastic transition also depends on the crystallographic texture of the films since some grains are oriented more favorably for plastic deformation than others. The effect of texture is very small in this case, however, because both as-deposited films and annealed films of a given thickness have similar textures (see ODFs in Fig. 4.2) and yet sharply different transitions. This indicates that the gradual transition for the as-deposited films can be attributed mainly to grain-to-grain variations in the residual stress and to the heterogeneity of the microstructure.

4.4.3 Yield stress

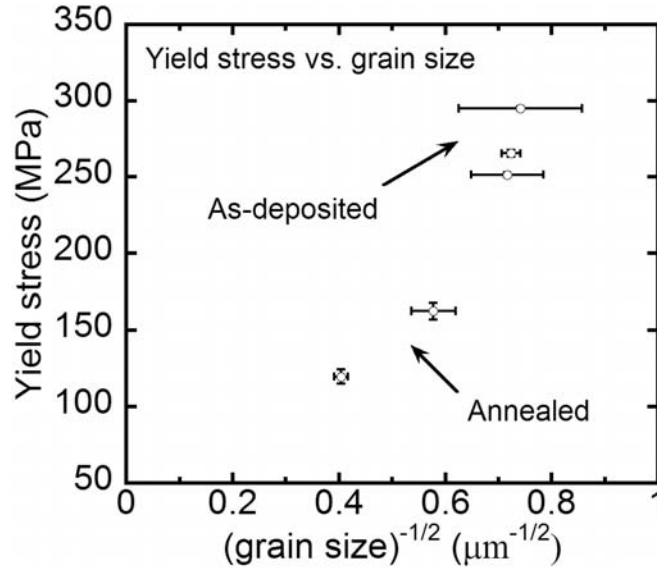
Figure 4.7(a) shows the yield stress of the Cu films as a function of film thickness. The figure clearly illustrates that the film thickness is not the main parameter determining the yield stress of the films. Potential strengthening mechanisms in these Cu films include grain boundary strengthening, Taylor hardening, the film thickness effect, the effect of crystallographic texture, and possibly solid solution hardening by impurities that were introduced in the films during the electroplating process. Strengthening due to the film thickness effect can be ruled out in the present study, because the films in this study are freestanding and Cu does not form a strong passivating oxide layer. In fact, one might

even expect a slight weakening of a freestanding film when the film thickness is on the order of the grain size due to a reduction in constraint experienced by each grain. Strengthening due to dislocation interactions is also unlikely to be a significant factor, because the increase in flow stress due to work hardening in Fig. 4.5 is small compared to the reduction in yield stress after annealing. Moreover, the annealed films have a relatively high dislocation density. Finally, it is likely that electroplated Cu films have small amount of impurities from the electroplating process, but the concentration of impurities and the resulting solid solution strengthening should be independent of film thickness or heat treatment. Thus, crystallographic texture and grain size are the main candidates to explain the observed behavior. These strengthening mechanisms will now be examined in more detail.

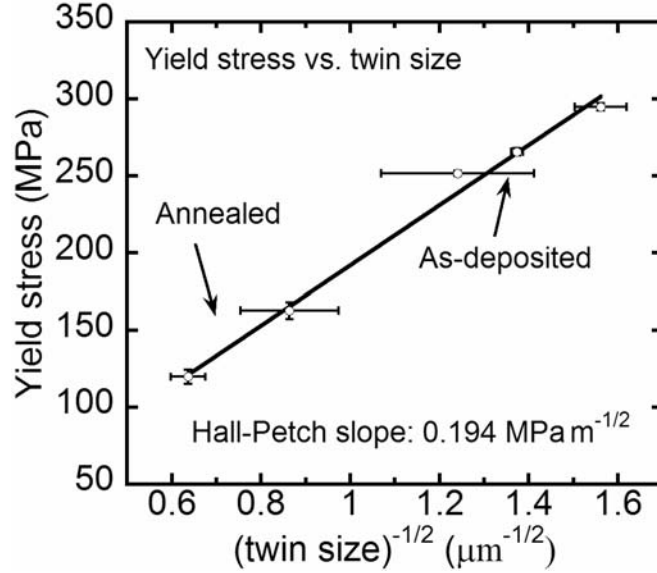
The yield stress of polycrystalline films depends on the texture of the films because grains with different orientations yield at different levels of stress. In order to quantify this effect, the plane-strain Taylor factor was calculated from the experimental ODFs for each of the films. Details of the calculation can be found in Appendix E. Figure 4.7(b) shows the Taylor factor and the corresponding resolved shear stress as a function of film thickness. The Taylor factor decreases slightly with increasing film thickness and after annealing, but the effect is not nearly strong enough to explain the experimental observations: the resolved shear stress varies both with film thickness and with heat treatment.

We now consider the effect of grain boundary strengthening. Figure 4.10(a) shows the plane-strain yield stress of the films in a traditional Hall-Petch plot. The

correlation with the square root of the grain size is poor with different slopes for annealed and as-deposited films. In Fig. 4.10(b), the yield stress is plotted as a function of the modified average grain size counting twin boundaries as distinct grain boundaries. The yield stress clearly shows Hall-Petch behavior, indicating that twin boundaries act as barriers to dislocation motion. Dislocations with Burgers vectors along the intersection of the slip planes in the twinned and untwinned sections of the grain can of course propagate across the twin boundary. Transmission of dislocations with other Burgers vectors, however, requires these dislocations to first dissociate into a non-glissile Frank partial dislocation that is left at the twin boundary and a Shockley partial dislocation that can propagate through the boundary. The dissociation process is energetically unfavorable and requires an elevated stress level before it occurs [65]. This mechanism is confirmed by a TEM study of bulk electroplated Cu samples with very high twin densities [35] and by in-situ TEM observations of the deformation process in nanocrystalline Cu specimens [128]. Thus, twin boundaries can be treated as obstacles to dislocation motion and our results suggest that the relevant length scale in the Hall-Petch relationship is the modified average grain size where twins are counted as separate grains. It should be noted that the difference between the two measures for grain size, and hence the difference between Figs. 4.10(a) and (b), is a direct consequence of the high incidence of twinning in these films and may not be so obvious for films with fewer twins. The data in Fig. 4.10(b) suggest a Hall-Petch coefficient of $0.194 \pm 0.011 \text{ MNm}^{-3/2}$. However, in order to make a valid comparison with the bulk Hall-Petch coefficient for Cu, the results in Fig. 4.10(b) first need to be converted to the equivalent uniaxial yield stress using the procedure given



(a)



(b)

Figure 4.10: The plane-strain yield stress as a function of average grain size ignoring twin boundaries (a) and taking twin boundaries into account (b).

in Appendix B. The resulting Hall-Petch slope is $0.156 \pm 0.008 \text{ MNm}^{-3/2}$, which is in good agreement with the value of $0.112 \text{ MNm}^{-3/2}$ observed in tensile testing of bulk Cu [129]. It should be noted that the grain sizes used to determine the Hall-Petch coefficient for these samples are slightly larger than for equivalent bulk samples with more equiaxed grains because of the large aspect ratios of twins. Properly correcting for the aspect ratios of the twins further lowers the Hall-Petch coefficient to the bulk value.

Keller *et al.* [103] obtained a Hall-Petch coefficient roughly three times larger than that of bulk Cu by testing sputter-deposited Cu films on Si substrates using the substrate curvature technique. Interpretation of substrate curvature measurements is of course complicated by the fact that both temperature and strain are changed simultaneously during the measurement. Furthermore, it is difficult to separate the effects of grain size and film thickness for films on substrates. This clearly illustrates the importance of making measurements on freestanding films.

4.5 Summary

In this chapter, the plane-strain bulge test technique was used to investigate the mechanical behavior of freestanding electroplated Cu thin films with an eye on the effects of film thickness and microstructure. A small variation of stiffness with Cu thickness is observed. This variation is the result of the elastic anisotropy of Cu and the changes in the crystallographic texture of the films. The Cu films do not show a modulus deficit and experimental moduli agree well with results obtained from single-crystal

elastic constants and the appropriate orientation distribution functions. Variations of yield stress with film thickness and heat treatment can be directly attributed to corresponding changes in the grain size of the films. The measurements indicate that twin boundaries act as obstacles to dislocation motion and the yield stress follows typical Hall-Petch behavior if twins are counted as distinct grains when determining the grain size. Film thickness and crystallographic texture have a negligible effect on strengthening of freestanding Cu thin films.

Chapter 5

Length-scale effect in freestanding Cu thin films[†]

In the previous chapter, we have recognized the influence of the microstructure on the elastic-plastic properties of freestanding electroplated Cu thin films. In the next two chapters, we will systematically investigate the dimensional constraint effects on the plastic behavior of freestanding thin Cu films that are associated with the presence of film-passivation interfaces and the small film thickness. This chapter focuses on the effects of surface passivation and film thickness on the yield stress and strain-hardening behavior of freestanding Cu thin films with a range of thicknesses and surface passivation conditions, while the next chapter discusses the influence of surface passivation and film

[†] Based on "*The effects of passivation layer and film thickness on the mechanical behavior of freestanding electroplated Cu thin films with constant microstructure*", Y. Xiang, J.J. Vlassak, M.T. Perez-Prado, T.Y. Tsui, A.J. McKerrow, in Mater. Res. Soc. Sym. Proc. **795**, 417-422 (2005) and "*Size effect and Bauschinger effect in freestanding thin films*", Y. Xiang and J.J. Vlassak, Acta Mater., in review (2005).

thickness on the reverse plastic behavior on unloading, i.e., the Bauschinger effect.

5.1 Objective and overview

The effect of dimensional constraints on the mechanical behavior of thin films is often referred to as the film thickness effect, size effect, or length-scale effect. The length-scale effect is a more accurate terminology compared with the other two because the constraint effect is significant only when the characteristic length scales of the deformation field approach one or more materials length parameters of the films.

The objective of the work presented in this chapter is to develop a basic understanding of the physical origins of the length-scale effect. Several sets of Cu films with thickness ranging from 0.34 – 4.2 μm are prepared using either electroplating or sputtering. In order to rule out the influence of microstructure, the microstructure of the films is controlled such that it is either independent of film thickness or only a weak function of film thickness for each set of samples. The stress–strain curves are obtained using the plane-strain bulge test technique. The effects of surface passivation, film thickness, and grain size on the yield stress and strain-hardening of these films are quantitatively evaluated. The experimental results are then compared with calculations based on both the strain-gradient plasticity theory and discrete dislocation dynamics [88]. Comparison of modeling results with experimental data provides insight in the mechanisms controlling plasticity in these films and yield numerical values for the length scale in the strain-gradient plasticity.

5.2 Experiments

The stress–strain curves of three sets of freestanding Cu films [Table 5.1] were obtained using the plane-strain bulge test technique [59, 65].

The first set of samples consisted of electroplated Cu films with thickness varying from 1.0 to 4.2 μm , but with constant microstructure [Table 5.1]. These films were fabricated by electroplating 5.4 μm Cu films on Si substrates using a commercial plating process [99]. Prior to the plating process, the Si substrates were coated with a 80 nm Si_3N_4 film using low-pressure chemical vapor deposition, a 20 nm TaN adhesion layer using reactive sputtering, and a Cu seed layer using magnetron sputtering. The electroplated films were annealed at 400°C for 15 minutes in vacuum to obtain a uniform and stable microstructure. The films were subsequently thinned to the desired thickness by means of chemical mechanical planarization (CMP). Further details of the materials preparation process can be found in [99]. Freestanding Cu membranes were fabricated by opening long rectangular windows in the substrate using Si micromachining techniques [65] and by etching the exposed Si_3N_4 and TaN coatings using a CF_4 reactive plasma. Some of the membranes were passivated by sputter coating 20 nm Ti onto either one surface or both surfaces of the freestanding Cu membranes. For these films, the effect of microstructure on the mechanical properties is completely ruled out; comparison of the stress–strain curves for these films reveals the effects of passivation and film thickness.

The second set of samples consisted of electroplated Cu films of a single thickness (1.8 μm) but different Ti passivation thicknesses. The sample preparation

Table 5.1: Summary of experimental results.

Film set	Thickness h (μm)	Average grain size ^{a)} d (μm)	h/d	Passivation ^{b)}	Yield stress ^{c)} σ_y (MPa)
1 st set Electroplated	4.20 ± 0.05	1.50 ± 0.05	2.80 ± 0.13	20 nm Ti	181.8 ± 3.5
				no	175.5 ± 3.7
	1.90 ± 0.05	1.51 ± 0.04	1.26 ± 0.07	20 nm Ti	212.6 ± 4.5
				no	200.2 ± 4.1
	1.00 ± 0.05	1.50 ± 0.05	0.67 ± 0.04	20 nm Ti	250.8 ± 5.4
				no	200.5 ± 4.2
2 nd set Electroplated	1.75 ± 0.05	N/A	N/A	no	302.3 ± 3.0
				20 nm Ti	328.1 ± 3.3
				30 nm Ti	355.1 ± 3.2
				40 nm Ti	349.7 ± 3.6
				50 nm Ti	333.4 ± 3.5
3 rd set Sputtered	0.89 ± 0.01	0.46 ± 0.02	1.93 ± 0.11	yes	335.5 ± 16.8
				no	250.3 ± 12.5
	0.67 ± 0.01	0.46 ± 0.01	1.43 ± 0.05	yes	373.6 ± 16.7
				no	266.1 ± 13.3
	0.61 ± 0.01	0.54 ± 0.02	1.14 ± 0.06	yes	434.6 ± 21.7
				no	299.7 ± 15.0
	0.44 ± 0.01	0.39 ± 0.01	1.13 ± 0.05	yes	611.7 ± 30.6
				no	346.6 ± 17.3
	0.34 ± 0.01	0.33 ± 0.01	1.06 ± 0.06	yes	695.5 ± 34.8
				no	365.6 ± 18.3

^{a)} The average grain size was determined by the intercept method with twins counted as separate grains.

^{b)} The passivation is 20 – 50 nm (as specified in the Table) Ti on both surfaces for electroplated films and 20 nm TaN/80 nm Si₃N₄ on one surface for sputtered films.

^{c)} The yield stress is defined at 0.35% plastic strain for 2nd set of samples and at 0.2% plastic strain for all other films.

method is same as that for the first set of films except that the thickness of the as-plated Cu films was 1.8 μm and no CMP process was needed. The freestanding Cu membranes were passivated by sputtering 20 – 50 nm Ti on both surfaces of the membranes. This set of samples is useful to investigate the influence of varying surface constraints on material strengthening.

The third set of samples consisted of sputter-deposited Cu films with thicknesses ranging from 0.34 to 0.89 μm . For each thickness, Cu was sputtered directly onto freestanding bilayer membranes that consisted of 80 nm of Si_3N_4 and 20 nm of TaN. Immediately prior to the Cu deposition, the TaN surface of the membranes was sputter-cleaned in-situ using an Ar plasma. After deposition, all membranes were annealed in vacuum to increase the grain size of the films. Annealing temperatures were selected to ensure that the membranes would not buckle during the annealing step as a consequence of the differential thermal expansion between the membrane and the Si frame. The resulting grain sizes were measured using transmission electron microscopy and are listed in Table 5.1. For some samples, the $\text{Si}_3\text{N}_4/\text{TaN}$ layer was etched away using reactive ion etching (RIE) in order to create freestanding Cu membranes. Other samples were tested as annealed without removing the $\text{Si}_3\text{N}_4/\text{TaN}$ layer.

The reason for leaving the thin $\text{Si}_3\text{N}_4/\text{TaN}$ layer in place was twofold: First, the $\text{Si}_3\text{N}_4/\text{TaN}$ layer served to passivate one of the surfaces of the Cu film by blocking dislocations from exiting the film. Comparison of the stress–strain curves of these films with those of the freestanding Cu films provides information on the effect of a free surface or interface on the mechanical behavior of thin films. The second reason for

leaving the Si_3N_4/TaN layer in place was that this layer makes it possible to alternate the direction of plastic flow in the Cu film during a bulge test experiment as described in detail in the next chapter. The contribution of the TaN/Si_3N_4 coating to the stress–strain curve is readily determined by bulge testing the membrane after the Cu film has been dissolved in dilute nitric acid.

From the third set of experiments, both the length-scale and the Bauschinger effects are quantitatively evaluated. The length-scale effect results are compared with the other two sets of sample, while the Bauschinger effect results will be discussed in detail in the next chapter.

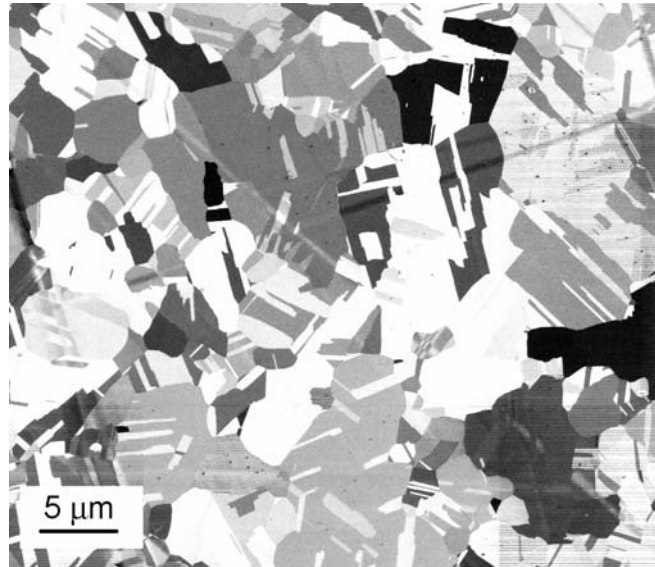
5.3 Experimental results

5.3.1 Microstructure

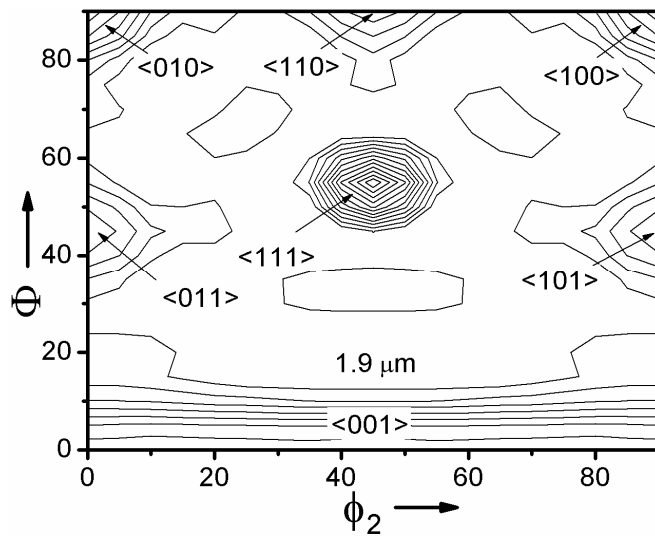
The grain structure of the first set of samples was characterized using both focused ion beam (FIB) microscopy and cross-section transmission electron microscopy (TEM). The electroplated Cu films have high incidence of twins, e.g., Fig. 5.1(a). Since twin boundaries are effective internal obstacles to dislocation motions [35, 130], the average grain size in the plane of the film was determined by the intercept method with twins counted as separate grains. As listed in Table 5.1, the average grain size of these films is 1.5 μm independent of film thickness. By contrast, if regular grains are counted,

the average grain size of the films varies from 2.5 to 3.0 μm . Furthermore, X-ray diffraction (XRD) shows that the crystallographic texture of the films is also independent of thickness. A typical orientation distribution function is shown in Fig. 5.1(b). The texture is formed with distinct $\langle 111 \rangle$, $\langle 110 \rangle$, and $\langle 100 \rangle$ fiber components as well as a randomly oriented component. Cross-section TEM [Fig. 5.2] reveals that the thinnest electroplated films have a grain size on the order of the film thickness with grain boundaries traversing the entire film [Fig. 5.2(a)]; thick films typically have more than one grain through the thickness [Fig. 5.2(b)]. This is not surprising given that the average grain size of the electroplated films is approximately one third the thickness of the thickest film. The grain size of the second set of electroplated Cu films was also determined from FIB micrographs and is listed in Table 5.1. Figure 5.2(c) presents a TEM micrograph of an electroplated film with a Ti passivation layer that was deformed in the plane of the film. A 50 nm region of high dislocation density can be observed near the Cu/Ti interface, indicating that this interface prevents dislocations from exiting the film, which has important consequences for the plastic response of the film.

The grain structure of the sputter-deposited films was characterized using TEM. Figure 5.3 shows typical plan-view TEM micrographs for the thinnest (0.34 μm) and the thickest (0.89 μm) films. These films have a columnar grain structure with equi-axed grains in the plane of the film. The grain size of the sputtered films is found to be a weak function of film thickness [See Table 5.1]. The crystallographic texture may also vary slightly with film thickness, but the results in the previous chapter show that texture has a limited effect on the yield stress of the films [130].



(a)



(b)

Figure 5.1: The FIB micrograph (a) and the orientation distribution function (b) for an electroplated 1.9 μm Cu film.

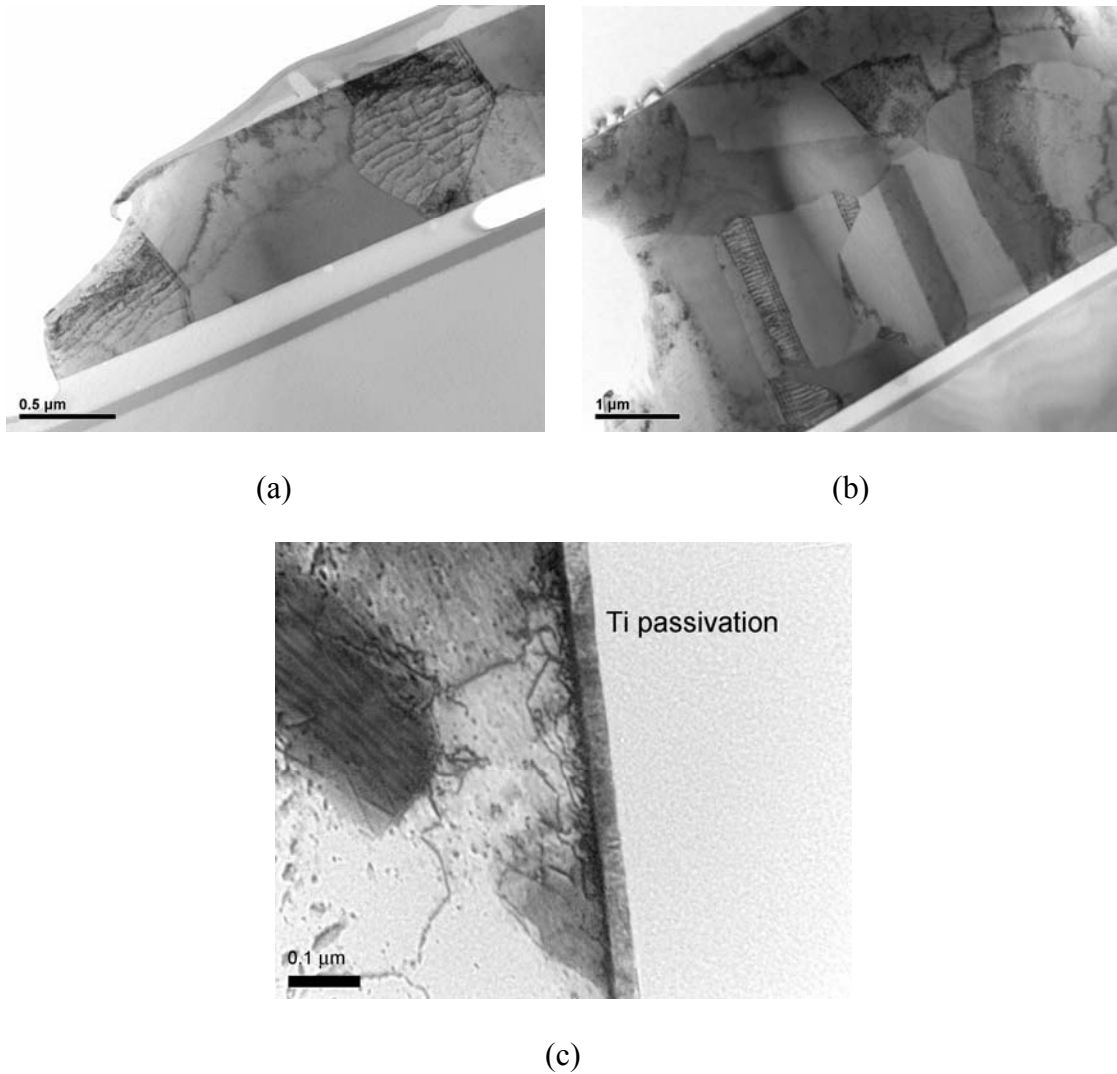
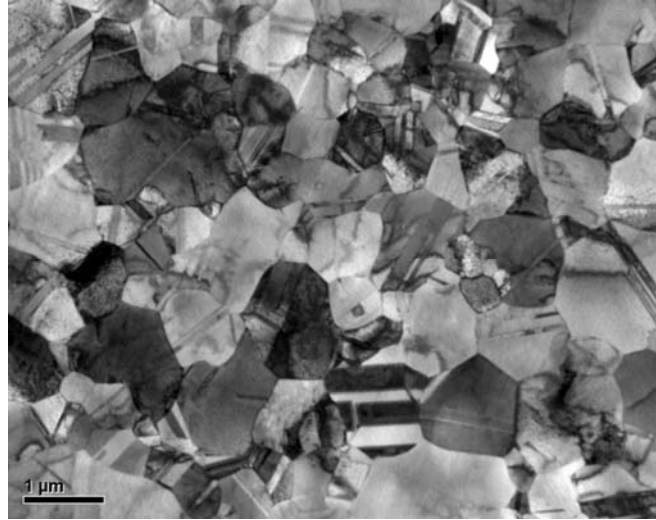
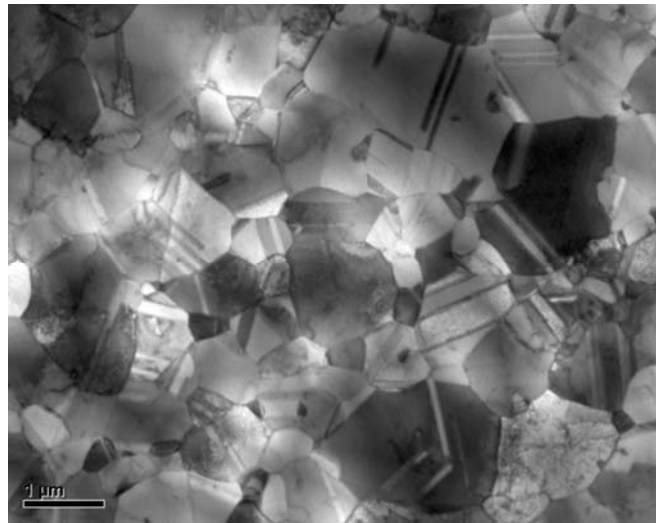


Figure 5.2: Cross-section TEM micrographs of electroplated Cu films after deformation showing: (a) Grain size on the order of the film thickness for a 1.0 μm film; (b) More than one grain across the film thickness for a 4.2 μm film; (c) A region of high dislocation density at the Cu-Ti interface in a 1.8 μm passivated film.



(a)



(b)

Figure 5.3: Typical plan-view TEM micrographs showing the grain structure for Cu films of 0.34 (a) and 0.89 (b) μm .

5.3.2 Stress–strain curves

Typical stress–strain curves for the first set of electroplated Cu films are presented in Fig. 5.4. Figure 5.4(a) shows the effect of the Ti passivation layer on the stress–strain curve of a 1.0 μm Cu film, while Figure 5.4(b) illustrates the effect of film thickness for films with both surfaces passivated by 20 nm Ti. For a given film thickness, the passivation layer clearly increases the work hardening rate of the film. Furthermore, the stress–strain curves of passivated films show a strong dependence on film thickness, even when the microstructure of the films is unchanged. This needs to be contrasted with the behavior of unpassivated films, which shows little or no variation with films thickness (See Table 5.1).

Figure 5.5 presents the stress–strain curves for the second set of electroplated Cu films. The thickness of the Ti passivating layer varies from 20 – 50 nm. It is evident that the presence of passivation layer increases the hardening rate and flow stress of the film distinctly, no matter what the thickness is. With the increasing Ti thickness, the flow stress and hardening rate of the film first increases and reaches a maximum at $h_{\text{Ti}} = 30$ nm.

Figure 5.6 shows typical stress–strain curves for sputter-deposited films [Figs. 5.6(a) – (e) for 0.34 – 0.89 μm films, respectively]. It should be noted that all figures are plotted with the same scale. For each thickness, the curves for films both with and without $\text{TaN/Si}_3\text{N}_4$ passivation are shown. For all thicknesses, films with passivation show significantly more work hardening than unpassivated films. Moreover, films with passivation are deformed in compression at the end of the last few unloading cycles except for the thinnest one [Fig. 5.6(a)]. All unloading/reloading cycles for these

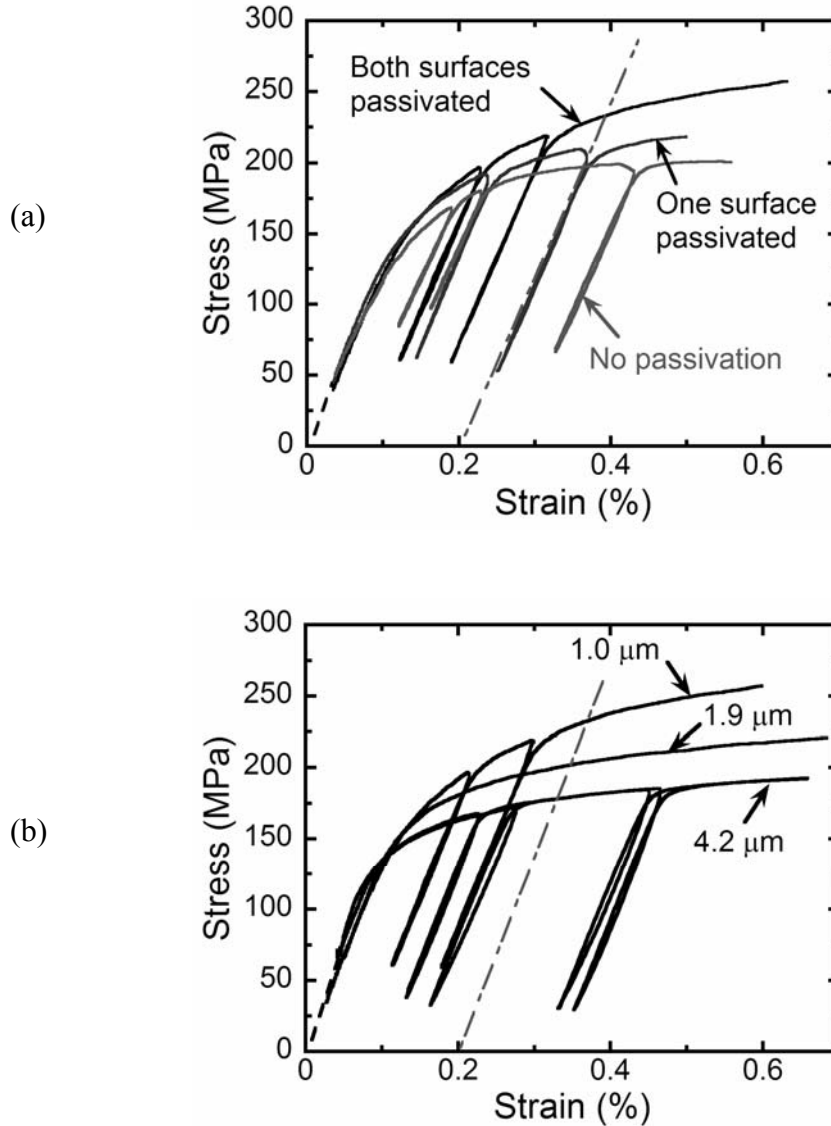


Figure 5.4: Stress–strain curves of the first set of electroplated Cu films. (a) The effect of passivation for 1.0 μm films. (b) The effect of film thickness for 1.0 – 4.2 μm films with both surfaces passivated by 20 nm Ti. All curves are offset by the equi-biaxial residual strains in the films, as represented by the dashed line starting from the origin.

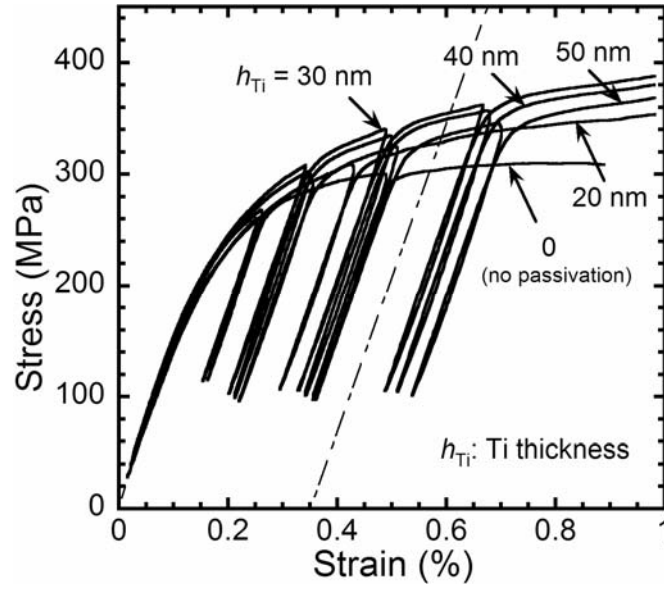
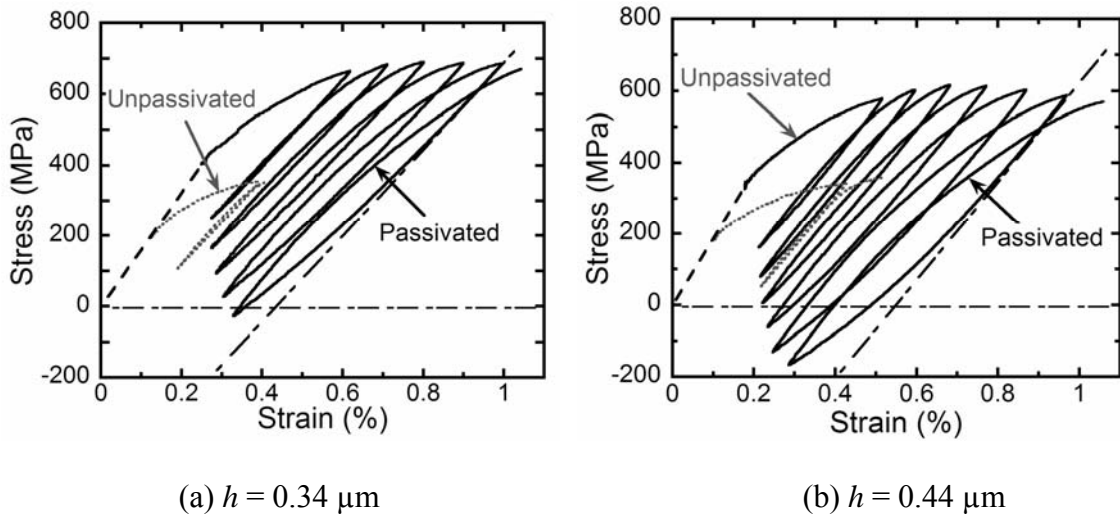


Figure 5.5: The stress–strain curves of 1.8 μm electroplated Cu films (2nd set) with both surfaces passivated by 20 – 50 nm Ti. All curves are offset by the equi-biaxial residual strains in the films, as represented by the dashed line starting from the origin.



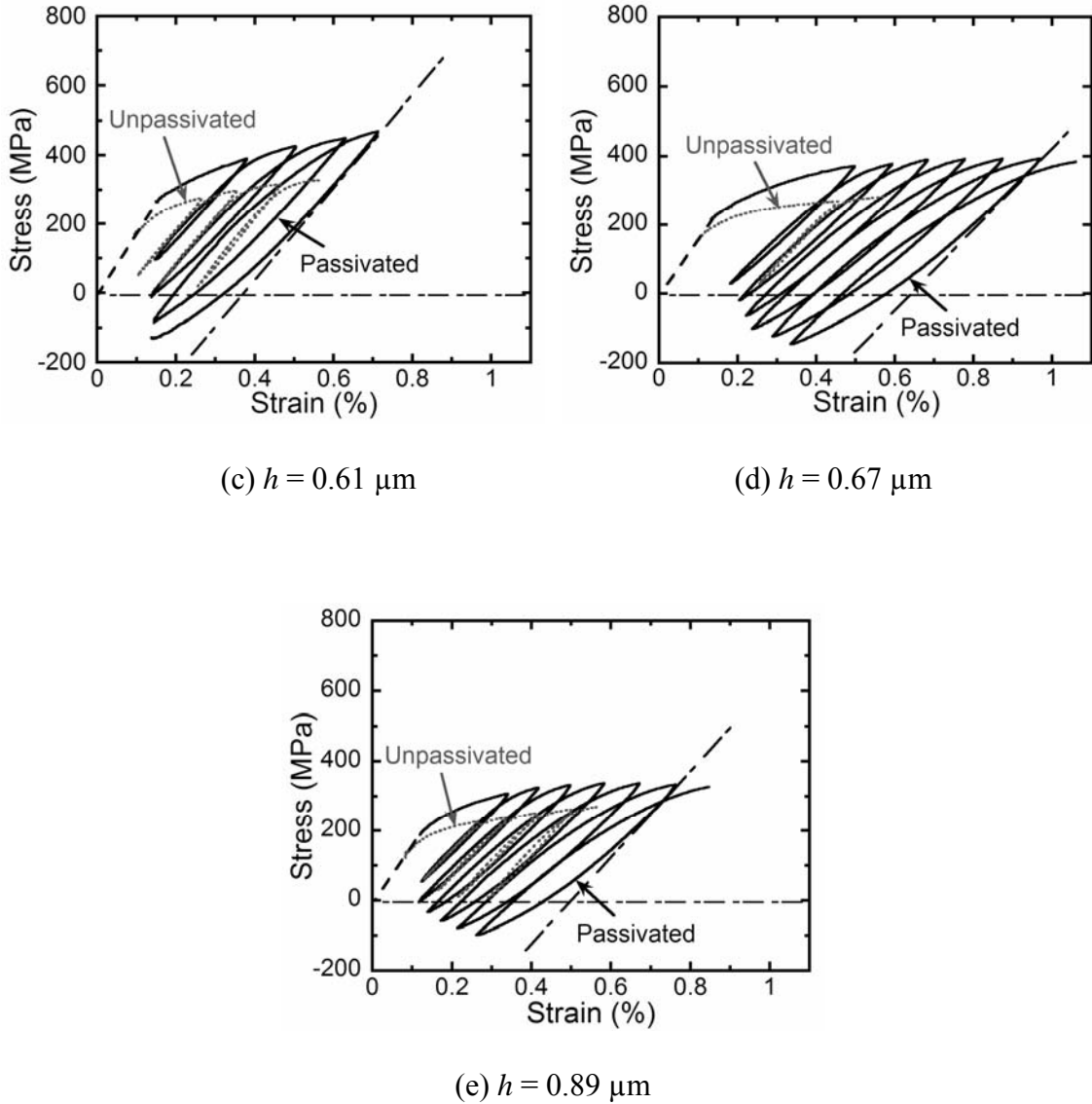


Figure 5.6: Typical stress–strain curves for unpassivated (dotted curves) and passivated (solid curves) Cu films: [(a) – (e)] for $0.34 - 0.89 \mu\text{m}$ films, respectively. All curves are plotted at the same scale and are offset by the equi-biaxial residual strains in the films, as represented by the dashed line starting from the origin.

passivated film show significant hysteresis with reverse plastic flow occurring even when the overall stress in the film is still tensile. By contrast, films without passivation show little or no reverse plastic deformation when fully unloaded. In other words, passivated films show a strong Bauschinger effect, while unpassivated films do not.

5.3.3 Yield stress

Table 5.1 lists the yield stress for all films tested. Figure 5.7 presents the yield stress as a function of reciprocal film thickness for both passivated (filled symbols) and unpassivated (open symbols) films. The yield stress is defined at 0.2% offset strain. The vertical dash-dot line separates the data of the first set of electroplated Cu films and that of the sputter-deposited Cu films. It is noticed that for films with thickness below 1 μm , the yield stress of passivated films rises much more rapidly than for the thicker films, even though the latter have passivation on both sides. There are two possible explanations. It is possible that the Ti coating does not provide as strong a barrier to dislocation motion as the TaN/Si_3N_4 layer, since the latter is stiffer and does not deform plastically. Alternately, it is possible that the effect of the passivation layer indeed increases rapidly with decreasing film thickness independent of the precise nature of the passivating layer. Both explanations will be explained in more detail later in this chapter. There is a slight dependence on film thickness for sputter-deposited films without passivation. This is the result of Hall-Petch hardening, since the grain size of these films decreases with decreasing film thickness [Table 5.1]. By contrast, for electroplated films without passivation, the yield stress shows little or no variation with film thickness, since the

grain size of these films is a constant [Table 5.1]. This can be better appreciated by plotting the yield stress of unpassivated films as a function of the reciprocal square root of the average grain size in Fig. 5.8. Also plotted are the data (open circles in Fig. 5.8) for freestanding electroplated Cu films in Chapter 4 and a linear fit (the solid line in Fig. 5.8) of the Hall-Petch relationship to the current set of data. The Hall-Petch slope is $0.19 \text{ MPam}^{-3/2}$, which is identical to the value obtained in Chapter 4. It is evident that the three sets of experimental results agree remarkably well with each other independent of film deposition methods. This agreement also suggests that impurities in both sets of electroplated Cu films do not affect the yield stress significantly.

Figure 5.9 presents the yield stress as a function of the thickness of Ti passivation coatings for the $1.8 \text{ }\mu\text{m}$ Cu films. The increase of the yield stress is significantly larger than the contribution of the Ti coatings even when assuming they deform only elastically, as represented by the dashed line in Fig. 5.9. The figure clearly shows the strengthening effect of the Ti surface passivation. This strengthening effect is consistent with the formation of boundary layers of high dislocation density nearer the Cu-Ti interfaces due to the constrained dislocation motions, as suggested by Nicola et al. [76]. The interface constraint is certainly affected by the mechanical properties and thickness of the passivation layer. Figure 5.9 shows that the yield stress increases with increasing Ti thickness and reaches a maximum at $h_{\text{Ti}} = 30 \text{ nm}$. We attribute this effect to an increasing constraint on dislocation motion at the Cu-Ti interface as the Ti thickness increases. The decrease of the yield stress above $h_{\text{Ti}} = 30 \text{ nm}$ is likely due to plastic deformation or cracking of the Ti coatings, which would relax the constraint on

dislocation motion near the Cu-Ti interface.

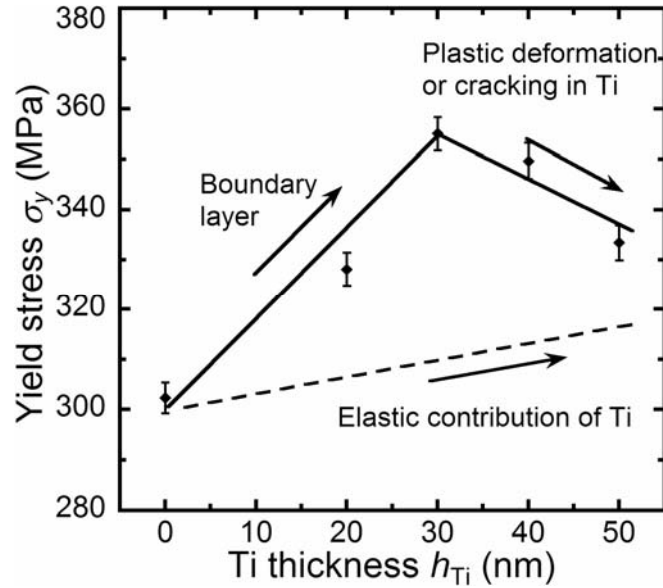


Figure 5.9: Yield stress as a function of the passivation layer thickness for 1.8 μm electroplated films. The dashed line represents the contribution of the Ti layers if there is no plastic deformation in Ti.

5.4 Strain-gradient plasticity calculations

In this section, we pursue the suitability of the strain-gradient plasticity (SGP) theories to explain of the experimental results. This is motivated by the fact that the presence of passivating layers causes constrained plastic deformation at the film-passivation interface, which naturally leads to plastic strain gradients in the passivated films.

5.4.1 The strain-gradient plasticity

One of the recognized sources of size-dependent plasticity at the micron scale is the presence of plastic strain gradients that increase the plastic flow resistance. This feature cannot be captured by classical plasticity theories. Strain-gradient plasticity theories are thus developed by introducing one or more material length parameters into the classical theories. These length parameters set the characteristic dimensions of the deformation field at which the contribution of plastic strain gradients to work hardening is comparable to that of plastic strains. The work hardening due to dislocation interactions is quantified by the empirical Taylor equation, which relates the flow stress to the total dislocation density in the material. Dislocations are typically divided into so-called statistically stored dislocations (SSDs) and geometrically necessary dislocations (GNDs). These two types of dislocations are physically indistinguishable in a crystal and contribute to the Taylor hardening in the same way, i.e., both types of dislocations are internal obstacles to gliding dislocations. Generally, only SSDs contribute to the macroscopic plastic strains in the material, while GNDs are often associated with a net Burgers vector in a given volume, which naturally leads to plastic strain gradients.

The strain-gradient plasticity theories in the literature are typically categorized in different types depending on how plastic strain gradients are incorporated into the theories. In this chapter, we choose the stretch and rotation version of the strain-gradient plasticity theory proposed by Fleck and Hutchinson [73]. The Fleck-Hutchinson theory is a generalization of classical J_2 theory in both flow and deformation versions. The dependence on the gradients of plastic strains is incorporated by introducing a

generalized effective plastic strain, which is a weighted function of the conventional effective plastic strain and three independent invariants of the plastic strain gradient tensor. Three material length parameters (ℓ_1 , ℓ_2 , and ℓ_3) enter the coefficients of the three independent invariants in the expression of the generalized effective plastic strain. These length parameters characterize the contributions of both stretch and rotation gradients of plastic strains to the plastic flow resistance. Particularly, ℓ_2 and ℓ_3 determine the contribution of rotation gradients, while ℓ_1 reflects the contribution of both stretch and rotation gradients. The essence of the Fleck-Hutchinson theory is that the generalized effective plastic strain is used as a phenomenological measure of the total dislocation density resulting from plastic strains (SSDs) and their gradients (GNDs) and that both types of dislocations increase the plastic flow resistance in the same way.

5.4.2 Problem formulation

The plastic response of a homogeneous, isotropic thin film in the bulge test configuration is analyzed using the flow version of the Fleck-Hutchinson theory [131]. Figure 5.11 schematically illustrates the cross-section of the film. The plastic flow is constrained at the bottom surface of the film due to the presence of a rigid passivation layer. We choose a Cartesian coordinate system with the origin at the film-passivation interface and with three axes along the three principal stress directions (cf. Fig. 3.1). The film is subjected to plane-strain tension with the strain rate along the longitudinal direction, $\dot{\epsilon}_{22}$, equal to zero. Moreover, since the pressure applied to the film is much

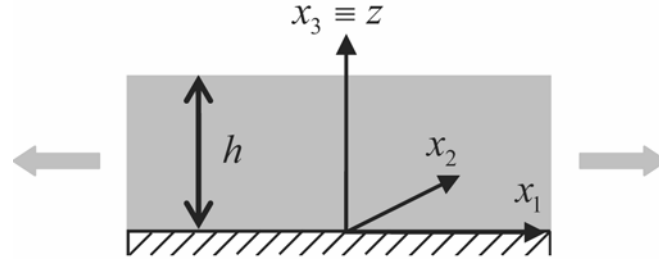


Figure 5.10: Schematic illustration of the cross-section of a thin film under plane-strain tension. The bottom surface of the film is passivated by a rigid layer.

smaller compared to the in-plane stress, the stress rate normal to the film surface, $\dot{\sigma}_{33}$, can be taken equal to zero. In order to avoid mathematical complexity, elastic strains are ignored in the following derivation. This simplification has negligible influence for calculations in the plastic regime [73]. The plastic strain rate components are functions of $x_3 \equiv z$ only and the nonzero components can be expressed in terms of the unknown conventional effective plastic strain rate, $\dot{\varepsilon}_p$,

$$\dot{\varepsilon}_{11}^p(z) = -\dot{\varepsilon}_{33}^p(z) = \frac{\sqrt{3}}{2} \dot{\varepsilon}_p(z), \quad (5.1)$$

where $\dot{\varepsilon}_p = \sqrt{2\dot{\varepsilon}_{ij}^p\dot{\varepsilon}_{ij}^p/3}$. The generalized effective plastic strain rate, \dot{E}_p , is found to be

$$\dot{E}_p^2 = \dot{\varepsilon}_p^2 + \left(\frac{1}{2} \ell_1^2 + \frac{8}{3} \ell_3^2 \right) \dot{\varepsilon}_p'^2 = \dot{\varepsilon}_p^2 + \ell^2 \dot{\varepsilon}_p'^2, \quad (5.2)$$

where $(\)' \equiv \frac{d(\)}{dz}$, ℓ_1 and ℓ_3 are the material length parameters originally defined in

[73], and $\ell = \sqrt{\frac{1}{2}\ell_1^2 + \frac{8}{3}\ell_3^2}$ is an effective length parameter that sets the scale at which the contribution of the gradients term is important to the generalized effective plastic strain rate. The second material length parameter, ℓ_2 , does not enter the expression implying that rotation gradients are not important in current problem. The stress rate components are given in terms of the conventional equivalent stress rate, $\dot{\sigma}_e$,

$$\dot{\sigma}_{11} = 2\dot{\sigma}_{22} = \frac{2}{\sqrt{3}}\dot{\sigma}_e, \dot{\sigma}_{33} = 0. \quad (5.3)$$

where $\dot{\sigma}_e = \sqrt{2\dot{s}_{ij}\dot{s}_{ij}/3}$, with \dot{s}_{ij} the stress deviator. The constitutive equation for strain-gradient plasticity is given as

$$\dot{\sigma}_e = \dot{h}(E_p)\dot{\varepsilon}_p - \ell^2 \left(\dot{h}(E_p)\dot{\varepsilon}_p' \right), \quad (5.4)$$

where $\dot{h}(E_p)$ is the tangent hardening quantity of the uniaxial tensile stress–strain curve, $d\sigma(\varepsilon_p)/d\varepsilon_p$, evaluated at the generalized effective plastic strain rate, \dot{E}_p . In the calculations, the uniaxial tensile stress–strain data of the film need to be used as input to the formulation and we take the Ramberg-Osgood curve,

$$\frac{\varepsilon}{\varepsilon_0} = \frac{\sigma}{\sigma_0} + \left(\frac{\sigma}{\sigma_0} \right)^n \quad \text{or} \quad \sigma = \sigma_0 \left(\frac{\varepsilon_p}{\varepsilon_0} \right)^{1/n}, \quad \text{with} \quad N = \frac{1}{n}, \quad (5.5)$$

where ε_0 and σ_0 are the yield strain and yield stress, respectively; $\varepsilon_0 = \sigma_0/E$ and E is Young's modulus. Thus $\dot{h}(E_p)$ is equal to $NE(E_p/\varepsilon_0)^{N-1}$. For convenience, the strain and stress rates are normalized by ε_0 and σ_0 , where corresponding variables are labeled with a hat $\hat{\cdot}$; ℓ and z are normalized by the film thickness, h , with $L = \ell/h$, $x = z/h$,

and $\frac{d(\)}{dz} = \frac{1}{h} \frac{d(\)}{dx}$. For simplicity, from now on we denote $(\)' \equiv \frac{d(\)}{dx}$. Substituting

$\dot{h}(E_p) = NE(E_p / \varepsilon_0)^{N-1}$ into Eq. (5), we find

$$\dot{\sigma}_e = N\dot{E}_p^{N-1}\dot{\varepsilon}_p - L^2 \left(N\dot{E}_p^{N-1}\dot{\varepsilon}_p'^2 \right)', \quad (5.6)$$

where $\dot{E}_p = \left(\dot{\varepsilon}_p^2 + L^2 \dot{\varepsilon}_p'^2 \right)^{1/2}$ is the normalized effective plastic strain rate from Eq. (5.2).

From Eqs. (2) and (4) and noticing that $\dot{\varepsilon}_{11}^e = \dot{\varepsilon}_{11} - \dot{\varepsilon}_{11}^p$, the effective stress rate can be related to the applied strain rate, $\dot{\varepsilon}_{11}$, and the unknown conventional effective strain rate, $\dot{\varepsilon}_p$,

$$\dot{\sigma}_e = \frac{\sqrt{3}}{2} \dot{\sigma}_{11} = \frac{\sqrt{3}}{2(1-\nu^2)} \dot{\varepsilon}_{11}^e = \frac{\sqrt{3}}{2(1-\nu^2)} \left(\dot{\varepsilon}_{11} - \dot{\varepsilon}_{11}^p \right) = \frac{\sqrt{3}}{2(1-\nu^2)} \left(\dot{\varepsilon}_{11} - \frac{\sqrt{3}}{2} \dot{\varepsilon}_p \right). \quad (5.7)$$

We denote $y_1 = \dot{\varepsilon}_p$, $y_2 = \dot{\varepsilon}_p'$ and reduce Eqs. (7) to the following dimensionless ordinary differential equations

$$y_1' = y_2; \quad y_2' = \frac{A-B}{C}, \quad (5.8)$$

where $A = \frac{1}{L^2} \left(\dot{\varepsilon}_p - \dot{\sigma}_e \dot{E}_p^{1-N} \right)$, $B = \frac{N-1}{\dot{E}_p^2} \dot{\varepsilon}_p \dot{\varepsilon}_p'^2$, and $C = \frac{N-1}{\dot{E}_p^2} \left(L^2 \dot{\varepsilon}_p'^2 + 1 \right)$. The boundary

conditions are

$$y_1|_{x=0} = \dot{\varepsilon}_p|_{x=0} = 0; \quad y_2|_{x=1} = \dot{\varepsilon}_p'|_{x=1} = 0. \quad (5.9)$$

Here the constraint on plastic flow at the film-passivation interface ($x=0$) is enforced, while at the free surface ($x=1$) there is no plastic strain gradient. This boundary value problem [Eqs. (5.8) and (5.9)] can be incrementally solved to obtain the stress-strain

curve using numerical methods, e.g., using the built-in ordinary differential function solver, *bvp4c.m*, in Matlab.

For films with both surfaces passivated, the boundary condition (5.9) needs to be modified to

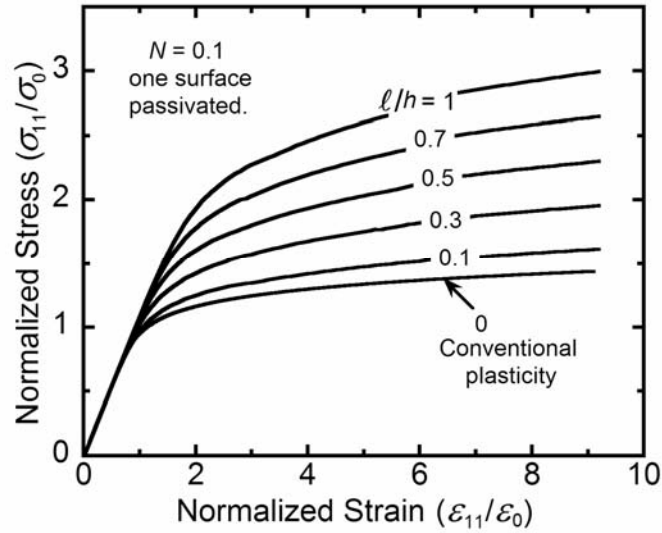
$$y_1 \Big|_{x=0} = y_1 \Big|_{x=1} = 0, \quad (5.10)$$

while all other equations remain the same.

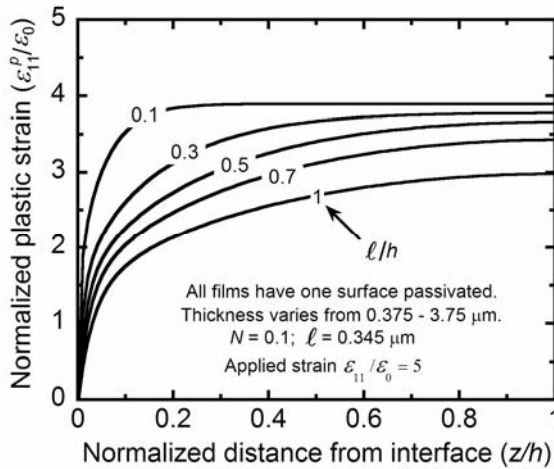
5.4.3 Numerical results

The stress–strain curves of the third set of samples are calculated using the SGP formulation in the previous section, where the hardening exponent N of unpassivated films is an input parameter. N is a constant for all thicknesses in the calculations. Since the stress–strain curves of unpassivated films can be best fitted with an N between 0.1 and 0.15, the upper and lower limits of the stress–strain curve will be calculated using the two limit values of N . Figure 5.11 (a) presents the typical results for films with $N = 0.1$ and with one surface passivated. The size effect is clearly shown in the stress–strain curves: the flow stress and hardening rate increases with decreasing normalized film thickness, ℓ/h . Figure 5.11(b) compares the distribution of plastic strains across the film thickness for these films. It should be noted the boundary condition of the film-passivation interface completely suppresses plastic flow at the interface, i.e., the plastic strain is zero at the interface.

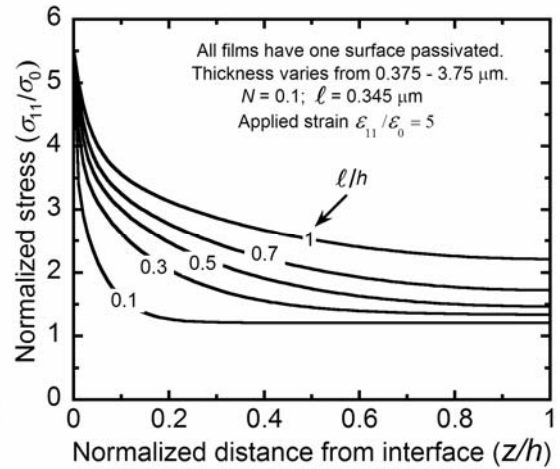
In order to compare the calculated results with the experimental data, we define a



(a)



(b)



(c)

Figure 5.11: (a) Calculated stress–strain curves for films with one surface passivated [$N = 0.1$]. (b) Distribution of transverse plastic strain and (c) distribution of transverse stress across the film thickness at a given applied strain.

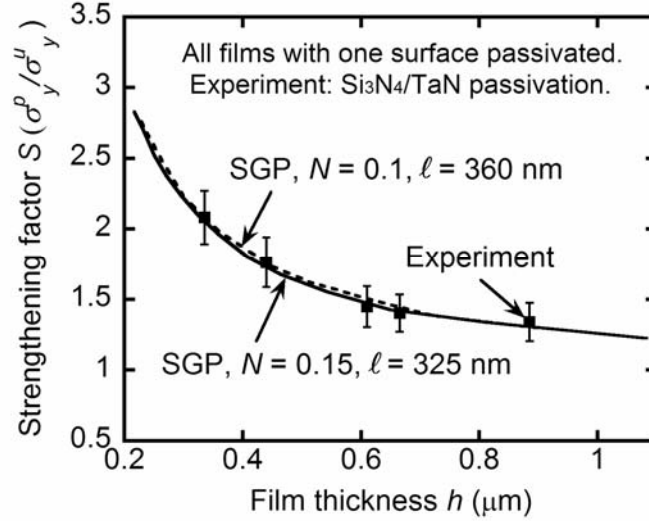


Figure 5.12: The strengthening factor, S , as defined in Eq. (2), versus the normalized film thickness. The dashed line is the best fit to experimental data with a length scale parameter $\ell = 360$ nm for a hardening index $N = 0.15$, while the solid line is the best fit with $\ell = 330$ nm for $N = 0.1$.

strengthening factor S to characterize the effect of passivation

$$S = \sigma_y^p / \sigma_y^u, \quad (12)$$

where σ_y^p and σ_y^u are the yield stress for a film with and without passivation, respectively. In other words, the yield stress of the passivated film is normalized by that of the same film without passivation and the influence of the microstructure is ruled out. The strengthening factor S is calculated from both the experimental [Figs. 5.6(a) – 5.6(e)] and the SGP [Fig. 5.11] stress–strain curves and plotted as a function of film thickness h in Fig. 5.12. By fitting the SGP results (dashed and solid curves) to the experimental data

points (filled squares), a numerical value of the material length parameter ℓ is obtained. The dashed and solid curves correspond to the two limiting cases with $N = 0.1$ and 0.15 , respectively, and yield an upper and lower limits for the material length parameter of $\ell = 360$ nm and 330 nm, respectively. The average of the two limits can be taken as the material length parameter $\ell = 0.345 \pm 0.015$ μm . The fit in Fig. 5.12 is quite good, which indicates that the SGP well describes hardening of the films.

5.5 Discrete dislocation simulations

The experiments were also directly simulated using discrete dislocation dynamics by Nicola et al. [88]. In this section, we summarize the key information of the simulation work for the purpose of comparison with our experimental results in the next section.

5.5.1 Modeling

The polycrystalline film of thickness h is modeled as an infinite array of columnar grains with an identical size d , as illustrate in Fig. 5.13. The film is subjected to plane-strain tension with zero strains along x_3 axis; therefore the model is essentially two dimensional in the x_1 - x_2 plane. Furthermore, elastic anisotropy is neglected to avoid mathematical complication. Plastic deformation in the film happens through nucleation and glide of edge dislocations in the x_1 - x_2 plane, which are treated as line singularities in an elastic solid. In each grain there are three sets of slip planes that are oriented at ϕ ,

$\phi + 60^\circ$, and $\phi + 120^\circ$ from the x_1 -axis, on which edge dislocations with Burgers vector b can nucleate and glide. Simulations are performed in a unit cell that contains eight grains (i.e., the cell length $w = 8d$) for films with one surface or both surfaces passivated, as well as unpassivated films. The orientation of each grain, ϕ , is randomly selected from the range $[0, \pi)$. Passivation layers, if any, deform only elastically and have no elastic mismatch with the film. Both grain boundaries and film-passivation interfaces are treated to be impenetrable to dislocation motions. A more complete description of the problem formulation and analysis procedure can be found in Ref. [88].

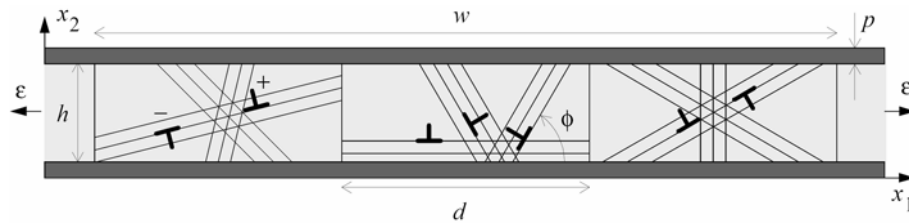


Figure 5.13: The two-dimensional model of a freestanding film with both surfaces passivated and under tensile loading. (From [88])

At the beginning of the simulations, the film is dislocation free and has random dislocation sources on the slip planes. During the simulations, dislocations nucleate when the Peach-Koehler force at a source exceeds a critical value for a given time span and glide on the slip planes under the applied stresses. Gliding dislocations form pile-ups when they reach grain boundaries and interfaces, and exit the material and leave step bands at free surfaces, interact with other dislocations resulting, e.g. annihilation. The

calculations are performed in an incremental way such that the deformation history is recorded.

The materials parameters take the representative values of Cu, while the grain size takes the average value obtained in the experiments reported earlier in this chapter. The dislocation constitutive parameters such as source density, strength, and strength distribution are determined by fitting the calculated yield stresses to the measured values for the first set of samples in passivated condition. The same dislocation constitutive parameters are then used for simulations over a much wider range film thickness and for different grain size and passivation conditions.

5.5.2 Numerical results

Figure 5.14 illustrates the snapshots of films with different passivation conditions at an applied strain of 0.5% during the simulations. The effect of surface passivation on the distribution of the stress and dislocation in the films is clearly demonstrated. It is evident that dislocations pile up not only at the film-passivation interfaces, but also at grain boundaries because both the interfaces and grain boundaries are treated as impenetrable to dislocations in the simulations. Areas near free surfaces generally contain many fewer dislocations. Passivated films show significantly higher stress levels and higher dislocation densities. There is also large variation from grain to grain in the same film as a result of orientation variation. The average stresses in these films are plotted versus the applied strains in Fig. 5.15(a), which reproduces the experimental stress–strain curves in Fig. 5.4(a). Similarly, the experimental stress–strain curves in Fig. 5.4(b) can be

simulated and the results are shown in Fig. 5.15(b), which illustrates the effect of film thickness for films with constant microstructure and with both surfaces passivated. The dislocation source density, strength, and strength distributions have been selected such that quantitative agreement is obtained between the experimental and computational results for the conditions shown in Fig. 5.15(b). The same density is used for all simulations including for the results shown in Fig. 5.15(a) and Figs. 5.16(a) and (b).

We now compare the simulations with the experimental results. The yield stress as obtained from the experiments and the discrete dislocation simulations are plotted as a function of the reciprocal film thickness for films with one surface passivated and for

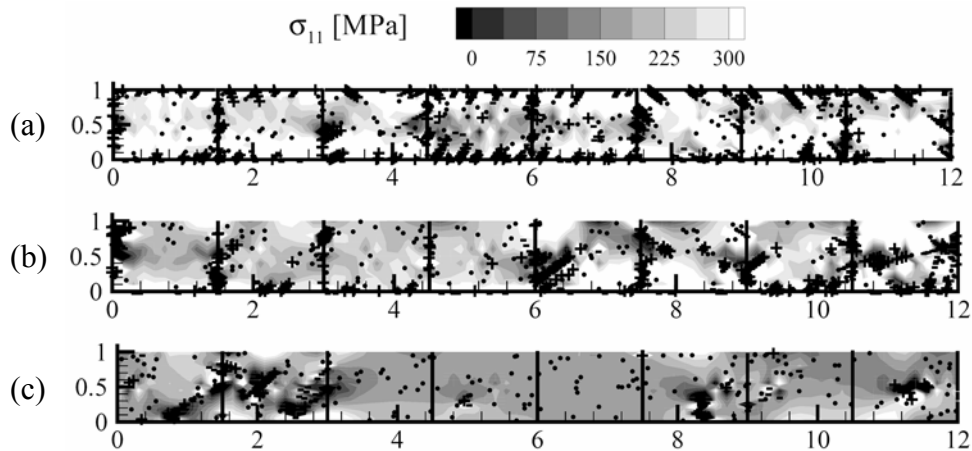


Figure 5.14: The distribution of stress and dislocation in 1 μm films with (a) both surfaces passivated, (b) bottom surface passivated, and (c) no passivation. The applied strain is $\varepsilon = 0.5\%$. (From [88])

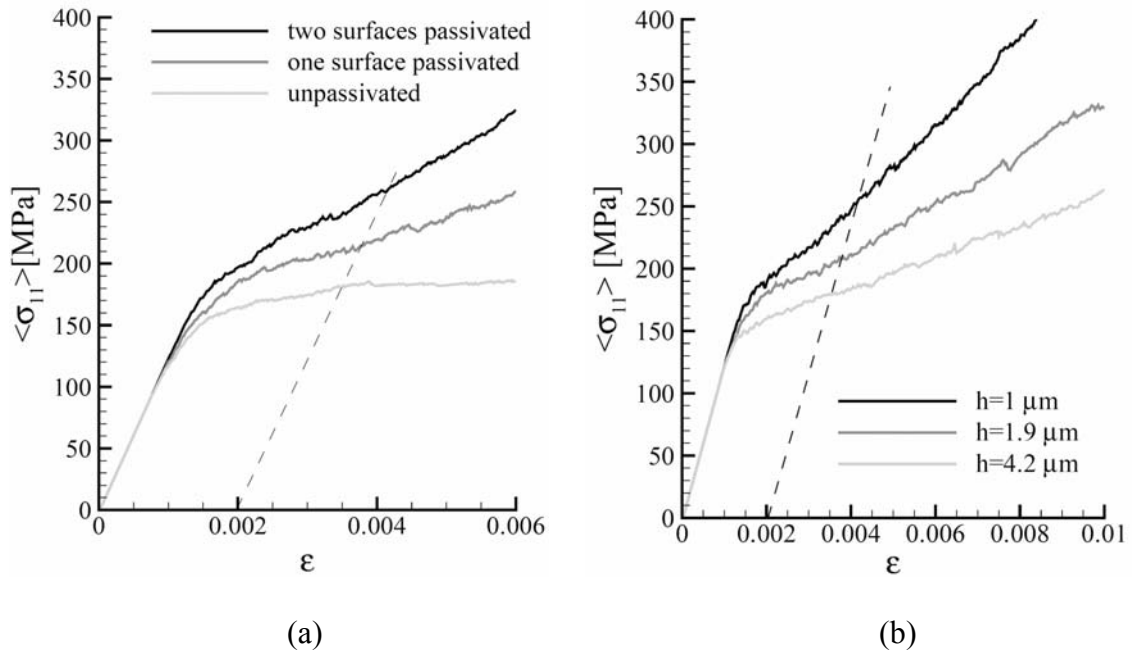


Figure 5.15: Discrete dislocation simulations reproduce the experimental stress–strain curves for the first set of Cu films [Fig. 5.4]: (a) Effects of passivation on stress–strain curves of 1.0 μm film; (b) Effects of film thickness on stress–strain curves of films with both surfaces passivated.

films without passivation in Fig. 5.16. The agreement is generally excellent although the scatter in the simulations is larger for the sputter-deposited films than for the electroplated films. This is so because the simulations are carried out with a limited number of grains while the dislocation source density is kept the same. The sputtered films have smaller grain size and thus fewer sources in each grain, which causes uncertainties in the simulations. The different slopes for electroplated and sputtered films observed in Fig. 5.16(a) and are the results of different grain sizes in the two sets of

samples. This is further confirmed by the slight change of the yield stress for unpassivated films, as shown in Fig. 5.16(b).

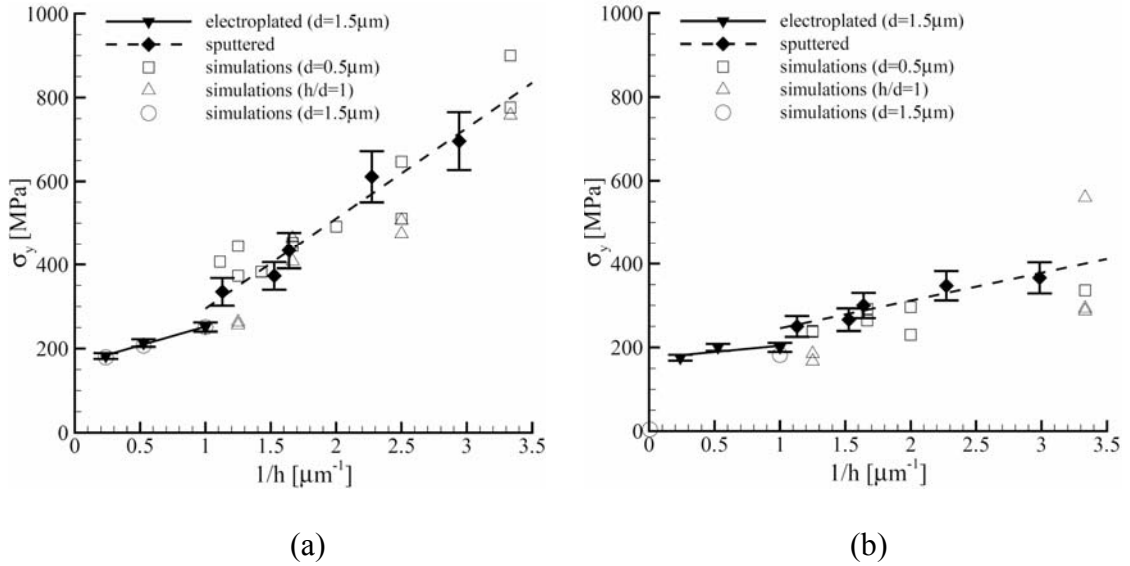


Figure 5.16: Comparison between experimental and computational yield stress as a function of the reciprocal of film thickness for (a) films with one surface passivated and (b) unpassivated films. (From [88])

5.6 Comparison and discussion

In Fig. 5.13, a material length parameter $\ell = 0.345 \pm 0.015 \mu\text{m}$ is obtained for these Cu films by comparing the yield stresses of the sputter-deposited films with the strain-gradient plasticity calculations. In both experiments and calculations, one surface

of the Cu film was passivated. In the calculation, it was assumed that plastic flows are completely suppressed at the film-passivation interface. This assumption is reasonable given that the TaN/Si₃N₄ is much stiffer than Cu, deforms only elastically, and adheres well to the Cu. If the Cu—TaN/Si₃N₄ interface does not completely suppress plastic flows, the value of ℓ should be regarded as a lower limit of the material length parameter.

It should be noticed that the effective material length parameter ℓ is different from the three material length parameters originally defined by Fleck and Hutchinson

[73]. Instead, $\ell = \sqrt{\frac{1}{2}\ell_1^2 + \frac{8}{3}\ell_3^2}$, and additional experiments are required in order to solve

for the original parameters. Nevertheless, the effective material length parameter agrees remarkably well with values obtained from other experiments [15, 73].

The physical meaning of the material length parameter ℓ can be explained as follows: If the characteristic dimension of the deformation field, or more specifically the film thickness in the current problem, is equal to ℓ , then the contribution of the plastic strain gradients to work hardening is equal to that of the plastic strains, as is evident from Eq. (3). By plotting the plastic strain gradient as a function of the distance from the interface, as shown in Fig. 5.17, we find that a boundary layer, with high gradients of plastic strains, is formed near the film-passivation interface. It is further noticed that the thickness of this boundary layer is approximately 80 nm independent of film thickness. As a result, thinner films have lower average plastic strains or higher average stresses when subjected to the same amount of applied strains. This gives the origin of the thickness-dependent plastic behavior in thin metal films. The explanation is consistent

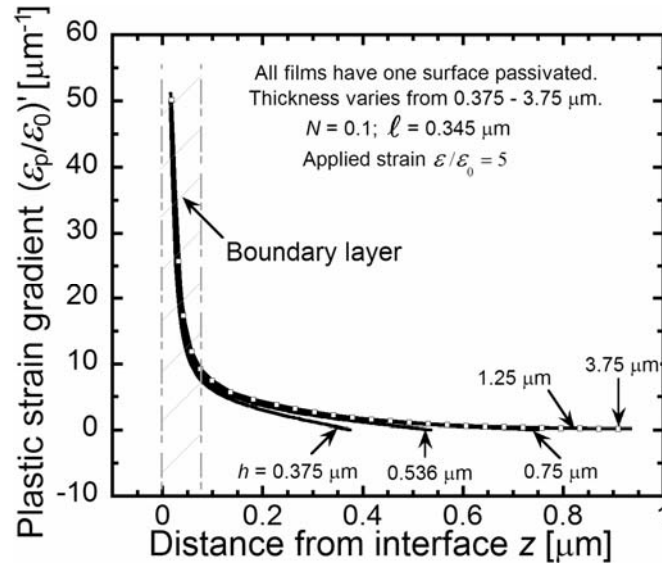


Figure 5.17: A boundary layer with high plastic strain gradients is formed near the film-passivation interface. The thickness of this layer is independent of film thickness.

with the presence of a boundary layer with high dislocation density near the film-passivation interface observed in direct discrete dislocation simulations in Ref. [76] and in Section 5.5. The distribution of dislocation in passivated films [Figs. 5.14(a) and (b)] clearly exemplifies the dislocation pile-ups near the film-passivation interfaces. Cross-sectional TEM observations of the deformed films [Fig. 5.2(c)] also confirm the presence of such a boundary layer. The presence of this boundary layer is not surprising since the film-passivation interface blocks gliding dislocations and forms dislocation pileups or more complicated structures there.

The results obtained from the strain-gradient plasticity and the discrete dislocation dynamics can be connected by noticing that dislocation pileups lead to net Burgers

vectors or geometrically necessary dislocations, which are in turn measured by the plastic strain gradients. Furthermore, the thickness of this layer is also close to what observed in TEM and in discrete dislocation simulations.

From the dislocation dynamics point of view, the restriction on dislocation glide imposed by the film-passivation interfaces and by the grain boundaries, as shown in Fig. 5.15(a) and (b), gives rise to a dislocation structure that form a long-range back stress field. The back stress field superimposes on the externally applied stress field, which inhibits subsequent nucleation at dislocation sources and in turn leads to increased stress levels in the films for further plastic deformation, i.e., increased working-hardening rate. This same back stress field assists dislocations to glide back when the external loading direction is reversed, which leads to early reverse plastic flow on unloading, i.e., the Bauschinger effect. The Bauschinger effect will be discussed in more detail in the next chapter.

For unpassivated films, the yield stress varies with film thickness as a result of changes in the average grain size. The variation follows the Hall-Petch relation for both electroplated and sputter deposited Cu films and both agree remarkably well with experimental in Chapter 4.

5.7 Summary

Stress–strain curves of Cu films with thicknesses ranging from 0.34 – 4.2 μm and with various surface passivation conditions have been obtained using the plane-strain

bulge test technique. The yield stress and work hardening rate of a film increase considerably if one surface or both surfaces of the film are passivated. This is due to the constraint on plastic flows at the film-passivation interfaces. The degree of the constraint is affected by the mechanical properties and thickness of the passivating layer. For films with the same passivation condition, the yield stress scales inversely with the film thickness and pronounced Bauschinger effect is observed. By contrast, unpassivated films show only Hall-Petch strengthening due to the variation of grain sizes and negligible hysteresis and Bauschinger effect on unloading.

The experimental results are compared with numerical results based on both the strain-gradient plasticity theory and the discrete dislocation dynamics. Good agreement is obtained between experimental results and simulations based on both models. Fitting the SGP results to the experimental data gives a material length parameter that sets the characteristic length scale of the deformation field at which the size effect becomes dominant. The value of the material length parameter agrees well with results in the literature. The SGP calculations also reveal a boundary layer near the film-passivation interface, which has much larger gradients of plastic strains than the rest part of the films. The thickness of this layer does not scale with the film thickness. As a result, the yield stress of passivated films exhibits strong thickness dependence. This is consistent with the observations in direct simulations of the experiments using discrete dislocation dynamics: A strong interface causes dislocations to pile-up and form a boundary layer with much higher dislocation densities than the rest part of the film and with thickness independent of film thickness. Large plastic strain gradients are associated with high

densities of GNDs, which build up significant back stresses. These back stresses increase the resistance to plastic flow on loading and assists reverse plastic flow on unloading, leading to unusual Bauschinger effects. Grain boundaries also affect the dislocation structures since they are internal obstacles to dislocation motions. As a result, the yield stress of passivated films exhibit strong thickness dependence, while the yield stress of unpassivated films shows Hall-Petch strengthening only.

Chapter 6

Bauschinger effect in Cu thin films[†]

In this chapter, we first introduce a new experimental technique that allows us to isothermally deform thin metal films alternating in tension and compression and to measure the corresponding stress–strain curve. The technique was applied to thin sputter-deposited Al and Cu films. A dislocation based mechanism is proposed to explain the results. Further experiments on passivated Cu thin films with a range of thickness and grain size indicate that the Bauschinger effect scales with the grain aspect ratio, which is consistent with the prediction of the mechanism. Direct simulations of these experiments using discrete dislocation dynamics also support the proposed mechanism.

[†] Based on "*Bauschinger effect in thin metal films*", Y. Xiang and J.J. Vlassak, *Scripta Mater.* **53**, 177-182 (2005) and "*Size effect and Bauschinger effect in freestanding thin films*", Y. Xiang and J.J. Vlassak, *Acta Mater.*, in review (2005).

6.1 Introduction

6.1.1 What is Bauschinger effect?

It is well known that the mechanical response of a metallic material depends not only on its current stress state but also on its deformation history. One of the most important examples is the observation that after a metal is deformed plastically in one direction, the yield stress in the reverse direction is often lower. Figure 6.1 schematically shows a typical stress–strain curve for metallic materials. The stress σ_f is the forward flow stress, and σ_r at the start of reverse plastic flow is the reverse flow stress. If σ_r is

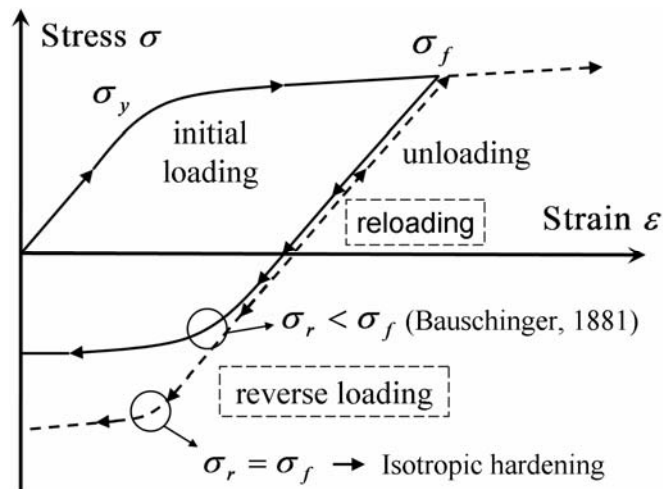


Figure 6.1: Schematic illustration of the typical stress–strain curve of a metallic material that exhibits the Bauschinger effect.

equal to σ_f , the material hardens isotropically. For many metals, however, the reverse flow stress is found to be lower than the forward flow stress. This anisotropic flow behavior was first reported by Bauschinger [132] and is referred to as the Bauschinger effect. The loss of strength due to the Bauschinger effect is of practical importance since the strength of a metal part may be impaired if the working stress acts in the reverse direction compared to the manufacturing stress. Furthermore, a good understanding of the physical origin of the Bauschinger effect may lead to more refined plasticity theories and may ultimately result in materials with superior mechanical behavior. Many experimental and theoretical efforts have been devoted to study the Bauschinger effect in bulk metals since the phenomenon was first reported [133-146]. The physical origins are generally ascribed to either long-range effects, such as internal stresses due to dislocation interactions [137, 138], dislocation pile-ups at grain boundaries [139, 140] or Orowan loops around strong precipitates [141-145], or to short-range effects, such as the directionality of mobile dislocations in their resistance to motion or annihilation of the dislocations during reverse straining [141]. Satisfactory agreement has been achieved between models and experimental results obtained in various bulk metals and alloys [134-136, 138-142].

6.1.2 Bauschinger effect in thin metal films

As discussed in Chapter 2, thin films behave mechanically very differently from their bulk counterparts, especially in the plastic regime [14]. Various theoretical models

and numerical simulations have been proposed to describe thin-film plasticity including strain-gradient plasticity theories [70, 72], crystal plasticity theories [81], and discrete dislocation simulations [76, 77]. The plasticity theories and the discrete dislocation models explain the strengthening effects associated with the film thickness and microstructure reasonably well; they predict, however, different behavior in reverse loading. In the discrete dislocation simulations [81, 94] and some crystal plasticity theories [94], passivated films show a distinct Bauschinger effect upon unloading after plastic pre-straining in tension. Reverse plastic flow starts early even though the overall stress in the film is still in tension. This type of Bauschinger behavior is not predicted in other models [70, 72, 81] and is also very different from that typically found in bulk materials. Up to date, however, there has been no direct experimental evidence of such a Bauschinger effect in thin metal films.

The most common experimental technique for revealing the Bauschinger effect in bulk material is cyclic or unidirectional testing where prestraining in tension is followed by reverse loading in compression. This method cannot be directly applied to thin films because any compressive stress in the plane of a freestanding thin film causes it to buckle due to the large lateral dimension/thickness ratio in thin films.

6.1.3 Objective and overview

In this chapter, we first introduce a new experimental technique to deform thin metal films alternating in tension and compression and to measure the corresponding

stress–strain curves. This technique allows us to quantitatively study the Bauschinger effect in thin metal film and has been applied to thin sputter-deposited Al and Cu films. These preliminary results provide for the first time unambiguous experimental evidence of a strong Bauschinger effect in thin metal films.

We then carry out a systematic study on the influence of various microstructural parameters such as film thickness and grain size on the Bauschinger effect in thin sputter-deposited Cu films with a range of thickness and grain size. The experimental details have been presented in Chapter 5, where the length-scale effect is discussed. In this chapter we focus on the Bauschinger effect observed in these films by accounting for the influence of free surface, interface, and grain boundary on dislocation activity.

6.2. Compression test for thin metal films

6.2.1 The compression test technique

The new experimental method is based on the plane-strain bulge test technique, the details of which are described in Chapter 3. Figure 6.2 illustrates how the bulge test technique can be modified to test metal films in compression. A bilayer membrane is microfabricated consisting of the metal film of interest on a thin ceramic layer such as Si_3N_4 that has a much higher yield strain than the metal film. During the test, the metal film first flows in tension, while the Si_3N_4 layer only deforms elastically. Upon unloading,

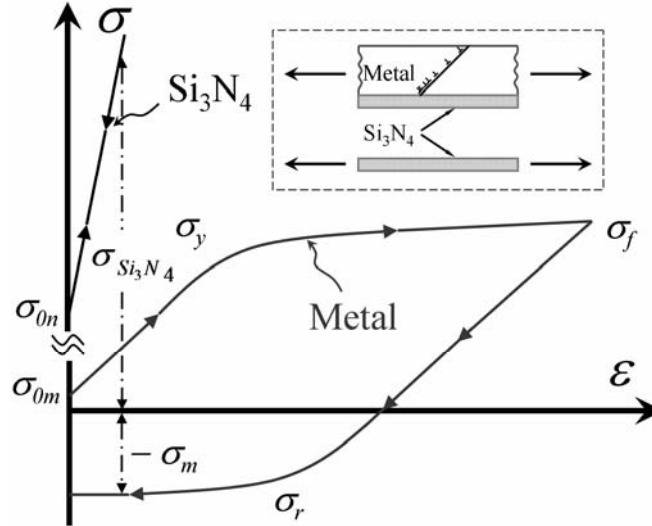


Figure 6.2: The principle of the compression test technique for thin metal films. The stress–strain curves of the metal and ceramic layers in the composite film are schematically shown.

the tensile stress in the Si_3N_4 layer drives the metal film into compression, while the overall stress in the bilayer is kept in tension to prevent buckling of the membrane. The Si_3N_4 film thus serves a dual purpose: it provides the driving force to deform the metal film into compression and it passivates one of the surfaces of the metal film. By adjusting the thickness ratio of the Si_3N_4 layer and the metal film, different levels of compressive stress can be obtained in the metal film.

If the Si_3N_4 film and the metal film are denoted as layers 1 and 2 with thickness h_1 and h_2 , respectively, the average stress in the bilayer, σ_b , is given by

$$\sigma_b = \frac{h_1}{h_1 + h_2} \sigma_1 + \frac{h_2}{h_1 + h_2} \sigma_2, \quad (6.1)$$

where σ_1 and σ_2 are the stresses in the respective layers. These stresses are related to the corresponding strains in each layer through the following constitutive equations

$$\sigma_1 = f_1 \left(\varepsilon_{01} + \frac{2\delta^2}{3a^2} \right) \text{ and } \sigma_2 = f_2 \left(\varepsilon_{02} + \frac{2\delta^2}{3a^2} \right), \quad (6.2)$$

Where δ is the deflection of the bilayer, and ε_{01} and ε_{02} are the residual strains in layers 1 and 2, respectively. Equilibrium requires that the average stress in the membrane depend on the membrane deflection as follows:

$$\sigma_b = \frac{pa^2}{2\delta(h_1 + h_2)}, \quad (6.3)$$

where p is the total pressure supported by the bilayer. From Eqs. (6.1), (6.2), and (6.3), the pressure–deflection relation for the bilayer is found to be

$$p(\delta) = \frac{2\delta h_1}{a^2} f_1 \left(\varepsilon_{01} + \frac{2\delta^2}{3a^2} \right) + \frac{2\delta h_2}{a^2} f_2 \left(\varepsilon_{02} + \frac{2\delta^2}{3a^2} \right). \quad (6.4)$$

We define the pressures p_1 and p_2 as follows

$$p_1(\delta) = \frac{2\delta h_1}{a^2} f_1 \left(\varepsilon_{01} + \frac{2\delta^2}{3a^2} \right) \text{ and } p_2(\delta) = \frac{2\delta h_2}{a^2} f_2 \left(\varepsilon_{02} + \frac{2\delta^2}{3a^2} \right). \quad (6.5)$$

Since the Si_3N_4 film (layer 1) deforms only elastically, the constitutive function f_1 is independent of whether the film is freestanding or part of a bilayer. Comparison of Eqs. (3.1) and (6.4) shows that $p_1(\delta)$ is equal to the pressure required to deflect a

freestanding Si_3N_4 membrane to the deflection δ . According to Eq. (6.4), $p_2(\delta)$ can be obtained by subtracting the pressure–deflection curve of a freestanding Si_3N_4 film from that of the bilayer. The stress–strain curve of the metal film, f_2 , can be calculated from $p_2(\delta)$ using Eq. (3.7). This method is generally applicable as long as the constitutive equation of layer 1, f_1 , does not change when layer 2 is removed.

6.2.2 Application to thin sputter-deposited Al and Cu films

We now apply this technique to thin sputter-deposited Al and Cu thin films. The detailed sample preparation method is discussed in Chapter 3. Briefly, 1 μm thick Al films were sputter deposited onto a Si wafer, coated on both sides with 80 nm of Si_3N_4 by means of low-pressure chemical vapor deposition (LPCVD). Immediately prior to the Al deposition, a thin TiN sticking layer was grown using reactive sputtering. Freestanding Al/TiN/ Si_3N_4 composite membranes were microfabricated by opening rectangular windows in the Si substrate using standard silicon micromachining techniques. Freestanding Cu/ Si_3N_4 bilayers were prepared by first microfabricating freestanding Si_3N_4 membranes followed by sputter depositing 600 nm Cu films directly on top of the Si_3N_4 membranes. Both sets of samples were vacuum annealed at 300°C to stabilize the microstructure. Freestanding Al and Cu membranes were prepared by etching the Si_3N_4 or $\text{Si}_3\text{N}_4/\text{TiN}$ layer beneath the metal films using reactive ion etching (RIE). Transmission electron microscope (TEM) micrographs in Fig. 6.3 show that grains in

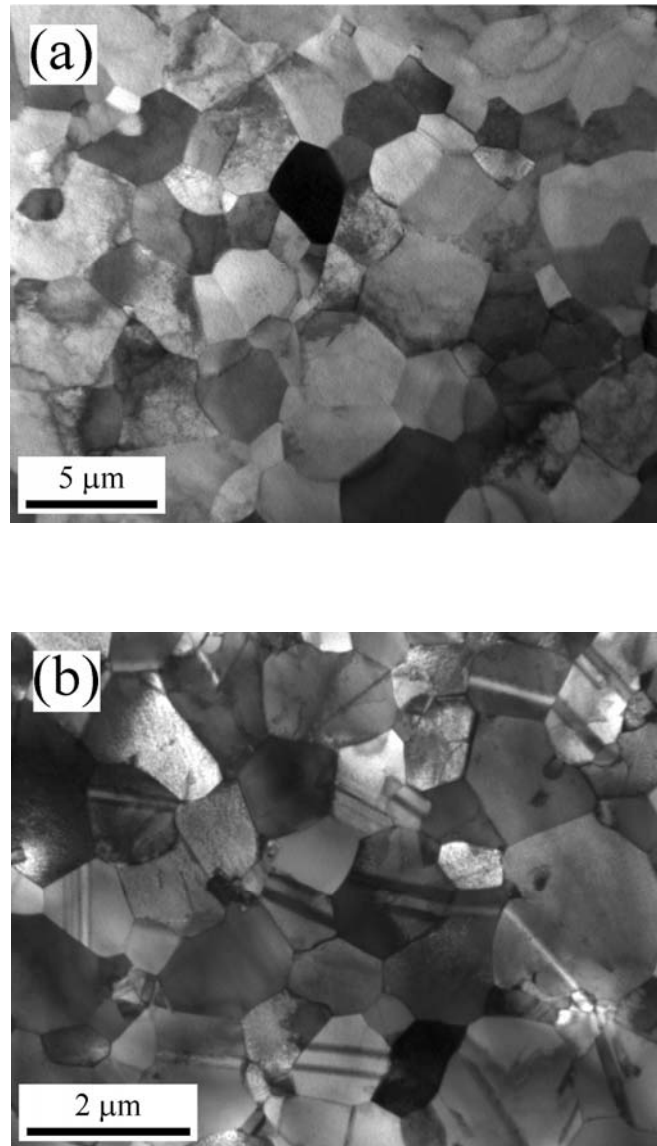


Figure 6.3: TEM micrographs showing the grain structure of a 1 μm Al film (a) and a 0.6 μm Cu film (b).

both films are roughly equiaxed and that the average grain size is 2.1 μm for Al and 0.9 μm for Cu. Both films have a columnar grain structure with grain boundaries traversing the thickness of the film. Annealing twins are only found in Cu grains.

Both composite and freestanding films were tested in multiple loading/unloading cycles with a bulge test apparatus [147]. For the Cu/Si₃N₄ samples, the elastic contribution of the Si₃N₄ films was measured independently by dissolving the Cu in dilute nitric acid and testing the Si₃N₄ membranes separately. The pressure–deflection of the Cu/Si₃N₄ bilayer and the freestanding Si₃N₄ membrane are plotted in Fig. 6.4. The curve of the freestanding Si₃N₄ membrane consists of both loading (solid line) and unloading (solid squares) sections. It can be seen that the deformation of the Si₃N₄ membrane is elastic. For a given deflection, the difference between the pressures supported by the bilayer and the Si₃N₄ membrane gives the contribution of the Cu film, as illustrated by the insert in Fig. 6.4. The stress–strain curve of the Cu film is then calculated using equation (1) and (6). The same method could not be applied to the Al samples because the TiN had a large compressive stress that caused the freestanding Si₃N₄/TiN bilayer to buckle if the Al was dissolved. Instead, the properties of the Si₃N₄/TiN were obtained from the elastic unloading curves of both Si₃N₄/TiN/Al and freestanding Al films [59]. The elastic contribution of Si₃N₄/TiN bilayer can then be subtracted from the data of the Si₃N₄/TiN/Al composite films.

The resulting stress–strain curves are presented in Figs. 6.5(a) and 6.5(b) for passivated Cu and Al film, respectively. Also plotted in Fig. 6.5 are typical stress–strain

curves for unpassivated Cu and Al films. For both materials, the passivated films show a very strong Bauschinger effect: during unloading, reverse plastic flow starts when the applied stress is still in tension and continues when the films are loaded in compression. Each loading cycle shows significant hysteresis, which increases with increasing plastic strain. By contrast, the stress–strain curves of unpassivated films have unloading cycles with little or no hysteresis.

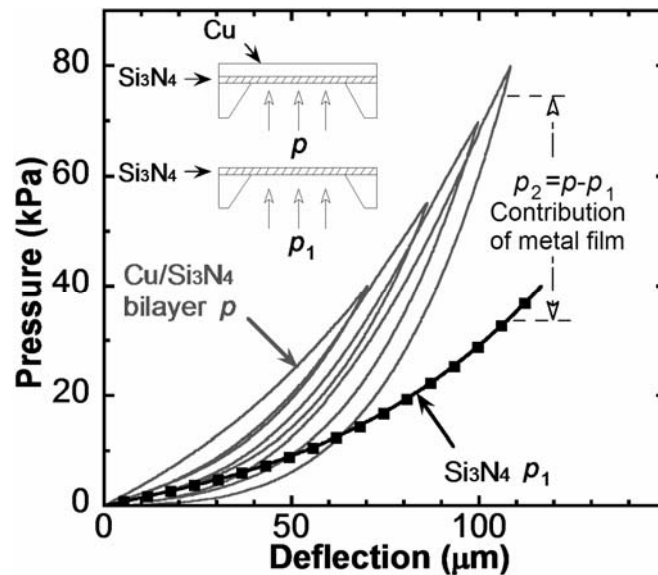


Figure 6.4: Pressure–deflection curves of the Cu/Si₃N₄ bilayer and the freestanding Si₃N₄ film. For clarity, only every twentieth data point of the Si₃N₄ unloading curve is displayed (■).

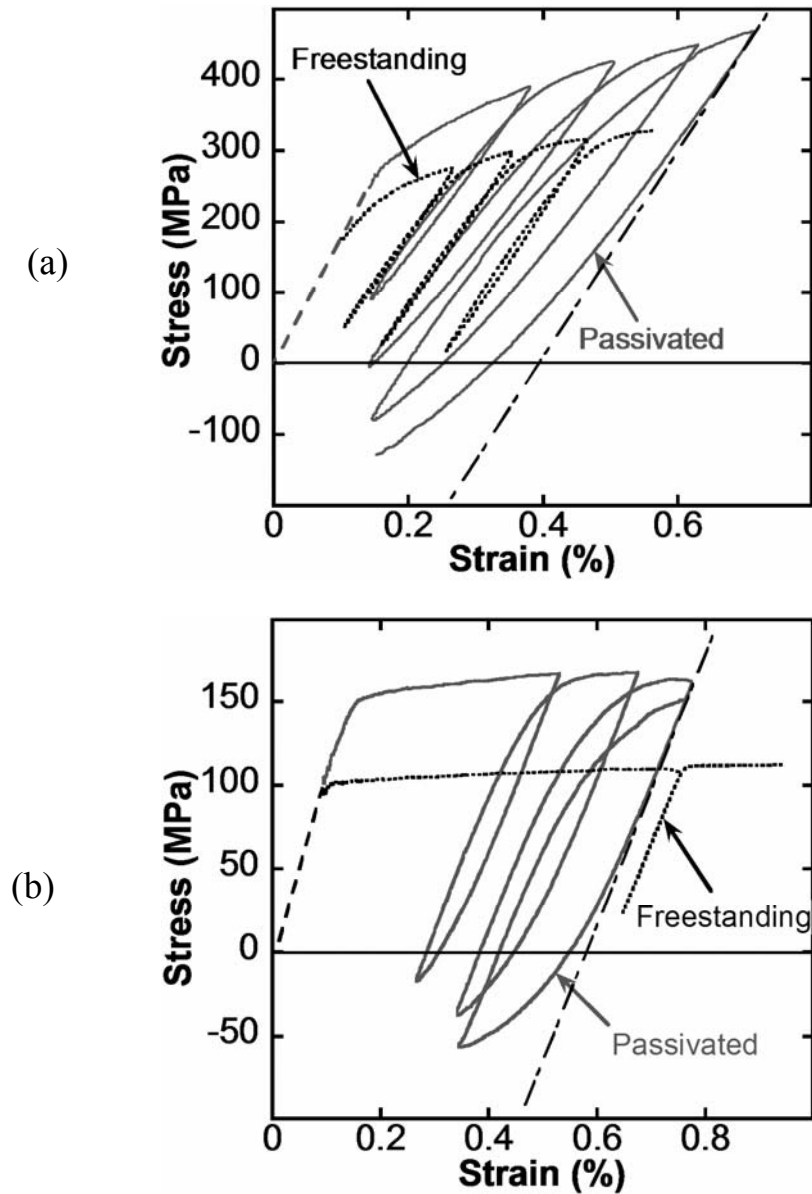


Figure 6.5: Stress–strain curves of passivated and freestanding films for a 0.6- μm Cu film (a) and a 1.0- μm Al film (b). The stress–strain curves are offset by the biaxial residual strains in the films, as represented by the dashed lines starting from the origins in the stress–strain curves.

6.2.3 Discussion

A dislocation-based mechanism is proposed to explain the difference between passivated and unpassivated films. Figure 6.6 depicts a thin metal film with a columnar grain structure. The lower surface of the film is passivated by a material that forms a strong interface, while the upper surface is free. When dislocations reach an obstacle such as a grain boundary or a strong interface during forward plastic deformation, they form pileups; when they reach a free surface, they simply exit the material to form surface steps. In the presence of pile-ups, dislocations in the film are subject to two types of stress: the externally applied stress and the internal stress imposed by the pileups; the former provides the driving force for further plastic flow, while the latter acts as a resistance. During tensile loading of a passivated film, dislocation pile-ups form at the

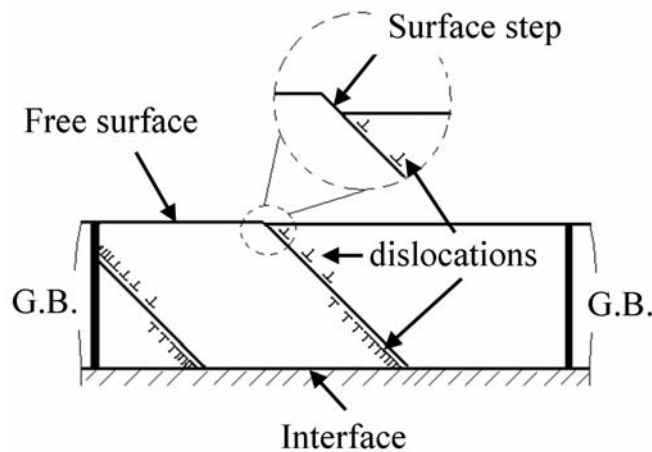


Figure 6.6: Dislocations interact with grain boundaries as well as free surfaces and interfaces in thin films.

film/passivation interface resulting in significant back stresses in the film. Upon unloading, these back stresses cause dislocations to glide in the opposite direction resulting in a nonlinear unloading curve. The different behavior of passivated and freestanding films arises as follows. In freestanding films, many dislocations can exit the film due to the proximity of the free surface and no significant Bauschinger effect is observed. If one of the film surfaces is passivated [Fig. 6.6] and the interface is strong, a boundary layer with high dislocation density is formed near the interface [76]. This boundary layer, which may consist of simple pileups or may have a more complex structure, has an associated back stress that is not present in freestanding films. As a result of this high back stress, reverse plastic flow starts much earlier during the reverse loading cycle. If the back stress is large enough, reverse flow can start even when the externally applied stress is still in tension, as observed in the stress–strain curves of the passivated Cu and Al film in Fig. 6.5. It should be noted that the Bauschinger effect will occur only when the obstacle to dislocation motion is strong enough to cause significant back stresses. The data in Fig. 6.5(b) suggest that this is not the case for the thin native oxide that forms on freestanding Al films.

In addition to the composite-film technique proposed here, the substrate curvature technique can also be used to load thin films deposited on a substrate alternating in tension and compression. In this technique, a metal film on a silicon substrate is loaded into compression by heating the sample until the residual stress in the film becomes compressive due to the thermal mismatch with the substrate. Upon cooling, the film goes into tension. From the change in substrate curvature, one can determine the stress in the

film and thus obtain an estimate for the forward and reverse flow stress. Using this technique, Baker *et al.* [148] observed "anomalous" thermomechanical behavior for Cu films encapsulated between Si₃N₄ barrier and passivation layers, when a small amount of oxygen was introduced in the deposition system during film growth: the films exhibited a Bauschinger-like behavior that is large compared to that observed for bulk Cu. The result is difficult to interpret, however, because the applied strain cannot be decoupled from the temperature change and because at elevated temperatures other deformation mechanisms such as diffusional creep may come into play [149]. Compared to the substrate curvature technique, the composite film technique proposed here has the unique advantage of measuring the isothermal stress–strain behavior and is thus ideal for studying Bauschinger effect in thin metal films.

6.3 The influence of free surfaces, interfaces, and grain boundaries on Bauschinger effect

In this section, we discuss the influence of the microstructural parameters, such as free surfaces, interfaces, grain boundaries, on Bauschinger effect in Cu thin films. The discussion is based on the experimental results for the third set of samples in the previous chapter, i.e., the sputter-deposited Cu films with thickness ranging from 0.34 to 0.89 μm .

6.3.1 Experimental results

The stress–strain curves for both passivated and unpassivated films are presented in Fig. 5.6. In order to quantitatively compare the Bauschinger effect in passivated and unpassivated films, the reverse plastic strain during each unloading cycle, ε_{rp} , is plotted as a function of total prestrain, ε_p , in Fig. 6.8. Both strains are normalized by the yield strain of the films, ε_y , as defined in the inset of Fig. 6.7. The difference between the passivated and unpassivated films is immediately evident. Moreover, for passivated films, it is noted that the Bauschinger effect increases with the increasing grain aspect ratio h/d . This is due to the constraint of both the grain boundaries and the film-passivation interface and will be discussed in more detail later in the discussion section.

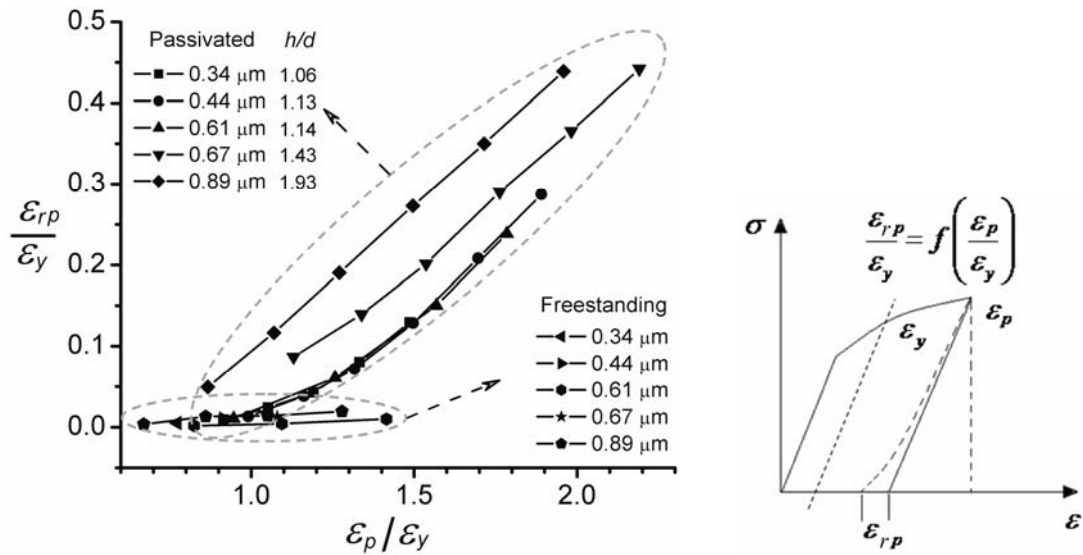


Figure 6.7: Bauschinger effect in sputter-deposited Cu films: the reverse plastic strain, ε_{rp} , as defined in the inset, versus the applied prestrain, ε_p . Both strains are normalized

by the yield strain, $\varepsilon_y = \sigma_y(1-\nu^2)/E$.

6.3.2 Comparison and discussion

The Fleck-Hutchinson theory used for the calculations in Section 5.4 does not provide a constitutive description for unloading and therefore the Bauschinger effect cannot be directly predicted from the calculations. The calculated distributions of plastic strains [Fig. 5.11(b)] and their gradients [Fig. 5.17] across the film thickness, however, suggest a potential mechanism for the unusual Bauschinger effect observed in these experiment. The presence of a boundary layer with large plastic strain gradients suggests that GNDs of a high density are formed near the interface. The net Burgers vector of the GNDs then leads to a directional back stress and therefore the flow asymmetry or Bauschinger effect found in the stress-strain curves. This observation would argue for inclusion of a back stress in the Fleck-Hutchinson theory. Such a back stress would naturally lead to a certain degree of kinematic hardening and could be used to describe the Bauschinger effect in thin films. There is, however, no simple relation between the GND density and the degree of kinematic hardening versus isotropic hardening [83]. Moreover, the influence of microstructure is not reflected.

The experiments were also simulated directly using discrete dislocation dynamics, as summarized in Section 5.5. The calculated stress-strain curves for two films with distinct thickness and grain size [(a) $h = 1 \mu\text{m}$, $d = 1.5 \mu\text{m}$ and (b) $h = 0.6 \mu\text{m}$, $d = 0.5 \mu\text{m}$] are presented in Fig. 6.8, in which curves for both unpassivated films and films with one surface passivated are plotted together. The influence of passivation and grain aspect ratio on the Bauschinger effect is clearly shown. In Fig. 6.8(a), the unpassivated film exhibits almost no hysteresis, while the passivated film shows a

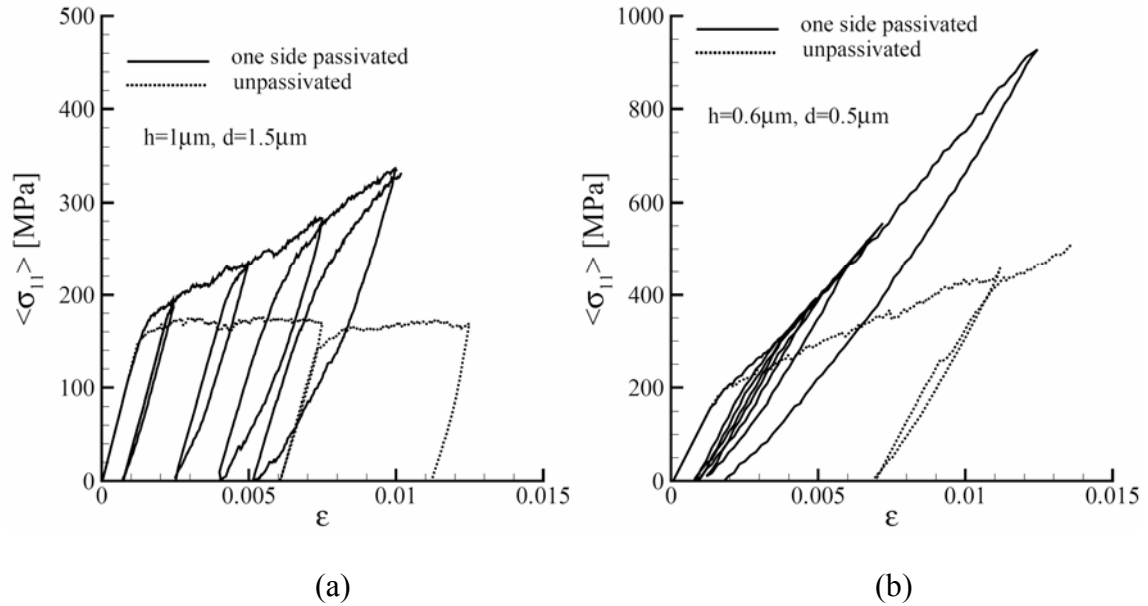


Figure 6.8: Discrete dislocation simulations predict significant Bauschinger effect in films with one surface passivated: (a) $h=1\mu\text{m}$, $d=1.5\mu\text{m}$ and (b) $h=0.6\mu\text{m}$, $d=0.5\mu\text{m}$. By contrast, little or no reverse plastic flow is observed in unpassivated films. (From [88]).

pronounced Bauschinger effect with the hysteresis loop increasing with the prestrain. In Fig. 6.8(b), the film is thinner and has a smaller grain size, but the grain aspect ratio is larger. Both the passivated and unpassivated films show a significantly higher work-hardening rate than the other film. The hysteresis loop in the passivated film is also larger. Even for the unpassivated film, there is also some degree of hysteresis. This is due to dislocation pile-ups that form at the grain boundaries. The simulated curves for both sets of films reproduce the trends observed in the experimental curves in Fig. 5. 6.

The normalized reverse plastic strain during each unloading cycle is determined from the calculated stress–strain curves and plotted as a function of the normalized total prestrain. Figure 6.9 compares the simulated results with those obtained from the experimental stress–strain curves. In both experiments and computations, the unpassivated films show nearly no Bauschinger effect, while the passivated films exhibit a pronounced Bauschinger effect that increases with increasing prestrain. There is no obvious dependence of the Bauschinger effect on the grain aspect ratio in the simulations, while the experimental results clearly suggest that the effect increases with increasing grain aspect ratio for a given prestrain.

Now we explain the dependence of the Bauschinger effect on the grain aspect ratio. The dislocation-based mechanism proposed in Section 6.2.3, as illustrated in Fig. 6.6, suggests that a free surface facilitates the escape of dislocations from the material, while a strong interface inhibits dislocations from doing so and results in the formation of dislocation pile-ups or more complex structures at the interface, which causes significant back stresses. Grain boundaries can block dislocations in the material but also acts as dislocation sources. As a result, for passivated films, significant back stresses are generated, providing a large driving force for dislocations to glide back during unloading. For films with the same grain size, thicker films have larger grain boundary areas so there are more dislocation sources; a larger grain aspect ratio (h/d) also helps keep more dislocations from exiting the material. This is confirmed by the discrete dislocation simulations, as shown in Fig. 6.10. The calculated dislocation density is higher in thicker films if the grain size is the same [Fig. 6.10(a)]. In other words, there are more

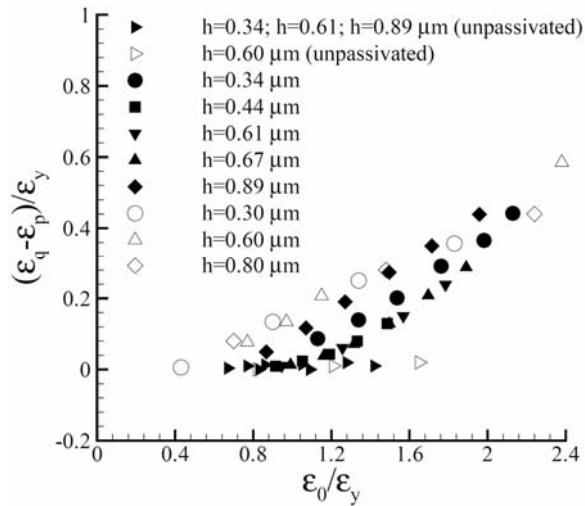


Figure 6.9: The reverse plastic strain as a function of the total prestrain for each unloading loop of the stress–strain curves obtained by numerical simulations [open symbols] and experimental measurements [filled symbols]. Both strains are normalized by the corresponding yield strains. (From [88]).

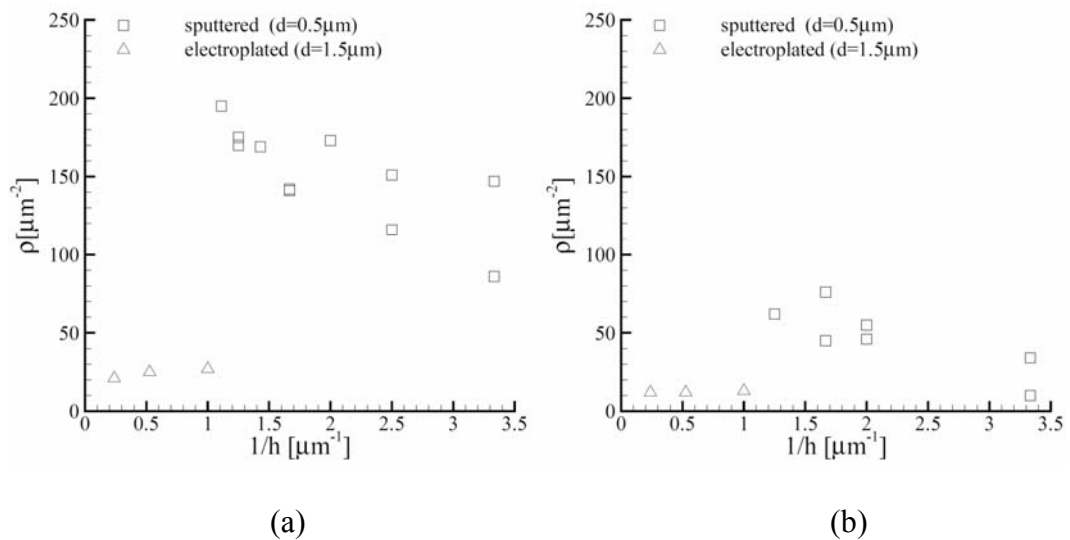


Figure 6.10: Calculated dislocation density at approximately yield stress versus the reciprocal of film thickness. Figures are taken from [88].

dislocations *available* to glide back, and/or more dislocation sources to provide *enough* dislocations available to glide back, when the loading direction is reversed.

By contrast, for unpassivated films, no significant back stresses are generated and thus there is no significant driving force. The dislocation density is also much lower [Fig. 6.10(b)] and thus fewer dislocations are available to glide back when the loading direction is reversed. Grain boundaries may cause a certain degree of dislocation pile-ups, as suggested by the discrete dislocation simulations in Fig. 5.14(c), and thus a small amount of hysteresis is also observed when unpassivated films are fully unloaded. These arguments naturally lead to the experimental results in Fig. 6.7: (i) For films with one surface passivated, the Bauschinger effect scales with the grain aspect ratio h/d , i.e., for films with same grain size, thinner films show less BE because less dislocations are left in the material. (ii) Unpassivated films show negligible reverse plastic deformation due to a smaller dislocation density and lack of back stresses in these films.

6.3.3 Length-scale effect versus Bauschinger effect

In Chapter 5, we discussed the length-scale effect associated with surface passivation and film thickness in thin films. Based on the same set of experiments, we discussed the Bauschinger effect in this chapter. It is evident that both effects are results of the dislocation activity in the materials and are affected by various microstructural parameters that affect the formation of a dislocation structure, such as the material volume, free surfaces, interfaces, grain boundaries, crystallographic texture, and internal obstacles such as existing dislocation structures. For example, the nucleation and storage

of dislocations are energetically unfavorable in materials of small volumes, where dislocation sources are also limited; a free surface provides attracting image forces, allowing dislocations to exit the material; interfaces prevent dislocations from exiting the material, allowing back stresses to build up; grain boundaries can be effective internal obstacles to dislocation motions, as well as dislocation sources.

Both the length-scale and the Bauschinger effects sometimes originate from the same source, e.g., the passivated films in the current study. Surface passivation prevents dislocations from exiting the films and plastic flow is thus constrained at the interface. A boundary layer with large plastic strain gradients is formed near the interface, which significantly increases the resistance for plastic flow. The thickness of this boundary layer does not scale with film thickness, which leads to the length-scale effect. The plastic strain gradients are associated with geometrically necessary dislocations or net Burgers vectors. Due to the directionality of GNDs or net Burgers vectors, the hardening intrinsically possesses a kinematic nature, which leads to the flow asymmetry, or the Bauschinger effect, in the stress–strain curves. For a given applied strain, the plastic strain distribution in thinner films is less uniform than in thicker films and the average plastic strain is smaller [Fig. 5.11(b)].

The same phenomena can also be explained using the discrete dislocation mechanisms. Passivation causes dislocation pile-ups or more complex dislocation structures near the interface leading to significant back stresses to build up there. Back stresses restrict on dislocation glide and/or suppress dislocation nucleation, which increases the resistance for further plastic flow but assists the reverse plastic deformation

by driving dislocations to glide back on unloading. A pronounced Bauschinger effect requires not only significant back stresses, but also *enough* dislocations *available* to glide back. This explains why thinner films have less reverse plastic flow on unloading after the films is subjected to the same amount of prestrain, because the dislocation density is lower as shown in Fig. 6.10.

In more general cases, the length-scale effect is not necessarily related to the Bauschinger effect. For example, the size effect can arise from limited dislocation sources [87, 89], in which case a significant Bauschinger effect may not be expected.

6.4 Summary

In this chapter, we have systematically investigated the Bauschinger effect in Cu thin films using a new experimental technique that allows us deform thin metal films alternating in tension and compression and to measure the corresponding isothermal stress–strain curve. A detailed analysis of this technique is given with application to Al and Cu thin films. Both passivated Al and Cu films exhibit an unusual Bauschinger effect with reverse plastic flow occurring on unloading even when the overall film stress is still in tension. By contrast, stress–strain curves of unpassivated films show little or no reverse flows when the film is fully unloaded. Further experiments on Cu films with a range of film thicknesses and grain sizes exhibit that the Bauschinger effect increases with increasing grain aspect ratio for films with one surface passivated.

A dislocation based mechanism is proposed to explain the observed phenomena. Both the film-passivation interfaces and the grain boundaries prevent dislocations from exiting the film and allow the buildup of significant back stresses. On unloading, these back stresses provide a driving force for dislocations to glide back, causing the reverse plastic flow. For films with higher aspect ratios, the grain boundaries help keep more dislocations in the material. The increased dislocation density results in higher back stresses, which in turn lead to a larger reverse plastic flow on unloading due to a larger driving force and more dislocations available to glide back. As a result, the Bauschinger effect increases with increasing aspect ratios. For unpassivated films, the free surface allows dislocations to exit the film and no back stresses are generated; therefore no significant Bauschinger effect is observed. A small amount of hysteresis observed in some of the unpassivated films is due to dislocation pile-ups at grain boundaries. The mechanism is supported by discrete dislocation simulations.

Chapter 7

Conclusions and outlook

7.1 Summary and concluding remarks

The goal of this thesis was to develop a basic understanding of the plasticity in Cu thin films at room temperature. An accurate measurement of the mechanical properties of the films was the first step toward that objective. The plane-strain bulge test was chosen as our mechanical characterization technique. In this technique, the stress–strain curve of a thin film is determined from the pressure–deflection behavior of a long rectangular membrane made of the film of interest. The technique has a number of advantages. For example, it involves minimal sample handling, it is an isothermal measurement, and it measures the intrinsic film properties since it tests directly on a freestanding film. Moreover, for a membrane in a state of plane strain, film stress and strain are distributed uniformly across the membrane width and simple analytical formulae for stress and strain

can be established. These features make the plane-strain bulge test ideal for studying the mechanical behavior of thin films in both the elastic and plastic regimes. In this thesis, a finite element analysis was performed to ensure the accuracy and reliability of the technique and confirmed that the plane strain condition holds for rectangular membranes with aspect ratios greater than 4, and that the simple analytical formulae used to calculate the stress–strain curves from the pressure–deflection data are highly accurate for materials with strain-hardening exponents ranging from 0 to 0.5. It was found that the residual stress in the film affects mainly the elastic deflection of the membrane and changes the initial point of yield in the plane-strain stress–strain curve, but there is little or no effect on further plastic deformation. The effect of the residual stress can be eliminated by converting the plane-strain curve into the equivalent uniaxial stress–strain relationship using von Mises effective stress and strain. A versatile sample preparation was developed to fabricate freestanding membranes out of the film of interest using standard Si micromachining technology and an automated bulge test apparatus with high displacement and force measurement resolutions was constructed. Typical experimental procedures and data analysis were demonstrated for an electroplated Cu film. The experimental results are in good agreement with the finite element calculations.

Using the plane-strain bulge test technique, we carried out a series of experiments to investigate the effects of film microstructure, film thickness, and surface passivation on the elastic-plastic behavior of Cu thin films. Cu films with thickness ranging from sub-micrometer to several micrometers were fabricated either by electroplating or by sputtering. Suitable heat treatments were employed to obtain a wide range of

microstructure in these films. The microstructure was carefully characterized using a variety of microscopic techniques. Some of the films were passivated on one surface or both surfaces with thin layers of Ti or Si₃N₄. The stress–strain curves were measured using the plane-strain bulge test and the mechanical properties are determined as a function of film thickness and microstructure for films both with and without surface passivation. Experimental results are summarized below.

The stiffness of the Cu films varies as a result of changes in the crystallographic texture and the elastic anisotropy of Cu. Experimental stiffness values agree well with values calculated based single-crystal elastic constants and the appropriate orientation distribution functions. No modulus deficit is observed in both electroplated and sputtered Cu films.

The yield stress of freestanding Cu films without surface passivation varies mainly as a result of changes in the grain size of the films. The average grain size of the films ranges from 0.3 – 6.1 μm. The yield stress follows typical Hall-Petch behavior if twins are counted as distinct grains, indicating that twin boundaries are effective barriers to dislocation motion. The Hall-Petch coefficient obtained for electroplated films agree remarkably well with that for sputtered films, both of which are also in good agreement with values reported for bulk Cu. Film thickness and crystallographic texture have a negligible effect on the yield stress of unpassivated films. These results indicate that grain boundary strengthening is the main working mechanism for unpassivated Cu thin films at room temperature independent of whether the films are electroplated or sputter-deposited.

The yield stress and work hardening rate of the Cu films increase considerably if one surface or both surfaces of the films are passivated because dislocation motions are restricted at the film-passivation interfaces and the plastic flows in the films are constrained. For films with constant microstructure and surface passivation, the yield stress scales inversely with the film thickness. A new experimental technique that allows us to isothermally deform a metal film alternating in tension and in compression was developed and employed to investigate the Bauschinger effect in passivated Cu films. These films exhibit a pronounced Bauschinger effect with the reverse plastic flow already occurring on unloading. The effect increases with increasing grain aspect ratio for films with a columnar grain structure and with one surface passivated. By contrast, unpassivated films show no or little hysteresis when fully unloaded.

The plastic behavior of passivated films was explained using two different approaches: the strain-gradient plasticity (SGP) and the discrete dislocation dynamics. The two approaches can be connected by noticing that the plastic strain gradient is a measure of the density of geometrically necessary dislocations. By fitting the SGP calculations to the experimental results, a material length parameter $l = 0.345 \mu\text{m}$ is obtained, which agrees well with values in the literature. This parameter characterizes the length scale of the deformation field at which the contribution of plastic strain gradients to material hardening is comparable to that of plastic strains. The calculations also reveal a boundary layer near the film-passivation interface, which has much larger gradients of plastic strains and higher stress levels than the rest part of the film and the thickness of which is independent of film thickness. As a result, the average stress in the films

increases with decreasing film thickness. The SGP results predict the length-scale effect well, which is consistent with direct simulations of the experiments using discrete dislocation dynamics, where a boundary layer is also observed with much higher dislocation densities and with its thickness independent of film thickness. The discrete dislocation simulations reproduce the trends in the experiments and are in quantitative agreement with the experimental measurements for both length-scale and Bauschinger effects. The SGP theory used in this thesis, however, does not provide a description of Bauschinger effect.

The mechanism for the plastic behavior of passivated films was hence recognized: The presence of any passivation layers causes dislocations to pile up and form a boundary layer with high dislocation density near the interface leading to a significant back stress field, which superimposes on the externally applied stress field in the film. The directionality of the back stress field naturally leads to the flow asymmetry in the stress–strain curves: It increases the forward plastic flow resistance on loading but assists the reverse plastic flow on unloading, leading to the increased forward yield stress and the distinct Bauschinger effect in passivated films. The size dependence arises from that the boundary layer does not scale with the film thickness; hence the influence of the back stress field increases with decreasing film thickness.

Now we draw the conclusions:

1. The elastic behavior of the freestanding Cu films is controlled by the crystallographic texture and elastic anisotropy of the film. No modulus deficit is observed.

2. The plastic behavior of the freestanding Cu films is affected by the grain size, film thickness, and surface passivation. The material strengthening in thin films is due to the constrained dislocation activity at both grain boundaries and any film-passivation interfaces. As a result, the yield stress of unpassivated films is dominated by the average grain size, while the yield stress of passivated films is a function both film thickness and grain size.
3. The strain-gradient plasticity theory by Fleck and Hutchinson provides a good description of the length-scale effect for these films but does not capture the Bauschinger effect. Discrete dislocation simulations agree quantitatively well with the experimental results for both film thickness and Bauschinger effects.

7.2 Suggestions for future work

In this thesis, we have recognized the influence of crystallographic texture, grain size, film thickness, and surface passivation on the elastic-plastic behavior of Cu thin films at room temperature. In addition to the mechanisms identified in this study, there are some other microstructural mechanisms that may affect the mechanical behavior of thin metal films, which can be further explored in the future work.

For example, although not present in our films, precipitates or second phases in thin metal films can also affect their hardening behavior. The precipitation strengthening can be investigated by proper modification of the microstructure of Cu films. Potential material systems are alloys of Cu with Ag, Cd, Zr, Ta, or Cr. Since Cu has a very low

solubility for these elements, samples can be prepared by sputter deposition followed by a suitable heat treatment. The stress evolution in the heat treatment can be studied using the substrate curvature technique and the microstructure can be characterized using TEM. Kinetics of the precipitation in these films can also be studied through iso-thermal stress-relaxation experiments using the substrate curvature technique. The stress–strain curves of both as-deposited and annealed films can be measured using the plane-strain bulge test technique and the mechanical properties, such as yield stress and strain-hardening rate, can be related to the concentration of the precipitation.

The fatigue behavior and fracture toughness of metal thin films are also of practical interest. For example, as an essential component of the emerging flexible flat panel display, the metallic interconnect lines will need to survive relatively large stretches and hundreds of thousands of cyclic deformations. Thin metal films with high ductility and high fatigue resistance are thus critical to the development of the promising technology. Some initial finite element analysis [150] and experimental work [151] have demonstrated that the rupture strains of metal films deposited on polymeric substrate are sensitively controlled by their adhesion to the substrates. A good understanding of the underlying microstructural mechanisms is very important and requires additional experimental and modeling efforts. Qualitative work on the fatigue damage of Cu thin films deposited on polyimide substrate under uniaxial tension and compression has been reported [152]. The fatigue behavior of ultra-thin metal films can be quantitatively studied using the plane-strain bulge test. Similar to the experiments for Bauschinger effect, very thin films can be deposited onto freestanding Si_3N_4 membranes and the metal

is tested alternating in plane-strain tension and compression. One of the unique advantages of this experiment is that the stress–strain curve of the metal film can be accurately measured, as compared with the work in [152], where no stress values were measured. Fracture toughness can also be measured using the plane-strain bulge test technique. The only difference from the above configuration is that a pre-crack can be made in the metal film using focused ion beams before the composite metal/Si₃N₄ membranes are tested. A detailed analysis on propagation of the channeling cracks in such a configuration has been published by Vlassak [153].

The time-dependent deformations in metal thin films on substrates have been studied widely in the literature. There is relatively few work for similar behavior in freestanding films. The creep or stress-relaxation behavior in freestanding films can be measured at both room temperature and elevated temperatures using the plane-strain bulge test. For that purpose, additional improvements on the current bulge test system are needed. For example, the experiment control software needs to be revised such that a constant stress can be maintained in the film. A heating element or a furnace may to be added into the bulge test apparatus for measurements at elevated temperatures. Similar to what we have done in this thesis, the influence of microstructure, film thickness, surface passivation on these behaviors can be systematically investigated. The results can be also compared to those obtained using the substrate curvature technique in the literature and to improve our understanding the deformation mechanisms at both room and elevated temperatures.

Bibliography

1. D. Edelstein, H. Rathore and C. Davis et al.: Comprehensive reliability evaluation of a 90 nm CMOS technology with Cu/PECVD low-k BEOL, in *Proceedings of 2004 IEEE International Reliability Physics Symposium*, edited by IEEE (IEEE Piscataway, NJ, USA, 2004), p.316
2. S.M. Spearing: Materials issues in microelectromechanical systems (MEMS). *Acta Mater.* **48**, 179 (2000).
3. W.D. Nix: Mechanical properties of thin films. *Metall. Trans. A* **20**, 2217 (1989).
4. J. Proost and F. Spaepen: Evolution of the growth stress, stiffness, and microstructure of alumina thin films during vapor deposition. *J. Appl. Phys.* **91**, 204 (2002).
5. F. Spaepen: Interfaces and stresses in thin films. *Acta Mater.* **48**, 31 (2000).
6. R.P. Vinci and J.J. Vlassak: Mechanical behavior of thin films. *Annu. Rev. Mater. Sci.* **26**, 431 (1996).
7. S.C. Seel, C.V. Thompson, S.J. Hearne and J.A. Floro: Tensile stress evolution during deposition of Volmer-Weber thin films. *J. Appl. Phys.* **88**, 7079 (2000).
8. W.D. Nix and B.M. Clemens: Crystallite coalescence: A mechanism for intrinsic tensile stresses in thin films. *J. Mater. Res.* **14**, 3467 (1999).

9. D.W. Hoffman and J.A. Thornton: Compressive Stress Transition In Al, V, Zr, Nb And W Metal-Films Sputtered At Low Working Pressures. *Thin Solid Films* **45**, 387 (1977).
10. D.W. Hoffman and J.A. Thornton: Internal-Stresses In Sputtered Chromium. *Thin Solid Films* **40**, 355 (1977).
11. R.W. Hoffman: Stresses In Thin-Films - Relevance Of Grain-Boundaries And Impurities. *Thin Solid Films* **34**, 185 (1976).
12. F.A. Doljack and R.W. Hoffman: Origins Of Stress In Thin Nickel Films. *Thin Solid Films* **12**, 71 (1972).
13. R.G. Filippi, J.F. McGrath, T.M. Shaw and C.E. Murray: Thermal cycle reliability of stacked via structures with copper metallization and an organic low-k dielectric, in *2004 IEEE International Reliability Physics Symposium Proceedings*, edited by IEEE (IEEE, Piscataway, NJ, 2004), p.61
14. E. Arzt: Size effects in materials due to microstructural and dimensional constraints: A comparative review. *Acta Mater.* **46**, 5611 (1998).
15. J.W. Hutchinson: Plasticity at the micron scale. *Int. J. Solids Struct.* **37**, 225 (2000).
16. C.V. Thompson: Grain-Growth In Thin-Films. *Annu. Rev. Mater. Sci.* **20**, 245 (1990).
17. C.V. Thompson: Structure evolution during processing of polycrystalline films. *Annu. Rev. Mater. Sci.* **30**, 159 (2000).
18. C.V. Thompson and R. Carel: Texture Development In Polycrystalline Thin-Films. *Materials Science And Engineering B-Solid State Materials For Advanced Technology* **32**, 211 (1995).
19. M.A. Haque and M.T.A. Saif: Mechanical behavior of 30-50 nm thick aluminum films under uniaxial tension. *Scripta Mater.* **47**, 863 (2002).
20. R.O. Scattergood and C.C. Koch: A Modified-Model For Hall-Petch Behavior In Nanocrystalline Materials. *Scripta Metallurgica Et Materialia* **27**, 1195 (1992).
21. J. Schiotz, F.D. Di Tolla and K.W. Jacobsen: Softening of nanocrystalline metals at very small grain sizes. *Nature* **391**, 561 (1998).
22. F. Spaepen and D.Y.W. Yu: A comparison of the strength of multilayers, thin films and nanocrystalline compacts. *Scripta Mater.* **50**, 729 (2004).

23. J.J. Clement and C.V. Thompson: Modeling Electromigration-Induced Stress Evolution In Confined Metal Lines. *J. Appl. Phys.* **78**, 900 (1995).
24. R.H. Havemann and J.A. Hutchby: High-performance interconnects: An integration overview. *Proc. IEEE* **89**, 586 (2001).
25. C.V. Thompson and J. Cho: A New Electromigration Testing Technique For Rapid Statistical Evaluation Of Interconnect Technology. *Ieee Electron Device Letters* **7**, 667 (1986).
26. B.C. Valek, N. Tamura, R. Spolenak, W.A. Caldwell, A.A. MacDowell, R.S. Celestre, H.A. Padmore, J.C. Braman, B.W. Batterman, W.D. Nix and J.R. Patel: Early stage of plastic deformation in thin films undergoing electromigration. *J. Appl. Phys.* **94**, 3757 (2003).
27. The National Technology Roadmap for Semiconductors (Semiconductor Industry Association, 1997), pp.11
28. B. Zhao, D. Feiler, V. Ramanathan, Q.Z. Liu, M. Brongo, J. Wu, H. Zhang, J.C. Kuei, D. Young, J. Brown, C. Vo, W. Xia, C. Chu, J. Zhou, C. Nguyen, L. Tsau, D. Dornish, L. Camilletti, P. Ding, G. Lai, B. Chin, M. Johnson, J. Turner, T. Ritzdorf, G. Wu and L. Cook: A Cu/low- k dual damascene interconnect for high performance and low cost integrated circuits, in *1998 Symposium on VLSI Technology Digest of Technical Papers*, edited by (IEEE, New York, NY, 1998), p.28
29. L.B. Freund and S. Suresh, Thin film materials: stress, defect formation, and surface evolution (Cambridge University Press, New York, 2003),
30. M.T. Perez-Prado and J.J. Vlassak: Microstructural evolution in electroplated Cu thin films. *Scripta Mater.* **47**, 817 (2002).
31. A. Gangulee: Structure Of Electroplated And Vapor-Deposited Copper Films. *J. Appl. Phys.* **43**, 867 (1972).
32. I.V. Tomov, D.S. Stoychev and I.B. Vitanova: Recovery And Recrystallization Of Electrodeposited Bright Copper Coatings At Room-Temperature.2. X-Ray-Investigation Of Primary Recrystallization. *J. Appl. Electrochem.* **15**, 887 (1985).
33. H. Lee, W.D. Nix and S.S. Wong: Studies of the driving force for room-temperature microstructure evolution in electroplated copper films. *J. Vac. Sci. Tech. B* **22**, 2369 (2004).
34. C. Lingk and M.E. Gross: Recrystallization kinetics of electroplated Cu in damascene trenches at room temperature. *J. Appl. Phys.* **84**, 5547 (1998).

35. L. Lu, Y.F. Shen, X.H. Chen, L.H. Qian and K. Lu: Ultrahigh strength and high electrical conductivity in copper. *Science* **304**, 422 (2004).
36. W.C. Oliver and G.M. Pharr: An Improved Technique For Determining Hardness And Elastic-Modulus Using Load And Displacement Sensing Indentation Experiments. *J. Mater. Res.* **7**, 1564 (1992).
37. W.C. Oliver and G.M. Pharr: Measurement of hardness and elastic modulus by instrumented indentation: Advances in understanding and refinements to methodology. *J. Mater. Res.* **19**, 3 (2004).
38. G.G. Stoney: *Proceedings of the Royal Society* **A82**, 172 (1909).
39. J.C. Hay, A. Bolshakov and G.M. Pharr: A critical examination of the fundamental relations used in the analysis of nanoindentation data. *J. Mater. Res.* **14**, 2296 (1999).
40. X. Chen and J.J. Vlassak: Numerical study on the measurement of thin film mechanical properties by means of nanoindentation. *J. Mater. Res.* **16**, 2974 (2001).
41. K.L. Johnson, *Contact Mechanics* (Cambridge University Press, Cambridge, 1985),
42. D. Tabor, *The hardness of metals* (Clarendon Press, Oxford, 1951), pp.175
43. J.J. Vlassak and W.D. Nix: Measuring the elastic properties of anisotropic materials by means of indentation experiments. *J. Mech. Phys. Solids* **42**, 1223 (1994).
44. T.Y. Tsui, J.J. Vlassak and W.D. Nix: Indentation plastic displacement field: Part I. The case of soft films on hard substrates. *J. Mater. Res.* **14**, 2196 (1999).
45. T.Y. Tsui, J.J. Vlassak and W.D. Nix: Indentation plastic displacement field: Part II. The case of hard films on soft substrates. *J. Mater. Res.* **14**, 2204 (1999).
46. R. Saha and W.D. Nix: Effects of the substrate on the determination of thin film mechanical properties by nanoindentation. *Acta Mater.* **50**, 23 (2002).
47. X. Chen and J.J. Vlassak: Numerical study on the measurement of thin film mechanical properties by means of nanoindentation. *J. Mater. Res.* **16**, 2974 (2001).
48. R.B. King: Elastic Analysis Of Some Punch Problems For A Layered Medium. *Int. J. Solids Struct.* **23**, 1657 (1987).
49. A.K. Bhattacharya and W.D. Nix: Analysis Of Elastic And Plastic-Deformation Associated With Indentation Testing Of Thin-Films On Substrates. *Int. J. Solids Struct.* **24**, 1287 (1988).

50. A. Bolshakov and G.M. Pharr: Influences of pileup on the measurement of mechanical properties by load and depth sensing indentation techniques. *J. Mater. Res.* **13**, 1049 (1998).
51. N.A. Fleck, H. Otoyoy and A. Needleman: Indentation on porous solids. *Int. J. Solids Struct.* **29**, 1613 (1992).
52. X. Chen, Y. Xiang and J.J. Vlassak: A Novel Technique of Measuring the Mechanical Properties of Porous Materials by Nanoindentation: with Application to Low-k Dielectric Thin Films. submitted (2005).
53. G.W. Farnell and E.L. Adler, *Physical Acoustics* (Academic Press, New York and London, 1972), pp.35
54. G. Carlotti, L. Doucet and M. Dupeux: Comparative study of the elastic properties of silicate glass films grown by plasma enhanced chemical vapor. *J. Vac. Sci. Technol. B* **14**, 3460 (1996).
55. M.A. Haque and M.T.A. Saif: Deformation mechanisms in free-standing nanoscale thin films: A quantitative in situ transmission electron microscope study. *Proc. Nat. Acad. Sci.* **101**, 6335 (2004).
56. H.B. Huang and F. Spaepen: Tensile testing of free-standing Cu, Ag and Al thin films and Ag/Cu multilayers. *Acta Mater.* **48**, 3261 (2000).
57. D.T. Read, Y.W. Cheng, R.R. Keller and J.D. McColskey: Tensile properties of free-standing aluminum thin films. *Scripta Mater.* **45**, 583 (2001).
58. H.D. Espinosa, B.C. Prorok and B. Peng: Plasticity size effects in free-standing submicron polycrystalline FCC films subjected to pure tension. *J. Mech. Phys. Solids* **52**, 667 (2004).
59. J.J. Vlassak and W.D. Nix: A new bulge test technique for the determination of Young's modulus and Poisson's ratio of thin films. *J. Mater. Res.* **7**, 3242 (1992).
60. D.Y.W. Yu and F. Spaepen: The yield strength of thin copper films on Kapton. *J. Appl. Phys.* **95**, 2991 (2004).
61. R. Spolenak, W.L. Brown, N. Tamura, A.A. MacDowell, R.S. Celestre, H.A. Padmore, B. Valek, J.C. Bravman, T. Marieb, H. Fujimoto, B.W. Batterman and J.R. Patel: Local plasticity of Al thin films as revealed by X-ray microdiffraction. *Phys. Rev. Lett.* **90**, (2003).

62. H.D. Espinosa and B. Peng: A new methodology to investigate fracture toughness of freestanding MEMS and advanced materials in thin film form. *J. MEMS* **14**, 153 (2005).
63. H.D. Espinosa, B.C. Prorok and M. Fischer: A methodology for determining mechanical properties of freestanding thin films and MEMS materials. *J. Mech. Phys. Solids* **51**, 47 (2003).
64. J.J. Vlassak, New experimental techniques and analysis methods for the study of mechanical properties of materials in small volumes, Ph.D. Dissertation, Stanford University, Stanford, CA (1994).
65. Y. Xiang, X. Chen and J.J. Vlassak: The plane-strain bulge test for thin films. *J. Mater. Res.* **20**, 2360 (2005).
66. J.W. Beams: Mechanical properties of thin films of gold and silver, in *Structure and Properties of Thin Films*, edited by C.A. Neugebauer, J.B. Newkirk and D.A. Vermilyea (John Wiley and Sons, New York, NY, 1959), p.183
67. R.W. Hoffman: in *Physics of Thin Films*, edited by G. Hass and R. E. Thun (Academic Press, New York, 1966), p.211
68. P.S. Alexopoulos and T.C. Osullivan: Mechanical-Properties Of Thin-Films. *Annu. Rev. Mater. Sci.* **20**, 391 (1990).
69. L.B. Freund: The mechanics of electronic materials. *Int. J. Solids Struct.* **37**, 185 (2000).
70. N. Triantafyllidis and E.C. Aifantis: A Gradient Approach To Localization Of Deformation.1. Hyperelastic Materials. *J. Elast.* **16**, 225 (1986).
71. E.C. Aifantis: Gradient deformation models at nano, micro, and macro scales. *J. Eng. Mater. Tech.* **121**, 189 (1999).
72. N.A. Fleck, G.M. Muller, M.F. Ashby and J.W. Hutchinson: Strain Gradient Plasticity - Theory And Experiment. *Acta Metall.* **42**, 475 (1994).
73. N.A. Fleck and J.W. Hutchinson: A reformulation of strain gradient plasticity. *J. Mech. Phys. Solids* **49**, 2245 (2001).
74. N.A. Fleck and J.W. Hutchinson: Strain gradient plasticity. *Advances In Applied Mechanics* **33**, 295 (1997).
75. N.A. Fleck and J.W. Hutchinson: A Phenomenological Theory For Strain Gradient Effects In Plasticity. *J. Mech. Phys. Solids* **41**, 1825 (1993).

76. L. Nicola, E. Van der Giessen and A. Needleman: Discrete dislocation analysis of size effects in thin films. *J. Appl. Phys.* **93**, 5920 (2003).
77. A. Needleman and E. Van der Giessen: Discrete dislocation and continuum descriptions of plastic flow. *Mater. Sci. Eng. A* **309**, 1 (2001).
78. M.E. Gurtin: On the plasticity of single crystals: free energy, microforces, plastic-strain gradients. *J. Mech. Phys. Solids* **48**, 989 (2000).
79. M.E. Gurtin: A gradient theory of single-crystal viscoplasticity that accounts for geometrically necessary dislocations. *J. Mech. Phys. Solids* **50**, 5 (2002).
80. J.L. Bassani, A. Needleman and E. Van der Giessen: Plastic flow in a composite: a comparison of nonlocal continuum and discrete dislocation predictions. *Int. J. Solids Struct.* **38**, 833 (2001).
81. E. Bittencourt, A. Needleman, M.E. Gurtin and E. Van der Giessen: A comparison of nonlocal continuum and discrete dislocation plasticity predictions. *J. Mech. Phys. Solids* **51**, 281 (2003).
82. E. Van der Giessen and A. Needleman: Discrete Dislocation Plasticity - A Simple Planar Model. *Modelling Simul. Mater. Sci. Eng.* **3**, 689 (1995).
83. N.A. Fleck, M.F. Ashby and J.W. Hutchinson: The role of geometrically necessary dislocations in giving material strengthening. *Scripta Mater.* **48**, 179 (2003).
84. H. Gao, Y. Huang, W.D. Nix and J.W. Hutchinson: Mechanism-based strain gradient plasticity - I. Theory. *J. Mech. Phys. Solids* **47**, 1239 (1999).
85. Y. Huang, H. Gao, W.D. Nix and J.W. Hutchinson: Mechanism-based strain gradient plasticity - II. Analysis. *J. Mech. Phys. Solids* **48**, 99 (2000).
86. J.S. Stolken and A.G. Evans: A microbend test method for measuring the plasticity length scale. *Acta Mater.* **46**, 5109 (1998).
87. M.A. Haque and M.T.A. Saif: Strain gradient effect in nanoscale thin films. *Acta Mater.* **51**, 3053 (2003).
88. L. Nicola, Y. Xiang, J.J. Vlassak, E. Van der Giessen and A. Needleman: Plastic deformation of freestanding thin films: experiments and modeling. *J. Mech. Phys. Solids*, Submitted (2005).
89. J.R. Greer, W.C. Oliver and W.D. Nix: Size dependence of mechanical properties of gold at the micron scale in the absence of strain gradients. *Acta Mater.* **53**, 1821 (2005).

90. E.O. Hall: *Proc. Phys. Soc. London Sect. B* **64**, 747 (1951).
91. N.J. Petch: *J. Iron Steel Inst.* **173**, 25 (1953).
92. G.E. Dieter, *Mechanical metallurgy*, 3rd ed. (McGraw-Hill, New York, 1986), pp.287
93. Z.W. Shan, E.A. Stach, J.M.K. Wiezorek, J.A. Knapp, D.M. Follstaedt and S.X. Mao: Grain boundary-mediated plasticity in nanocrystalline nickel. *Science* **305**, 654 (2004).
94. S. Yefimov, I. Groma and E. van der Giessen: A comparison of a statistical-mechanics based plasticity model with discrete dislocation plasticity calculations. *J. Mech. Phys. Solids* **52**, 279 (2004).
95. Y. Xiang and J.J. Vlassak: Bauschinger effect in thin metal films. *Scripta Mater.* **53**, 177 (2005).
96. A.J. Kalkman, A.H. Verbruggen and G.C.A.M. Janssen: Young's modulus measurements and grain boundary sliding in freestanding thin metal films. *Appl. Phys. Lett.* **78**, 2673 (2001).
97. D.T. Read, Y.W. Cheng and R. Geiss: Morphology, microstructure, and mechanical properties of a copper electrodeposit. *Microelectron. Eng.* **75**, 63 (2004).
98. Y. Xiang, X. Chen and J.J. Vlassak: The mechanical properties of electroplated Cu thin films measured by means of the bulge test technique. *Mater. Res. Soc. Symp. Proc.* **695**, 189 (2002).
99. Y. Xiang, J.J. Vlassak, M.T. Perez-Prado, T.Y. Tsui and A.J. McKerrow: The effects of passivation layer and film thickness on the mechanical behavior of freestanding electroplated Cu thin films with constant microstructure. *Mater. Res. Soc. Symp. Proc.* **795**, 417 (2004).
100. H.J. Lee, G. Cornella and J.C. Bravman: Stress relaxation of free-standing aluminum beams for microelectromechanical systems applications. *Appl. Phys. Lett.* **76**, 3415 (2000).
101. P.A. Flinn: Measurement And Interpretation Of Stress In Copper-Films As A Function Of Thermal History. *J. Mater. Res.* **6**, 1498 (1991).
102. M.D. Thouless, J. Gupta and J.M.E. Harper: Stress Development And Relaxation In Copper-Films During Thermal Cycling. *J. Mater. Res.* **8**, 1845 (1993).

103. R. Keller, S.P. Baker and E. Arzt: Quantitative analysis of strengthening mechanisms in thin Cu films: effects of film thickness, grain size, and passivation. *J. Mater. Res.* **13**, 1307 (1998).
104. R. Spolenak, C.A. Volkert, K. Takahashi, S. Fiorillo, J. Miner and W.L. Brown: Mechanical properties of electroplated copper thin films. *Mater. Res. Soc. Symp. Proc.* **594**, 63 (2000).
105. L.S. Palatnik and A.I. Linskii: The Strength Of Vacuum Condensates Of Copper. *Sov. Phys.-Solid State* **3**, 2053 (1962).
106. A. Lawley and S. Schuster: Tensile Behavior Of Copper Foils Prepared From Rolled Material. *Trans. Metall. Soc. AIME* **230**, 27 (1964).
107. I.A. Oding and I.T. Aleksanyan: *Sov. Phys.-Dokl.* **8**, 818 (1964).
108. H. Leidheiser and B.W. Sloope: Mechanical Properties Of Copper Films. *J. Appl. Phys.* **41**, 402 (1970).
109. R.R. Keller, J.M. Phelps and D.T. Read: Tensile and fracture behavior of free-standing copper films. *Mater. Sci. Eng. A* **214**, 42 (1996).
110. D.T. Read: Tension-tension fatigue of copper thin films. *Int. J. Fatigue* **20**, 203 (1998).
111. O. Tabata, K. Kawahata, S. Sugiyama and I. Igarashi: Mechanical property measurements of thin-films using load deflection of composite rectangular membranes. *Sensors and Actuators* **20**, 135 (1989).
112. H. Hencky: Uber den Spannungszustand in kreisrunden Platten mit verschwindender Biegesteifigkeit. *Zeitschrift fur Mathematik und Physik* **63**, 311 (1915).
113. S. Levy: Large deflection theory for rectangular plates, in *Non-linear problems in mechanics of continua*, edited by E. Reissner, W. Prager and J.J. Stoker (Proc. Symposia. Appl. Math. **I**, American Mathematical Society, New York, 1949), p.197
114. P. Lin, The in-situ measurement of mechanical properties of multi-layer coatings, Ph.D. Dissertation, Massachusetts Institute of Technology, Cambridge, MA (1990).
115. S. Timoshenko and S. Woinowsky-Krieger, Theory of plates and shells (McGraw-Hill, New York, 1959), pp.580
116. H. Itozaki, Mechanical properties of composition modulated copper-palladium foils, Ph.D. Dissertation, Northwestern University, Evanston, IL (1982).

117. M.K. Small and W.D. Nix: Analysis of the accuracy of the bulge test in determining the mechanical properties of thin-films. *J. Mater. Res.* **7**, 1553 (1992).
118. M.K. Small, J.J. Vlassak and W.D. Nix: Re-examining the bulge test: methods for improving accuracy and reliability, in *Thin Films: Stress and Mechanical Properties III*, edited by W.D. Nix, J.C. Bravman, E. Arzt and L.B. Freund (Mater. Res. Soc. Symp. Proc. **239**, Pittsburgh, PA, 1992), p.257
119. F. Maseeh and S.D. Senturia: Viscoelasticity and creep recovery of polyimide thin films, in *Technical Digest. IEEE Solid-State Sensor and Actuator Workshop*, edited by IEEE (IEEE, New York, NY, 1990), p.55
120. Y. Xiang, T.Y. Tsui, J.J. Vlassak and A.J. McKerrow: Measuring the elastic modulus and ultimate strength of low-k dielectric materials by means of the bulge test, in *Proc. IEEE Int. Interconnect Technol. Conf.*, edited by IEEE (IEEE, Piscataway, NJ, 2004), p.133
121. M. Azrin and W.A. Backofen: Deformation And Failure Of A Biaxially Stretched Sheet. *Metall. Trans.* **1**, 2857 (1970).
122. S.H. Hong, K.H. Chung and C.H. Lee: Effects of hot extrusion parameters on the tensile properties and microstructures of SiCw-2124Al composites. *Mater. Sci. Eng. A* **206**, 225 (1996).
123. H. Gao, L. Zhang, W.D. Nix, C.V. Thompson and E. Arzt: Crack-like grain-boundary diffusion wedges in thin metal films. *Acta Mater.* **47**, 2865 (1999).
124. Y.C. Joo, S.J. Hwang and H. Park: The Effect of Grain Boundary Characteristics on Microstructure and Stress Void Evolution in Electroplated and Sputtered Cu Films. *Materials Science Forum* **426-432**, 3481 (2003).
125. C.R. Barrett, W.D. Nix and A.S. Tetelman, The principles of engineering materials (Prentice-Hall, Englewood Cliffs, N. J., 1973), pp.xiv
126. G. Simmons and H. Wang, Single crystal elastic constants and calculated aggregate properties: A handbook, 2nd ed. (MIT Press, Cambridge, MA, 1970),
127. M.A. Phillips, R. Spolenak, N. Tamura, W.L. Brown, A.A. MacDowell, R.S. Celestre, H.A. Padmore, B.W. Batterman, E. Arzt and J.R. Patel: X-ray microdiffraction: local stress distributions in polycrystalline and epitaxial thin films. *Microelectron. Eng.* **75**, 117 (2004).
128. C.J. Youngdahl, J.R. Weertman, R.C. Hugo and H.H. Kung: Deformation behavior in nanocrystalline copper. *Scripta Mater.* **44**, 1475 (2001).

129. R. Armstrong, I. Codd, R.M. Douthwaite and N.J. Petch: Plastic Deformation Of Polycrystalline Aggregates. *Philosophical Magazine* **7**, 45 (1962).
130. Y. Xiang, T.Y. Tsui and J.J. Vlassak: The mechanical properties of freestanding electroplated Cu thin films. *Acta Mater.* submitted for publication. (2005).
131. J.W. Hutchinson, Personal communication. (2005).
132. J. Bauschinger: *Civilingenieur* **27**, 289 (1881).
133. G. Masing: *Wiss. Veroff. Siemens-Konzern* **3**, 231 (1923).
134. R.E. Stoltz and R.M. Pelloux: Bauschinger Effect In Precipitation Strengthened Aluminum-Alloys. *Metall. Trans. A* **7**, 1295 (1976).
135. R. Sowerby, D.K. Uko and Y. Tomita: A review of certain aspects of the Bauschinger effect in metals. *Mater. Sci. Eng.* **41**, 43 (1979).
136. P.S. Bate and D.V. Wilson: Analysis of the bauschinger effect. *Acta Metall.* **34**, 1097 (1986).
137. T. Hasegawa, T. Yakou and U.F. Kocks: Forward And Reverse Rearrangements Of Dislocations In Tangled Walls. *Mater. Sci. Eng.* **81**, 189 (1986).
138. O.B. Pedersen, L.M. Brown and W.M. Stobbs: The bauschinger effect in copper. *Acta Metall.* **29**, 1843 (1981).
139. H. Margolin, F. Hazaveh and H. Yaguchi: The grain boundary contribution to the bauschinger effect. *Scripta Metall.* **12**, 1141 (1978).
140. N. Ono, T. Tsuchikawa, S. Nishimura and S. Karashima: Intergranular constraint and the Bauschinger effect. *Mater. Sci. Eng.* **59**, 223 (1983).
141. A. Aran, M. Demirkol and A. Karabulut: Bauschinger effect in precipitation-strengthened aluminium alloy 2024. *Mater. Sci. Eng.* **89**, L35 (1987).
142. J.D. Atkinson, L.M. Brown and W.M. Stobbs: Work-Hardening Of Copper-Silica.4. Bauschinger Effect And Plastic Relaxation. *Philos. Mag.* **30**, 1247 (1974).
143. L.M. Brown and W.M. Stobbs: Work-Hardening Of Copper-Silica.1. Model Based On Internal Stresses, With No Plastic Relaxation. *Philos. Mag.* **23**, 1185 (1971).
144. L.M. Brown and W.M. Stobbs: Work-Hardening Of Copper-Silica.2. Role Of Plastic Relaxation. *Philos. Mag.* **23**, 1201 (1971).

145. L.M. Brown: Orowan's explanation of the Bauschinger effect. *Scripta Metall.* **11**, 127 (1977).
146. R. Hsu and R.J. Arsenault: The influence of surface removal on the Bauschinger effect. *Mater. Sci. Eng.* **66**, 35 (1984).
147. Y. Xiang, X. Chen and J.J. Vlassak: The plane-strain bulge test for thin films. (submitted).
148. S.P. Baker, R.M. Keller-Flaig and J.B. Shu: Bauschinger effect and anomalous thermomechanical deformation induced by oxygen in passivated thin Cu films on substrates. *Acta Mater.* **51**, 3019 (2003).
149. M.J. Kobrinsky and C.V. Thompson: The thickness dependence of the flow stress of capped and uncapped polycrystalline Ag thin films. *Appl. Phys. Lett.* **73**, 2429 (1998).
150. T. Li, Z.Y. Huang, Z.C. Xi, S.P. Lacour, S. Wagner and Z. Suo: Delocalizing strain in a thin metal film on a polymer substrate. *Mechanics Of Materials* **37**, 261 (2005).
151. Y. Xiang, T. Li, Z. Suo and J.J. Vlassak: High ductility of a metal film adherent on a polymer substrate. *J. Appl. Phys.* **87**, in press (2005).
152. G.P. Zhang, C.A. Volkert, R. Schwaiger, E. Arzt and O. Kraft: Damage behavior of 200-nm thin copper films under cyclic loading. *J. Mater. Res.* **20**, 201 (2005).
153. J.J. Vlassak: Channel cracking in thin films on substrates of finite thickness. *Int. J. Fract.* **119**, 299 (2003).
154. L.B. Freund, personal communication (1995).
155. H.-J. Bunge, Texture analysis in materials science: mathematical methods (Butterworths, London, 1982), pp.593
156. H. Tada, P.C. Paris and G.R. Irwin, The Stress Analysis of Cracks Handbook (Del Research Corporation, Hellertown, PA, 1973), pp.2.11
157. U.F. Kocks: Relation Between Polycrystal Deformation And Single-Crystal Deformation. *Metallurgical Transactions* **1**, 1121 (1970).

Appendix A

Experimental documentation

The experimental work presented in this thesis involves both standard facilities and self-constructed apparatus. A successful experiment requires knowledge of both detailed experimental procedures and special operation cares. The purpose of this Appendix is therefore to document the important details and to serve as a technical reference for future work.

A.1 Micromachining

Adopted from the fabrication process for ultra-large-scale integrated circuits, the micromachining technology has been widely used in the fabrication of micro-electrical-

mechanical-system (MEMS) and nano-electrical-mechanical-system (NEMS) devices. Micromachining, or microfabrication, generally involves photolithographic patterning and various isotropic/anisotropic etch processes. In the current work, the freestanding membranes are fabricated using the standard Si micromachining techniques. Some of the details are described below.

A.1.1 Substrate preparation

We start with (100) single crystal silicon wafers precoated on both sides with 80 nm Si_3N_4 using low pressure chemical vapor deposition (LPCVD). The front (polished) side may or may not be precoated with the film of interest also. The size of the wafer is 8 inches in diameter as received from commercial sources. Since the facilities used in the current work can only process a maximum of 3" wafers, we first need to cut the 8" wafers into 2" \times 2" square substrates. Figure A.1 schematically illustrates the Si wafer cleavage method, which adopts the configuration of a three-point bending test. First, a short line is scratched lightly along the $\langle 110 \rangle$ direction of the Si substrate using a diamond scribe. The notch as shown in the cross-section of the Si substrate in Fig. A.1(a) exaggerates the actual depth of the scribe line. The Si wafer is then placed between a special glass pliers with the scribe line aligned with the marker on the top jaw. By slowly squeezing the pliers, the Si wafer breaks along the $\langle 110 \rangle$ direction. Figure A.1(b) shows the glass pliers, which are available commercially from suppliers such as McMaster-Carr, Inc.

Some special care needs to be taken in the practice though. For example, the short scribe line is usually applied on the backside of the wafer, so films coated on the front

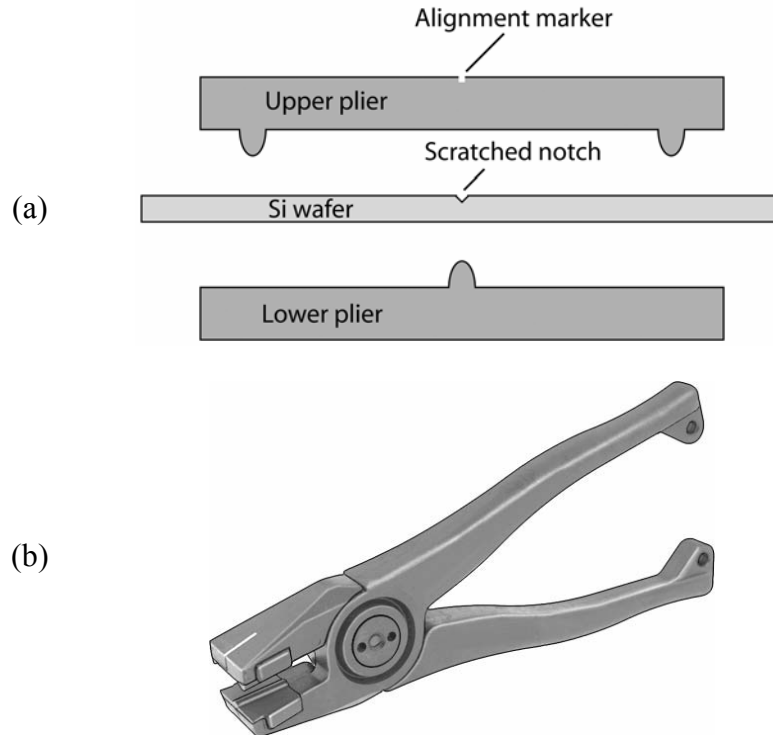


Figure A.1: Si wafer cleavage method: (a) Schematic illustration of the cross-section of the Si wafer and the glass pliers; (b) The glass pliers.

side should be properly protected to prevent any scratches. This can be realized by placing the wafer into a holder supporting only the wafer edges. Moreover, when the Si wafer breaks, Si debris usually scatter on the film of interest and/or Si_3N_4 surface and cause scratches in the film or the Si_3N_4 . It is thus critical to blow the wafer surfaces carefully using a pressurized nitrogen flow after the cleavage. The wafer may be further rinsed thoroughly using deionized (DI) water if necessary.

A.1.2 Photolithography

As discussed in Chapter 3, the Si_3N_4 coating on the backside of the Si substrate serves as hard mask during the wet etching. Patterns are defined through a photolithographic process and transferred into the Si_3N_4 using reactive ion etch (RIE). A negative photoresist (Shipley 1805) is first spincoated onto the Si_3N_4 followed by exposure to a ultra-violet (UV) light source under the mask, which defines the pattern. Figure A.2 shows a typical mask design for bulge test samples on a $2'' \times 2''$ square wafer. The mask is in negative tone. Four square dies with rectangular windows at the center are defined. It should be noted that the dimensions of the rectangles should be slightly larger than the

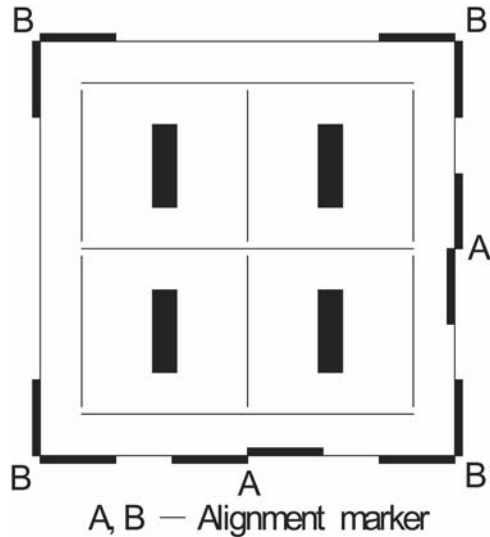


Figure A.2: A typical photolithographic mask designed for patterning 2 by 2 long rectangular windows in the Si_3N_4 coating. The dimensions of the rectangles are 3.32×10.92 mm^2 .

window to be created in the front side of the wafer due to the inclined walls formed by (111) surfaces during the anisotropic wet etch. For example, in order to make freestanding membrane windows of $2.4 \times 10 \text{ mm}^2$ in the front side, the rectangles in the mask should be approximately $3.32 \times 10.92 \text{ mm}^2$ for a $650 \text{ }\mu\text{m}$ substrate. Shallow scribe lines are etched to facilitate the die cutting. The edges of the rectangles are aligned with the straight edges (i.e., $\langle 110 \rangle$ directions) of the Si substrate, which is assisted by two primary alignment markers (Marker A in Fig. A.2) at the center of two neighboring edges. There are four auxiliary alignment makers at four corners (Marker B).

Table A.1 lists the detailed patterning steps and parameters used in the photolithography. It should be noted that, some of the steps may not be necessary in certain cases. For example, wafers are generally clean enough as received from commercial sources. Therefore, the wafer clean steps may not be necessary in such a case. Moreover, since some coatings do not suffer from moisture and oxidization in the wet etching, such as Si_3N_4 or films capped with Si_3N_4 , BCB coating protection may not be necessary. Instead, a Shipley coating can be used to protect the front side from scratching when the back side is being processed. The Shipley coating can be subsequently removed right after the patterning process is complete (i.e., before the wet etching step).

A.1.3 Reactive ion etch

The patterns defined by the photoresist need to be transferred into the Si_3N_4 coating by means of reactive ion etch (RIE). RIE uses reactive plasmas as etchant to selectively remove materials, which is also called “dry etch”. For example, the plasmas of

Table A.1: Photolithography steps and parameters

Substrate preparation	
Wafer cutting	See Section A.1.1
Wafer clean	TCE, Acetone, and Methanol ultrasound bath: 5 min each
Dehydration	Hot plate: 10min @ 120 °C
Front (film) side process	
Spin AP ^{a)}	5 sec @ 500 rpm; 20 sec @ 3500 rpm
Spin BCB	5 sec @ 200 rpm; 5 sec @ 500 rpm; 40 sec @ 4500 rpm
Pre-Exposure Bake ^{b)}	3.5 min each @ 40 °C, 50 °C, 60 °C; 1.5 min @ 75 °C
Exposure ^{c)}	20 sec @ 10 mW/cm ²
Post-Exposure Bake	3.5 min each @ 40 °C, 50 °C, 60 °C; 1.5 min @ 75 °C
Hard Curing	1 hr @ 120 °C
Back side process	
Spin Shipley 1805	5 sec @ 500 rpm; 2500rpm @ 40 sec
Pre-Exposure Bake	3.5min @ 103 °C
Exposure	11.5 sec @ 10 mW/cm ²
Post-Exposure Bake	3.5 min @ 103 °C
Development	CD30, 1 min (or: 10 more sec after no more bleeding)
DI Water Rinse	1 min

^{a)} Adhesion Promoter from Dow Chemical, Inc.; ^{b)} All bake on hot plate; ^{c)} All exposure in Karl-SUSS aligner.

CF₄ or SF₆ react with Si₃N₄ or Si at a much higher rate than with the Shipley photoresist. The reaction products are in gas forms, resulting in a selective removal of the materials that are not covered by Shipley.

The equipment used in the current work is a RIE-2000 from South Bay Technology, Inc. Typical operation parameters used for Si₃N₄ etch are a CF₄ flow rate of 30 sccm, a working pressure of 100 mTorr; a forward radio frequency power of 100

Watts with an adjusted minimum reflected power. 80 nm Si_3N_4 can be completely etched in 2 minutes at approximately 10 Å/sec.

A.1.4 Anisotropic wet etch

After RIE, patterns are transferred into Si_3N_4 , which serves the hard mask for wet etching. The exposed Si substrate is thus etched using a potassium hydroxide (KOH) based solution. This solution etches single crystal Si anisotropically with the maximum and minimum etch rates on (100) and (111) faces, respectively. Therefore, the etch pits are formed with (100) and (111) facets, when the edges of the rectangular mask align with the $\langle 110 \rangle$ directions of the (100) Si substrate. The concentration of the solution is approximately 23-wt.%, which gives an etch rate of approximately 1.2 $\mu\text{m}/\text{min}$ at 80 °C [See Table A.2]. The procedure for wet etching is given in Table A.2, while the setup is schematically illustrated in Fig. A.3. The temperature and concentration of the KOH

Table A.2: Procedure for wet etching.

Solution	15g KOH : 50ml H ₂ O (23-wt.%); 80 °C; etch rate ~1.2 $\mu\text{m}/\text{min}$
Procedure	<ol style="list-style-type: none"> 1. Mount the wafer into the wet etching holder. 2. Connect to venting system. 3. Vacuum the holder chamber for 15 min. 4. Fill N₂ into the chamber, adjust bubbler to get proper pressure, typically, ~1 bubble/sec. 5. Etch at 80 °C for ~10 hours for a 700-μm-thick wafer . 6. Take out the holder, clean, dry and cool it down. 8. Remove wafers out of the clamp and remove the gasket very carefully. 9. Rinse wafers with DI water.

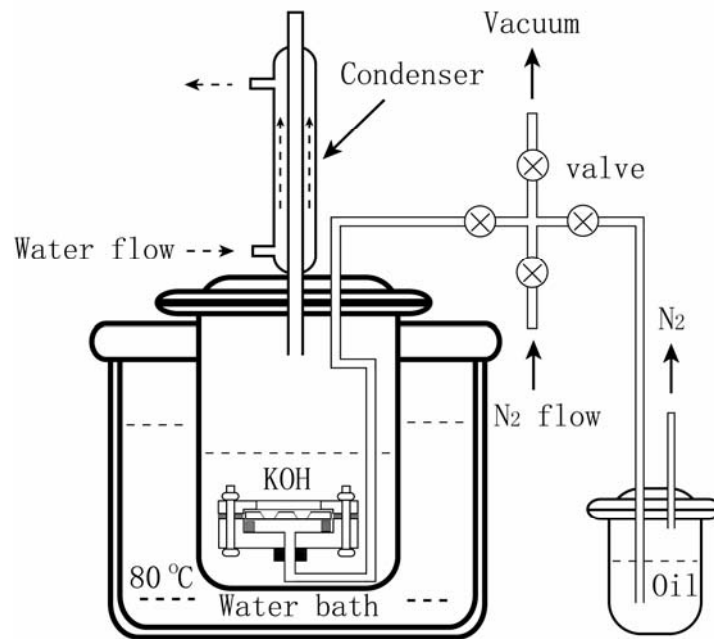


Figure A.3: Schematic illustration of our wet etching system.

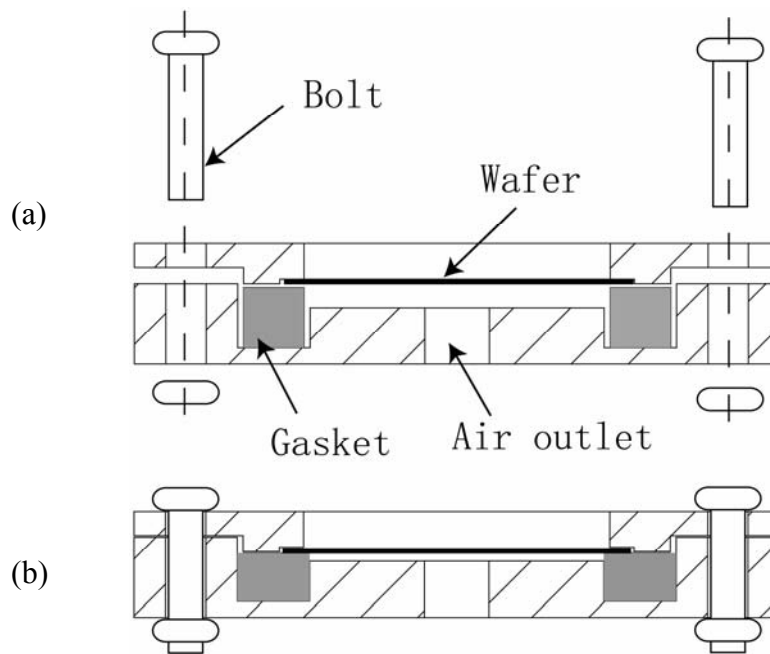


Figure A.4: Schematic illustration of the wafer holder for wet etching.

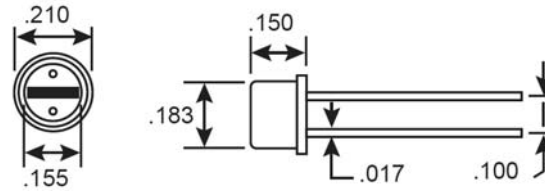
solution is maintained through a water bath and a condenser, respectively. A special holder is used to hold the substrate in the KOH solution, as schematically shown in Fig. A.4. The upper and lower parts of the holder are fastened and a soft rubber gasket is compressed approximately 20% to provide good sealing. The film side of the wafer is therefore protected from chemicals, moisture, and oxidization. There is a gas outlet at the lower part of the holder connecting to a nitrogen flow, which balances the pressure between two sides of the wafer. Otherwise, a differential pressure may build up due to the thermal expansion of the air gap at elevated temperatures, which may break the membrane once it is released freestanding at the late stage of the etching process.

A.2 Bulge test system

In this section, a technical documentation of the hardware and software of our bulge test system as well as its operation procedures is given.

A.2.1 Displacement measurement

The bulge test apparatus is schematically illustrated in Fig. 3.7, in which the displacement is measured using a laser interferometer. The intensity at the center of the interferometric fringe pattern is recorded continuously as a function of time into computer through a photosensor. The photosensor is based on a light sensitive resistor (Clairex[®] 621 – CL905L, as shown in Fig. A.6). The light sensitive material is CdS,



Dimension: inch

Figure A.5: The light sensitive resistor.

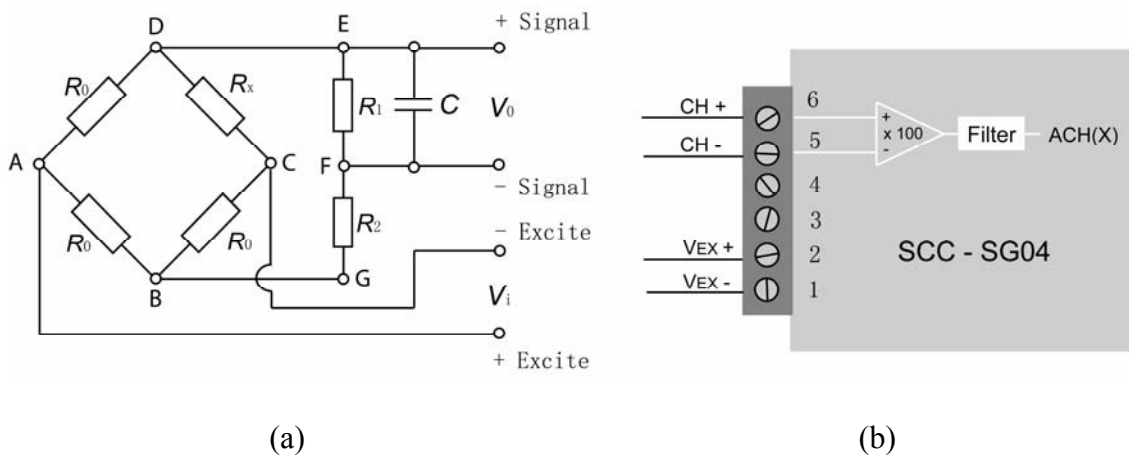


Figure A.6: (a) A full bridge circuit to monitor the fringe intensity. (b) The power supply and signal processing module (SCC-SG04) for the full bridge.

which has a peak response wavelength of 550 nm. The light sensitive resistor is stable and has low light memory. Its electrical resistance varies approximately from 10^2 to 10^4 Ω at the highest and lowest illumination intensities, respectively. The resistance is monitored using a bridge circuit, as shown in Fig. A.6.

We now analyze the Wheatstone full bridge circuit in Fig. A.6(a) and determine the device parameters. For the He-Ne laser (wavelength 633 nm, power 1mW) used in our system, the resistance of the light sensitive resistor, R_x , is measured to vary approximately from 300 Ω (R_{ON} , at maximum illumination intensity) to 64 k Ω (R_{OFF} , in fully darkness). We choose the reference resistor $R_0 = 10$ k Ω in the bridge [Fig. A.6(a)].

The output voltage of the bridge, V_{BD} , is therefore

$$V_{BD} = \left(\frac{R_0}{R_x + R_0} - \frac{R_0}{R_0 + R_0} \right) V_i = \frac{V_i}{2} \left(\frac{1 - R_x / R_0}{1 + R_x / R_0} \right), \quad (\text{A.1})$$

where $R_x / R_0 \sim 0.03 - 6.4$. The bridge is excited with an input voltage $V_i = 2.5$ V using a strain gauge module SCC-SG04 [Fig. A.6(b)] from National Instruments, Inc. The direct output voltage of the bridge, V_{BD} , therefore ranges approximately from -1.25 V (in fully dark) to $+1.25$ V (at maximum illumination intensity), which is out of the input range of the signal processing module SCC-SG04, ± 100 mV. Two resistors, R_1 and R_2 , are used to adjust the output voltage such that

$$V_{EF} = \frac{R_1}{R_1 + R_2} V_{BD}, \quad (\text{A.2})$$

where the absolute value of V_{EF} should be less than 0.1 V, while the maximum of V_{BD} is 1.25 V. This leads to

$$\frac{R_1}{R_1 + R_2} \times 1.25 \leq 0.1 \quad \text{or} \quad R_2 \geq 11.5 \times R_1. \quad (\text{A.3})$$

Noticing that R_1 and R_2 should be much larger than R_0 to avoid significant interference

with the bridge circuit, we thus choose $R_1 = 1 \text{ M}\Omega$ and $R_2 = 12.2 \text{ M}\Omega$.

There is, however, significant noise in the voltage output V_{EF} , as a result of background illumination noise as well as circuit noise, both of which typically have relatively high frequencies. Since the frequency of the fringe signal is typically equal or lower than 1 Hz, a simple low-pass filter is used by adding a capacitor C into the circuit such that any noise with frequencies higher than 1 Hz is filtered out. This requires $\sqrt{R_1 C} \approx 1$ and we thus obtain the capacity $C = 1 \text{ mF}$. The filtered signal V_0 is then collected by the SCC-SG04, as shown in Fig. A.6(b).

A.2.2 Data acquisition and experimental procedure

The experiment control and data acquisition for the bulge test are automated through a LabView program, the interface of which is shown in Fig. A.7. In the top two windows, the fringe intensity and the applied pressure are monitored in real time during the experiment. Users need to set a few control parameters: “Rate Factor” controls the loading rate through a stepper motor; $P_1 - P_{12}$ set the starting and ending pressures of loading or unloading (as indicated by the arrows) segments for up to 6 cycles. The current loading rate and the current loading-unloading cycle are displayed in “Current Rate” and “Current Cycle”.

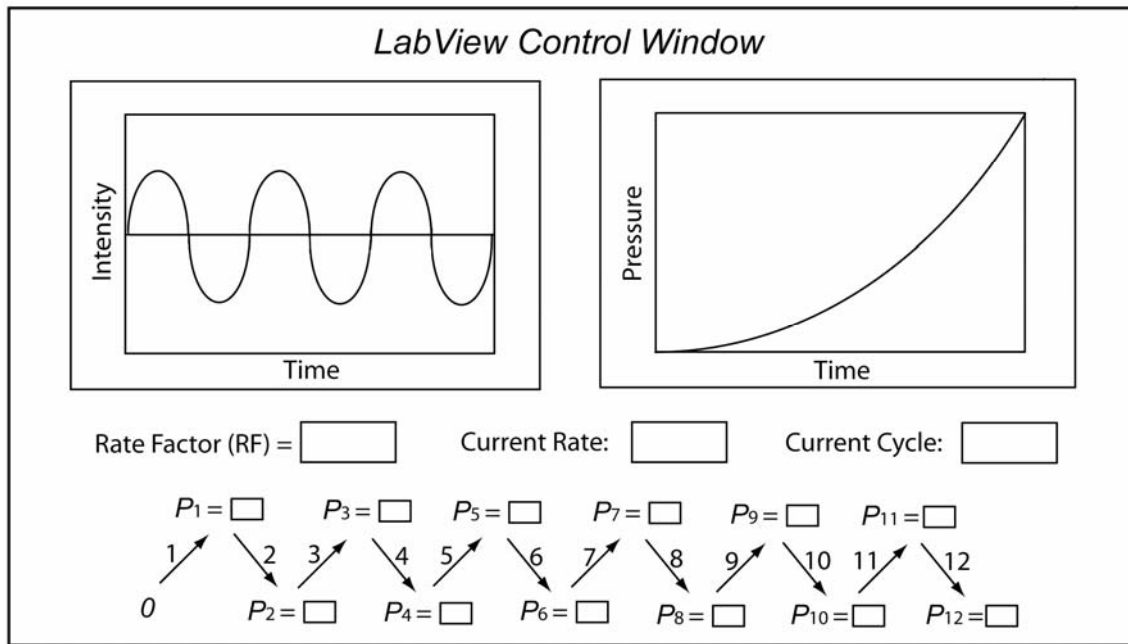


Figure A.7: Schematic illustration of the experiment control software interface.

The experiment process is controlled through a Matlab routine embedded in the LabView program. A flag variable, s , which is called the cycle number, is used to distinguish the individual loading or unloading segments. s is an integer taking the value from 1 to 12, with odd s for loading and even for unloading, as shown in Fig. A.7. A simple control flow is as follows:

1. Read pressure P ;
2. Check the current cycle number s and compare P with the corresponding loading segment ranges $P_1 - P_2$; $P_2 - P_3$, $P_3 - P_4 \dots$;
3. If P is out of range for a given cycle s , s increases by one; otherwise keep the current cycle number s ;
4. Repeat step 1 – 3.

A self-protection check is also employed in the program such that the program stops automatically whenever the membrane breaks. This is realized by checking whether the pressure is zero at any stages of the experiment except the beginning. Otherwise,

Table A.3: Procedure for the bulge test.

Preparation	<ol style="list-style-type: none"> 1. Mount the sample <ol style="list-style-type: none"> a. Open the valves and fill the cavity with water b. Position the sample with film side facing downwards c. Position references around the substrate d. Use vacuum grease for sealing e. Tighten the screws evenly 2. Align the optics of the laser interferometer <ol style="list-style-type: none"> a. Align and fix the half-silvered mirror b. Center the laser beam on the membrane c. Adjust mirror 1 to make the reference laser beam concentric with the incidence beam d. Adjust half-silvered mirror to make the reflected beam concentric with the reference beam e. Adjust mirror 2 and lens to project the fringe pattern on the screen with the photosensor in the center of the fringe pattern f. Fine tune the half-silvered mirror to make the fringe pattern symmetric 3. Close the valve to the water reservoir but make sure the valve connecting to pressure sensor is open
Experiment	<ol style="list-style-type: none"> 1. Run the control program Main.vi 2. Decrease the pressure slowly using motor control window until it is a little bit below zero, determine the zero point by observing the fringe pattern 3. Initialize the Matlab workspace 4. Set the pressure values for loading and unloading segments, set loading rate, and start the experiment 5. The program stops automatically if the preset loading cycles are finished or if the membrane breaks at any time

the stepper motor will keep pushing the ball screw in a loading cycle, since the pressure never reaches the preset values. This may cause the damage of the stepper motor and the ball screw. A typical procedure for the bulge test is the given Table A.3.

A.2.3 Data processing

For each test, two raw data files are stored, each of which contains two columns of data. One file records the intensity versus time and the other records the pressure versus time. The time axes of the two sets of data are synchronized. Typical data processing includes five steps:

1. Smooth the raw data by seven-point averaging and plot intensity–time and pressure–time curves.
2. Between each loading and unloading, there is a transition period. Light intensity signals in the transitions are typically very noisy, which may affect the normal data analysis. Therefore, transition signals need to be removed by setting them equal to a constant in the intensity–time curve.
3. Search and mark fringe peaks in the intensity–time curve. Save the peak–time data. Each peak corresponds to one single fringe.
4. Determine the pressure value corresponding to each peak: First locate the time for a given peak t_p , and then use the nearest two data points in the pressure–time curve to interpolate the pressure value at t_p . This is possible because the two data files are synchronized in the experiment. Save the pressure–peak data.

-
5. Calculate pressure–deflection and stress–strain curves: First determine the fringe number by counting the peaks. Starting from 0, the fringe number increases by one for each peak in loading cycles and decreases by one during unloading. The loading and unloading cycles need to be manually determined on the time axis, which is done in Step 2. Now we have the pressure–fringe number data. Deflection is then calculated using the fringe number. Finally, the stress–strain curve is calculated from the pressure–deflection data.

Appendix B

Calculation of the equivalent uniaxial stress–strain curve

The stress–strain curves obtained in the bulge test are plane-strain stress–strain curves. These curves can be converted into equivalent uniaxial stress–strain curves using an analysis first suggested by Freund [154]. This analysis eliminates the effect of the residual stress on the stress–strain curves and facilitates comparison of experimental bulge test data with results obtained from uniaxial tension tests.

The three principal stress directions of the freestanding film are shown in Fig. 3.1(a). Since the pressure applied to the film is much smaller compared to the in-plane stress, σ_3 can be taken equal to zero during the experiment. Initially, when the applied pressure is zero, the film has an equi-biaxial residual stress, $\sigma_1 = \sigma_2 = \sigma_0$. During the

experiment, σ_1 are ε_1 are measured. In the elastic regime σ_2 can be determined through Poisson's effect

$$\sigma_2 = \sigma_0 + \nu(\sigma_1 - \sigma_0), \quad (\text{B1})$$

as a result of the plane-strain condition.

In the following analysis, the material is assumed to obey the J_2 flow theory. Considering $\sigma_3 = 0$, the von Mises equivalent stress $\bar{\sigma}$ is given by

$$\bar{\sigma} = (\sigma_1^2 - \sigma_1\sigma_2 + \sigma_2^2)^{1/2}, \quad (\text{B2})$$

where σ_1 is measured, σ_2 is given by Eq. (B1) in the elastic regime and is yet to be determined in the plastic regime. The equivalent plastic strain $\bar{\varepsilon}_p$ is a function of the equivalent stress $\bar{\sigma}$

$$\bar{\varepsilon}_p = g(\bar{\sigma}). \quad (\text{B3})$$

The flow rates associated with the von Mises criterion are in this case:

$$\begin{aligned} \dot{\varepsilon}_1^p &= \frac{\sigma_1 - 1/2\sigma_2}{\bar{\sigma}} g'(\bar{\sigma}) \dot{\bar{\sigma}} \\ \dot{\varepsilon}_2^p &= \frac{\sigma_2 - 1/2\sigma_1}{\bar{\sigma}} g'(\bar{\sigma}) \dot{\bar{\sigma}} \end{aligned} \quad (\text{B4})$$

where $g'(\bar{\sigma}) = \frac{d\bar{\varepsilon}_p}{d\bar{\sigma}}$. In the experimental configuration here, the response is rate-independent and σ_1 increases monotonically with time. As a result, time can be replaced with σ_1 in the above equations. By writing out the equation for the strain rates in the longitudinal and transverse directions along with the plane-strain constraints, we find

$$\left\{ \begin{array}{l} \frac{d\varepsilon_1}{d\sigma_1} = \frac{1}{E} \left(1 - \nu \frac{d\sigma_2}{d\sigma_1} \right) + \frac{\sigma_1 - \frac{1}{2}\sigma_2}{\bar{\sigma}} \frac{dg}{d\sigma_1}, \\ \frac{d\varepsilon_2^e}{d\sigma_1} = \frac{1}{E} \left(\frac{d\sigma_2}{d\sigma_1} - \nu \right), \\ \frac{d\varepsilon_2^p}{d\sigma_1} = \frac{\sigma_2 - \frac{1}{2}\sigma_1}{\bar{\sigma}} \frac{dg}{d\sigma_1}, \\ \frac{d\varepsilon_2^e}{d\sigma_1} + \frac{d\varepsilon_2^p}{d\sigma_1} = 0. \end{array} \right. \quad (\text{B5})$$

These equations are solved for $\frac{dg}{d\sigma_1}$ and $\frac{d\sigma_2}{d\sigma_1}$, resulting in the following

differential equations:

$$\left\{ \begin{array}{l} \frac{d\sigma_2}{d\sigma_1} = \nu - \frac{E \left(\frac{1-\nu^2}{E} - \frac{d\varepsilon_1}{d\sigma_1} \right) (\sigma_1 - 2\sigma_2)}{\sigma_1(2-\nu) - \sigma_2(1-2\nu)}, \\ \frac{dg}{d\sigma_1} = \frac{2\bar{\sigma} \left(\frac{d\varepsilon_1}{d\sigma_1} - \frac{1-\nu^2}{E} \right)}{\sigma_1(2-\nu) - \sigma_2(1-2\nu)}. \end{array} \right. \quad (\text{B6})$$

Noting that the plane-strain modulus is $M = \frac{E}{1-\nu^2}$ and the tangential plane-strain

modulus is $M_t = \frac{d\sigma_1}{d\varepsilon_1}$, the above equations are revised to

$$\left\{ \begin{array}{l} \frac{d\sigma_2}{d\sigma_1} = \nu - \frac{E \left(\frac{1}{M} - \frac{1}{M_t} \right) (\sigma_1 - 2\sigma_2)}{\sigma_1(2-\nu) - \sigma_2(1-2\nu)}, \\ \frac{dg}{d\sigma_1} = \frac{2\bar{\sigma} \left(\frac{1}{M_t} - \frac{1}{M} \right)}{\sigma_1(2-\nu) - \sigma_2(1-2\nu)}. \end{array} \right. \quad (\text{B7})$$

By integrating equations (B7), the longitudinal stress σ_2 and the equivalent stress–strain curve $\bar{\varepsilon}_p = g(\bar{\sigma})$ can be derived from an experimental measurement of $\sigma_1(\varepsilon_1)$. In practice, the plane-strain modulus M is determined from the unloading sections of the measured $\sigma_1(\varepsilon_1)$ curve, and the tangential plane-strain modulus M_t at each point can be obtained by a linear fit to adjacent data points. Poisson’s ration ν can be taken as equal to the bulk value or needs to be determined from an independent measurement. The initial value of σ_2 is obtained from equation (B1) in the elastic regime. With these parameters, the above differential equations can be numerically solved to get the equivalent strain $\bar{\varepsilon}_p$, and the longitudinal stress σ_2 , thus obtaining the von Mises equivalent stress $\bar{\sigma}$ using equation (B2). The resulting $\bar{\sigma}-\bar{\varepsilon}_p$ curve is the equivalent uniaxial stress–strain curve. This numerical solution can be readily implemented in a spreadsheet.

Appendix C

Calculation of the plane-strain modulus of a polycrystalline film

In this section, we detail how the plane-strain modulus of a polycrystalline thin film can be estimated from the single-crystal elastic constants and the experimental orientation distribution function of the film. The following derivation applies to single crystals with cubic symmetry, but it is readily generalized to other crystal symmetries. The crystallographic texture of the polycrystalline film is represented by the orientation distribution function, $f(g)$, defined as the probability density of grains with orientations ranging from g to $g + dg$ [155]:

$$f(g)dg = \frac{dV}{V}, \quad (\text{C1})$$

where dV is the total volume of grains orientated in the range of g to $g + dg$, and V is the total volume of the sample. The orientation element dg can be expressed in terms of the three Eulerian angles (Φ , φ_1 , and φ_2):

$$dg = \frac{1}{8\pi^2} \sin \Phi d\Phi d\varphi_1 d\varphi_2. \quad (C2)$$

The elastic behavior of an anisotropic single crystal is described by the generalized Hooke's law

$$\epsilon_{ij} = s_{ijkl} \sigma_{kl}, \quad (C3)$$

$$\sigma_{ij} = c_{ijkl} \epsilon_{kl}, \quad (C4)$$

where s_{ijkl} and c_{ijkl} are respectively the compliance and stiffness tensors of the single crystal in a Cartesian coordinate system. For crystals with cubic symmetry, the axes of the coordinate system are usually aligned with the edges of the unit cell of the crystal. The elastic constants in other coordinate systems are readily found using tensor transformations:

$$s'_{ijkl} = a_{mi} a_{nj} a_{pk} a_{ql} s_{mnpq}, \quad (C5)$$

$$c'_{ijkl} = a_{mi} a_{nj} a_{pk} a_{ql} c_{mnpq}, \quad (C6)$$

where s'_{ijkl} and c'_{ijkl} are the compliance and stiffness tensors in the new coordinate system.

The direction cosines a_{ij} can be written in terms of the Eulerian angles of the crystal coordinate system with respect to the new coordinate system:

$$A = \begin{bmatrix} \cos \varphi_1 \cos \varphi_2 - \sin \varphi_1 \sin \varphi_2 \cos \Phi & \sin \varphi_1 \cos \varphi_2 + \cos \varphi_1 \sin \varphi_2 \cos \Phi & \sin \varphi_2 \sin \Phi \\ -\cos \varphi_1 \sin \varphi_2 - \sin \varphi_1 \cos \varphi_2 \cos \Phi & -\sin \varphi_1 \sin \varphi_2 + \cos \varphi_1 \cos \varphi_2 \cos \Phi & \cos \varphi_2 \sin \Phi \\ \sin \varphi_1 \sin \Phi & -\cos \varphi_1 \sin \Phi & \cos \Phi \end{bmatrix} \quad (C7)$$

In order to determine the effective elastic constants of a polycrystalline film with ODF given by $f(g)$, the single-crystal constants are first transformed to the macroscopic coordinate system attached to the film and then averaged over the volume of the film:

$$\bar{s}_{ijkl} = \oint s'_{ijkl}(\varphi_1, \Phi, \varphi_2) \frac{dV}{V} = \oint s'_{ijkl}(\varphi_1, \Phi, \varphi_2) f(g) dg, \quad (C8)$$

$$\bar{c}_{ijkl} = \oint c'_{ijkl}(\varphi_1, \Phi, \varphi_2) \frac{dV}{V} = \oint c'_{ijkl}(\varphi_1, \Phi, \varphi_2) f(g) dg. \quad (C9)$$

Note that Eq. (C8) represents the iso-stress or Reuss average of the elastic constants, while Eq. (C9) represents the iso-strain or Voigt average.

For films with fiber textures, the averaged tensors reflect the symmetry of the film, i.e., they are transversely isotropic. The plane-strain modulus of a transversely isotropic coating with elastic constants c_{ijkl} and s_{ijkl} is given by

$$M = c_{1111} - \frac{c_{1133}^2}{c_{3333}} = \left[s_{1111} - \frac{s_{1122}^2}{s_{1111}} \right]^{-1}, \quad (C10)$$

where the x_3 -axis is perpendicular to the film and the x_2 -axis points in the direction of plane strain. The Reuss and Voigt averages of the plane-strain modulus of the polycrystalline film are then respectively

$$M^R = \left[\bar{s}_{1111} - \frac{\bar{s}_{1122}^2}{\bar{s}_{1111}} \right]^{-1}, \quad (C11)$$

$$M^V = \bar{c}_{1111} - \frac{\bar{c}_{1133}^2}{\bar{c}_{3333}}. \quad (\text{C12})$$

The Voigt and Reuss averages represent upper and lower bounds for the plane-strain modulus of the polycrystalline film. The average of the bounds provides a good estimate for the modulus of the film:

$$M = (M^V + M^R) / 2. \quad (\text{C13})$$

Slightly different averaging schemes are possible, but usually do not result in significantly different moduli. The theoretical moduli shown in Fig. 4.6 were calculated using the single-crystal elastic constants for Cu obtained from [126].

Appendix D

Influence of grain boundary grooving on experimental film stiffness

In order to evaluate the effect of grain boundary grooving on the effective film stiffness, grain boundary grooves are approximated by a periodic array of cracks. A cell containing one such crack is schematically illustrated in Fig. 4.8, where c is the average depth of the grain boundary grooves, and h is the film thickness. The length of the cell, $2d$, is the average spacing between grain boundary grooves and can be taken equal to the average grain size of the film. Since grooving only occurs at high-energy grain boundaries, twin boundaries should not be counted as grain boundaries in this case. The presence of the grain boundary increases the compliance of the cell and results in an extra displacement Δ when the cell is subjected to a stress σ . If $d/h \geq 1$, the displacement Δ is

given by

$$\Delta = \Delta_{total} - \Delta_{no\ crack} = \frac{4\sigma c}{M} \cdot V(c/h), \quad (D1)$$

where $V_2(c/h)$ is approximated by the following equation [156]:

$$V(c/h) = \frac{c/h}{(1-c/h)^2} \left[0.99 - c/h(1-c/h)(1.3 - 1.2c/h + 0.7c^2/h^2) \right]. \quad (D2)$$

The equation has a better than 1% accuracy for any value of c/h . The additional strain due to the presence of the crack is therefore

$$\varepsilon_{crack} = \frac{\Delta}{2d} = \frac{2\sigma c}{Md} \cdot V(c/h). \quad (D3)$$

From Equations (D1) and (D2), it follows that

$$\frac{2c}{dM} \cdot V_2(c/h) = \frac{1}{M_c} - \frac{1}{M}, \quad (D4)$$

where M_c is the effective plane-strain modulus of a film with grooves. Rewriting Eq. (D4) yields the following expression for the effective modulus as a function of the normalized groove depth (c/h) and groove density (h/d)

$$\frac{M_c}{M_0} = \left(1 + 2 \cdot \frac{h}{d} \cdot \frac{c}{h} \cdot V_2\left(\frac{c}{h}\right) \right)^{-1}. \quad (D5)$$

For the 1.8 μm films with $c = 40$ nm and $2d = 3.0$ μm , Eq. (D5) predicts a reduction in modulus of approximately 1%; for the 3.0 μm films with $c = 170$ nm and $2d = 6.1$ μm , the reduction is approximately 2%.

Appendix E

Taylor factor for polycrystalline thin films

In order to evaluate the effect of the crystallographic texture, the Taylor factor was calculated for each of the electroplated films using the experimental orientation distribution functions (ODF). A detailed description of the procedure can be found in reference [157]; here only the main points are highlighted. The basic hypotheses in the Taylor factor calculation are that elastic strains are small compared to plastic strains and that the strain experienced by each grain is exactly equal to the macroscopically imposed strain. Since the macroscopic strain is in principle arbitrary, each grain needs at least five independent slip systems to satisfy this last requirement. The procedure for calculating the polycrystalline behavior is then relatively straightforward. For a given grain orientation $(\varphi_1, \Phi, \varphi_2)$, all possible combinations of five slip systems are considered that produce the macroscopically imposed strain through

$$\varepsilon_{ij}^m = \sum_k \mu_{ij}^{(k)} \gamma^{(k)}, \quad (\text{E1})$$

where ε_{ij}^m is the macroscopic plastic strain tensor transformed to the crystal coordinate system and $\gamma^{(k)}$ is the shear on slip system k . The coefficients μ_{ij} in Eq. (E1) are defined as follows

$$\mu_{ij} = \frac{1}{2} (m_i n_j + m_j n_i) \quad (\text{E2})$$

and are known as the Schmid factors for slip system (\mathbf{m}, \mathbf{n}) where \mathbf{m} is the unit normal to the slip plane and \mathbf{n} the unit vector parallel to the slip direction. For a face-centered cubic material such as Cu, there are twelve slip systems and hence $C_{12}^5 = 792$ combinations of five independent slip systems that satisfy Eq. (E1). Of all these combinations, the active set of five slip systems satisfies Bishop and Hill's principle of minimum plastic dissipation:

$$W_p = \sum_k \tau_y^{(k)} |\dot{\gamma}^{(k)}| = \text{minimum}. \quad (\text{E3})$$

If the critical resolved shear stress $\tau_y^{(k)}$ is the same on all slip systems, Eq. (E3) reduces to

$$\sum_k |\dot{\gamma}^{(k)}| = \text{minimum}, \quad (\text{E4})$$

i.e., the active set of slip systems is the one that minimizes the algebraic sum of shears on each of the slip systems. Once the active slip systems are known for a grain with a given orientation, it is a simple matter to calculate the stress tensor required to deform the grain:

$$\mu_{ij}^{(k)} \sigma_{ij} = \tau_y, \quad (\text{E5})$$

where k runs from 1 to 5. Since only five slip systems are active, the stress state can be determined only to within a hydrostatic component. For some grain orientations, it is possible that several sets of slip systems satisfy the Bishop and Hill criterion. In this case, the stress states associated with each of these sets are averaged. The stress tensor thus obtained depends on the orientation $(\varphi_1, \Phi, \varphi_2)$ of the grain. The stress state for the polycrystalline film is determined by averaging the stress tensor over all possible grain orientations using the orientation distribution function, $f(g)$, as a weight function:

$$\bar{\sigma}_{ij} = \oint \sigma_{ij}(\varphi_1, \Phi, \varphi_2) f(g) dg. \quad (\text{E6})$$

The hydrostatic stress component is finally determined from the condition that the surface of the film be stress free. In a uniaxial tension experiment, the Taylor factor is defined as the ratio of the uniaxial stress and the critical resolved shear stress:

$$M_T = \frac{\sigma_y^o}{\tau_y}. \quad (\text{E7})$$

For a polycrystalline material with a random crystallographic texture subjected to uniaxial tension, the above procedure results in the classical value of $M_T = 3.06$. If a state of plane strain is imposed instead and one takes into account the crystallographic textures [Fig. 4.2] of the specific samples, one obtains the plane-strain Taylor factors plotted in Fig. 4.7(b). In these calculations, all numerical integrations over the Euler angles were performed with a step size of $\pi/36$.